

박 사 학 위 논 문

Ph.D. Dissertation

다중 적층빔 및 케이블의 선형 및 비선형 해석을 위한
연속체역학 기반 빔 유한요소의 개발

Development of continuum mechanics based beam elements for
linear and nonlinear analyses of multi-layered composite beam
and helically stranded cable structures

2020

김 효 진 (金 效 津 Kim, Hyo-Jin)

한 국 과 학 기 술 원

Korea Advanced Institute of Science and Technology

박 사 학 위 논 문

다중 적층빔 및 케이블의 선형 및 비선형 해석을 위한
연속체역학 기반 빔 유한요소의 개발

2020

김 효 진

한 국 과 학 기 술 원

기계항공공학부/기계공학과

다중 적층빔 및 케이블의 선형 및 비선형 해석을
위한 연속체역학 기반 빔 유한요소의 개발

김 효 진

위 논문은 한국과학기술원 박사학위논문으로
학위논문 심사위원회의 심사를 통과하였음

2020 년 06 월 09 일

심사위원장 이 필 승 (인)

심사위원 곽 효 경 (인)

심사위원 김 성 수 (인)

심사위원 박 용 화 (인)

심사위원 유 승 화 (인)

Development of continuum mechanics based beam elements for linear and nonlinear analyses of multi-layered composite beam and helically stranded cable structures

Hyo-Jin Kim

Advisor: Phill-Seung Lee

A dissertation/thesis submitted to the faculty of
Korea Advanced Institute of Science and Technology in
partial fulfillment of the requirements for the degree of
Doctor of Philosophy in Mechanical Engineering

Daejeon, Korea

June 09, 2020

Approved by

Phill-Seung Lee

Professor of Mechanical Engineering

The study was conducted in accordance with Code of Research Ethics¹⁾.

1) Declaration of Ethical Conduct in Research: I, as a graduate student of Korea Advanced Institute of Science and Technology, hereby declare that I have not committed any act that may damage the credibility of my research. This includes, but is not limited to, falsification, thesis written by someone else, distortion of research findings, and plagiarism. I confirm that my dissertation contains honest conclusions based on my own careful research under the guidance of my advisor.

DME

Hyo-Jin Kim. Development of continuum mechanics based beam elements for linear and nonlinear analyses of multi-layered composite beam and helically stranded cable structures. Department of Mechanical Engineering. 2020. 84+vi pages. Advisor: Phill-Seung Lee. (Text in English)

Abstract

In this thesis, novel continuum mechanics based beam finite elements for the linear and nonlinear analyses of multi-layered composite beams and multi-layered helically stranded cable structures are introduced. The primary feature of the proposed beam finite element is an advanced modeling capability that originates from the general 3D geometry and displacement interpolations of the continuum mechanics based beams. The continuum mechanics based beam formulation enables much simpler and more efficient modeling procedure using relatively small number of the degree of freedom (DOF), because the entire geometry of the layered beam is modeled as a single beam model instead of modeling the each individual sub-component of the beam. Thus, it is possible to deal with the behavior of the entire multi-layered beam and helically stranded cable structures regardless of the numbers of layers and sub-components. The modeling capability and the performance of the proposed beam element model were verified through several numerical examples. The proposed beam finite element exhibits excellent predictive and modeling capabilities to deal with complicated geometries including arbitrary numbers of layers and wires, composite cross-sections, eccentricities in addition to various loading conditions. Further, the proposed beam finite element is successfully applicable for predicting the nonlinear behaviors of the multi-layered beam and cable structures while considering the geometrical and material nonlinearities of the sub-components as well as the nonlinear load-slip relation.

Keywords: layered beams; helically stranded cable; multi-layered; composite beams; interlayer slips; continuum mechanics; finite element analysis; nonlinear analysis

Contents

Contents	i
List of Tables	iii
List of Figures	iv
Chapter 1. Introduction	1
Chapter 2. Continuum mechanics based beam elements multi-layered composite beams with interlayer slips...	3
2.1 Nonlinear kinematics of layered beam structures	4
2.2 Incremental displacement interpolation	8
2.3 Incremental equilibrium equations	10
2.4 Finite element formulations	12
2.5 Numerical examples	15
2.5.1 Simply supported two-layer beam	15
2.5.2 Simply supported two-layer tapered beam	18
2.5.3 Roll-up of a cantilever cross-shaped three-layer beam	20
2.5.4 Buckling of a simply supported two-layer beam	22
2.5.5 Cantilever four-layer sandwich beam	25
2.5.6 Seven-layer I-section beam	29
2.5.7 Cantilever four-layer box beam	32
2.5.8 Comparison with experimental test1: Nailed two-layer wood beam	35
2.5.9 Comparison with experimental test2: Mode II delamination test of ENF specimen	38
2.6 Concluding remarks	41
2.6.1 Summary	41
2.6.2 Future works	42
Chapter 3. Continuum mechanics based beam elements multi-layered helically stranded cable structures	44
3.1 Basic assumptions and local coordinate systems of helically stranded cable structures	47
3.2 Nonlinear kinematics of helically stranded cable structures	50
3.3 Incremental displacement interpolation	53
3.4 Incremental equilibrium equations	56
3.5 Finite element formulations	57
3.6 Numerical examples	60
3.6.1 Convergence study of 7-wire strand cable under tension	60
3.6.2 Convergence study of 7-wire strand cable under bending	62
3.6.3 Cross-sectional interpolation test	65
3.6.4 Comparison with experimental test: Cantilever 7-wire helically-stranded cable	67
3.6.5 Cantilever six-layer 120-wire helically stranded cable	69
3.7 Concluding remarks	74
3.7.1 Summary	74
3.7.2 Future works	74
Chapter 4. Closing remarks	76
Bibliography	78

List of Tables

Table 1. z -directional displacement w at the midpoint of the beam for four load levels ($\lambda = 0.5, 1, 1.5,$ and 2) in the simply supported two-layer beam problem (unit: m).....	17
Table 2. Maximum displacement w_{\max} calculated in four cases of varying cross-sectional geometries ($\alpha_L = 0.3, 0.5, 0.7,$ and 0.9) in the simply supported two-layer beam with varying cross-section problem (unit: m)	19
Table 3. z -directional displacement w at the midpoint of the beam in three cases of eccentricities e in the buckling of the simply supported two-layer beam problem (unit: m).....	23
Table 4. z -directional displacement w at the free tip under $P = 15$ kN in Load Case I of the cantilever four-layer sandwich beam problem (unit: m)	29
Table 5. z - and y -directional displacements (w and v) at the free tip under $P = 15$ kN in Load Case II of the cantilever four-layer sandwich beam problem (unit: m)	29
Table 6. z -directional displacement w at the midspan of the beam under tensile axial load $P = 300$ kN and compressive axial load $P = -50$ kN with a uniformly distributed transverse load $q_0 = 10$ kN/m in the seven-layer I-section beam problem (unit: m).....	32
Table 7. z -directional displacement w and slip displacements s_1 and s_2 at the free tip in two interlayer cases ($\alpha = 0.5$ and 0.05) in the cantilever four-layer box beam problem (unit: m)	35
Table 8. z -directional displacement w at the midpoint of the beam for three load levels ($P = 10$ kN, 20 kN, and 30 kN) in the nailed two-layer wood beam problem (unit: m).....	38
Table 9. Maximum loads P_{\max} in the Mode II delamination test of ENF specimen problem (unit: N) 40	
Table 10. Geometric parameters of cantilever 6-layer, 120-wire helically stranded cable	73

List of Figures

Fig. 1. A continuum mechanics based beam element without slip kinematics allowing three translations and three rotations: (a) A q -node continuum mechanics beam element in the configuration at time t , where $q = 3$, and (b) Cross-section of beam modeled by p -node cross-sectional elements at beam node k , where $p = 4$ 5

Fig. 2. Geometry of a layered beam: (a) A layered beam that consists of l -layers, (b) Side view of layer beam, and (c) Beam nodes and coordinate systems used in the beam element 7

Fig. 3. Simply supported two-layer beam problem: (a) Problem description (E denotes Young's modulus) and (b) Solid element model used to obtain reference solutions 16

Fig. 4. Load-displacement curves for the z -directional displacement w at the midpoint of the beam obtained from the present beam and solid element model in the simply supported two-layer beam problem 17

Fig. 5. Simply supported two-layer tapered beam: (a) Problem description where $b_1 = 0.05$ m , $b_2 = 0.3$ m , $h_1 = 0.15$ m , and $h_2 = 0.05$ m and (b) Solid element model used to obtain reference solutions 17

Fig. 6. Maximum deflections of the beam according to α_L in the simply supported two-layer tapered beam problem 19

Fig. 7. Cantilever cross-shaped three-layer beam subjected to tip bending moment M_y 20

Fig. 8. Numerical results in the cantilever cross-shaped three-layer beam problem: (a) Deformed shapes of the beam at four load levels when $\theta = \pi/2$, π , $3\pi/2$, and 2π , and (b) and (c) Load-displacement curves of x -and z -directional displacements (u and w) at the free tip 21

Fig. 9. Load-slip displacement curves at the free tip of the beam in the cantilever cross-shaped three-layer beam problem 22

Fig. 10. Buckling of simply supported two-layer beam subjected to axial load P 23

Fig. 11. Deflection curves along the beam length according to three eccentricities e (0.015 m , 0.01325 m , and 0.0115 m) in the buckling of two-layer simply supported beam 24

Fig. 12. Cantilever four-layer sandwich beam problem: (a) Problem description and (b) Solid element model used to obtain reference solutions 26

Fig. 13. Numerical results in Load Case I for the cantilever four-layer sandwich beam problem: (a) Load-displacement curves for z-directional displacement w at the free tip, and (b) and (c) Distributions of the von Mises stress obtained from the present beam and solid element models, respectively, when $P = 15$ kN	27
Fig. 14. Numerical results in Load Case II for the cantilever four-layer sandwich beam problem: (a) and (b) Load-displacement curves for z - and y -directional displacements (w and v) at the free tip, and (c) and (d) Distributions of the von Mises stress obtained from the present beam and solid element model, respectively, when $P = 9$ kN, 12 kN, and 15 kN in Interlayer Case II	28
Fig. 15. Seven-layer I-section beam problem: (a) Problem description and (b) Solid element model used to obtain reference solutions	30
Fig. 16. Load-displacement curves for z-directional displacement w at the beam center according to tip axial load P varying from $P = -100$ kN to 300 kN with a constant transverse load $q_0 = 10$ kN/m in the seven-layer I-section beam problem	31
Fig. 17. Cantilever four-layer box beam problem: (a) Problem description and (b) Solid element model used to obtain reference solutions	33
Fig. 18. Numerical results and deformed shapes for the cantilever four-layer box beam problem: (a) and (b) z -directional displacement w and slip displacements s_1 and s_2 at the free tip according to the interlayer connection stiffness ratio α , and (c) and (d) Deformed shapes at the free tip in Interlayer Cases I and II, respectively	34
Fig. 19. Nailed two-layer wood beam problem: (a) Problem description and (b) Foshi-Bonac load-slip curve and material parameters used	36
Fig. 20. Load-displacement curves for the deflection w at the midspan of the beam according to the eccentric axial load P in the nailed two-layer wood beam problem	37
Fig. 21. Mode II delamination test of ENF specimen: (a) Problem description and (b) Bi-linear constitutive relationship used in cohesive interface	39
Fig. 22. Load-displacement curves for the z -directional displacement w at the midspan of the beam according to the concentrated load P in the Mode II delamination test of ENF specimen problem	40
Fig. 23. Geometry of helically stranded cable: (a) A three-layer strand cable consists of and 17-wire where α_n is lay angle of layer n , (b) cross-section of the three-layer strand cable where r_n and R_n are winding radius and radius of wires in layer n respectively	47

Fig. 24. (a) A 7-wire helically stranded cable structure and (b) Flexible cylinder whose radius is r_n , which is winding radius of the outer wire of the cable in (a) 48

Fig. 25. Concept of the multi-director continuum beam finite element for helically stranded cable structures where three coordinate system $\{0\}$, $\{1\}$ and $\{2\}$ are employed to represent the geometry of the strand cable 49

Fig. 26. Cross-sectional modeling of helically stranded cable using cross-sectional nodes and elements: (a) Cross-sectional geometry of a 7-wire strand cable, and (b) Cross-section of sub-wire m at beam node k modeled by p -node cross-sectional elements, where $p = 16$ 52

Fig. 27. Cantilever 7-wire strand cable subjected to tip tensile loading F_x : (a) Problem description, (b) Cross-sectional geometry of the strand cable, and (c) Various helical geometries of the strand cable when lay angle $\alpha = 0^\circ$, 10° , 20° and 30° 61

Fig. 28. (a) and (b) Tip displacement and torsional angle under tensile loading F_x obtained from the various geometries of strand cables (from $\alpha = 0^\circ$ to 30°) when number of element per pitch length $N_p = 4, 8, 12$ and 20 62

Fig. 29. Cantilever 7-wire strand cable subjected to tip bending moment M_y : (a) Problem description, (b) Cross-sectional geometry of the strand cable, and (c) Various helical geometries of the strand cable when lay angle $\alpha = 0^\circ$, 10° , 20° and 30° 63

Fig. 30. (a) and (b) Tip displacement and torsional angle under bending moment M_y obtained from the various geometries of strand cables (from $\alpha = 0^\circ$ to 30°) when number of element per pitch length $N_p = 12, 16, 20$ and 30 64

Fig. 31. (a) Cantilever 7-wire strand cable under Load Case I and Load Case II and (b) Cross-sectional modeling for the core and wires using 9-, 16-, and 25-node cross-sectional elements, respectively 65

Fig. 32. (a) Tip axial displacements and torsional angles under Load Case I, (b) Tip deflections and bending angle under Load Case II 66

Fig. 33. Cantilever 7-wire strand cable subjected to tip axial loading F_x (a) Problem description, (b) Layer-wise and cross-sectional geometries of the cable, and (c) the present beam model using 40 continuum mechanics based beam elements 68

Fig. 34. (a) Axial load-axial strain curves for the axial strain of the cable and (b) Axial load-reaction torque curves for the reaction torque at the tip of the cable 69

Fig. 35. Two-layer strand cable subjected to tip tensile loading F_x : (a) Problem description, (b) Layer-wise and cross-sectional geometry of the cable, and (c) Various helical geometries of the strand cable when lay angle $\alpha = 0^\circ$, -10° , -20° and -30° 70

Fig. 36. (a) and (b) Tip displacement and torsional angle under tensile loading F_x obtained from the various geometries of two-layer strand cables (from $\alpha_2 = 0^\circ$ to -40°) 71

Fig. 37. Six-layer cantilever strand cable composed of 120 wires: (a) Problem description, (b) Layer-wise and cross-sectional geometries of the strand cable (b) Present beam model using 20 continuum mechanics based beam elements 72

Fig. 38. Axial load-axial strain curves in the cantilever six-layer strand cable that consists of 120 wires subjected to uniform tensile loading F_x at the tip 73

Chapter 1. Introduction

Layered beam structures, which refers to beam structures composed of multiple layers and sub-components, are widely used in various engineering fields to obtain enhanced structural properties. The most important feature of these structures is the capability to combine various sub-components that may have different structural and material properties depending on various design requirements. This distinct feature enables to meet improved structural performances together with various practical conditions required in the field, such as high strength, durability, resistance, stiffness-to-weight ratios and flexibility. Laminated composites and sandwich beams, which have been widely used in mechanical and aerospace engineering, and reinforced concrete beams and bolted-beams, which have been primarily used in civil engineering, are representative layered beam structures. Unlike typical layered beam structures normally composed of the rectangular cross-sections and unidirectional layers, there are also layered beam structures with helically twisted geometries. These structures, which are generally referred to as helically stranded cable structures, have been commonly used in many engineering fields, for example, electric copper wires, optical fiber cables, high capacity aluminum conductors, submarine cables, cables for automobile and ships, and so on.

Layered beam structures have much more complex geometries than simple beams that consist of a single material as they are composed of several independent layers and sub-components that may have different properties. They also exhibit more complex behaviors than conventional beam structures, because the incomplete connections between the sub-components induce the composite interactions and individual behaviors of the sub-components. In particular, in the case of multi-layered beam structures, the combination of the composite interactions as well as the individual behaviors of the sub-components become more complex as the number of layers and sub-components increases, and this makes it difficult to predict their behaviors. Such complicated geometries of multi-layered beam structures often require complex numerical models and a massive amount of computation cost. Furthermore, for the analysis of the nonlinear behavior of multi-layered beam structures, it is necessary to perform an iterative solution process while considering the geometrical and material nonlinearities of the sub-components as well as the nonlinear load-slip relation between interlayers. This made accurate analysis more difficult and required much computational time due to a drastic increase in the complexity of the problem. The motivation of the works presented in this thesis comes from finding a way to overcome these difficulties and drawbacks.

The objective of this thesis is to propose new continuum mechanics based beam elements for linear and nonlinear analyses of multi-layered composite beam and helically stranded cable structures, and to demonstrate their performance. The main feature of the proposed beam finite element is an advanced modeling capability that originates from the general 3D geometry and displacement interpolations of the continuum mechanics based beams. The continuum mechanics based beam formulation enables much simpler and more efficient modeling procedure using relatively small number of the degree of freedom (DOF), because the entire geometry of the layered beam is modeled as a single beam model instead of modeling the individual components of the beam. Thus, it is possible to deal with the behavior of the entire layered beam structure regardless of the numbers of layers and sub-components that constitute the beam. Further, the proposed beam finite element is successfully applicable for predicting the nonlinear behaviors of the multi-layered beam and cables while considering the geometrical and material nonlinearities of the sub-components as well as the nonlinear load-slip relation. These benefits enable fast and efficient analysis of the nonlinear behavior of multi-layered beam and cable structures involving complicated geometry. The applicability and the predictive capability of the proposed beam finite element is examined through several numerical examples regarding the linear and nonlinear behaviors of various layered beam structures.

Chapter 2. Continuum mechanics based beam elements multi-layered composite beams with interlayer slips

Layered composite beam structures have been broadly used in various engineering fields due to their many benefits. One distinct feature of such structures is the capability to combine several components depending on specific design requirements. Clearly, the combination of materials enables cost-effective manufacturing together with great functional and structural properties such as high strength, durability, resistance, and stiffness-to-weight ratios and so on [1-3].

Layered beams are composed of several layers that are mechanically or adhesively connected through interlayers to obtain composite interaction. Generally, it is challenging to attain completely rigid interlayer connections effectively. Therefore, deformable interlayer connections allow interlayer slips and ensure only partial composite interaction. Classical beam models assuming perfectly rigid interlayer connections have been widely used, and such models give acceptable results in many engineering problems. However, they are likely to cause significant underestimations, particularly when interlayer connections are relatively weak compared to primary structural components or when large deformation is allowed.

Considerable efforts have been made to develop analytical and numerical models for the analysis of layered beams. After Newmark's works [4], analytical studies on layered beams including partial composite interaction effects have been conducted a lot, see Refs. [4-12] and references therein. A large number of studies have also been carried out to develop numerical models for geometric and material nonlinear behavior of layered beams [13-22]. Most early studies were focused largely on simple two- and three-layer beam problems; however recent efforts have been undertaken for linear analysis of multi-layered beams [23-25]. Although the nonlinear behaviors of two-layered beams are extensively studied in many literatures, little attention has been paid to the general multi-layered beam behaviors. Further developments on geometric and material nonlinear analyses of multi-layered beams encompassing complex beam geometries are still required for widening the applications of layered beams.

Recently, continuum mechanics based beam elements were developed as a direct extension of well-known isoparametric beam elements [26-28]. Incorporating cross-sectional elements in the beam formulation, they provide notable accuracy and efficiency to consider complex 3D beam geometry in geometric and material nonlinear analyses. Fully coupled nonlinear beam behaviors including large displacements and large rotations

have been effectively analyzed. In particular, the continuum mechanics based beams are useful to deal with composite beam structures [29-31].

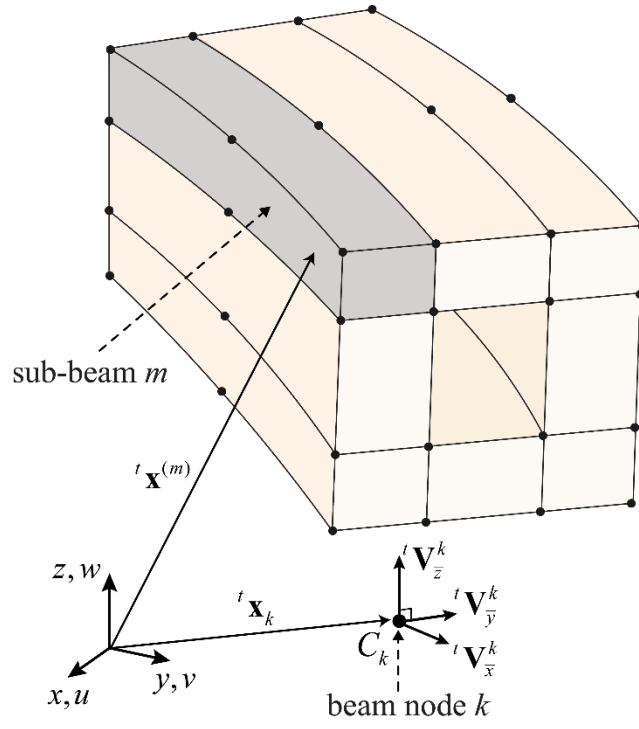
The main topic of Chapter 2 is to propose a new formulation of continuum mechanics based beam elements for linear and nonlinear analyses of multi-layered composite beams with interlayer slips and validate their performance. In order to comprise slip kinematics and the corresponding partial composite interaction effect, the continuum mechanics based beam formulation is enriched by introducing a layer degree of freedom (DOF) for each layer. The cross-sectional geometries of each layer is modeled individually by using cross-sectional elements embedded in the beam formulation, and discontinuous relative displacements between the layers are represented by independent DOFs given to layers.

The significant feature of the present beam formulation is an advanced modeling capability that originates from the general 3D geometry and displacement interpolations of the continuum mechanics based beams. Complicated layered beam geometries including an arbitrary number of layers and interlayers, varying and composite cross-sections, different interlayer stiffnesses, and eccentricities can be easily modeled without using additional interface elements or constraints. Most notably, the proposed beam formulation is applicable to predict geometric and material nonlinear behaviors of multi-layered beams including nonlinear load-slip relations at interlayers.

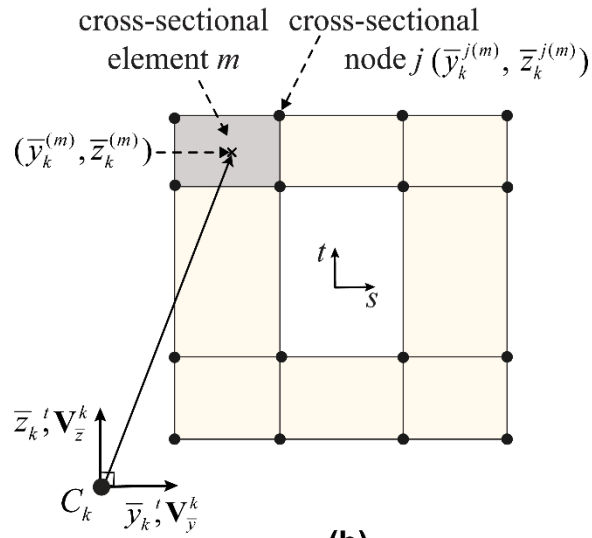
In the following sections, nonlinear kinematics of multi-layered beams allowing interlayer slips and the finite element formulation are presented. Geometry and displacement interpolations for layered beams are described in detail, and linearized incremental equilibrium equations involving partial composite interaction effects are derived based on the total Lagrangian formulation. Finally, the finite element discretization procedure is presented. The performance and predictive capability of the proposed beam finite elements are demonstrated through several illustrative numerical examples.

2.1 Nonlinear kinematics of layered beam structures

The geometry interpolation of the continuum mechanics based beam elements is directly degenerated from an assemblage of 3D solid finite elements; herein, the solid element fibers are aligned along the longitudinal axis of the beam. Each solid element fiber here is named as sub-beam (Fig. 1(a)).



(a)



(b)

Fig. 1. A continuum mechanics based beam element without slip kinematics allowing three translations and three rotations: (a) A q -node continuum mechanics beam element in the configuration at time t , where $q = 3$, and (b) Cross-section of beam modeled by p -node cross-sectional elements at beam node k , where $p = 4$.

For a q -node continuum mechanics based beam element, the material position in sub-beam m in the configuration at time t is given as

$${}^t \mathbf{x}^{(m)} = \sum_{k=1}^q h_k(r) {}^t \mathbf{x}_k + \sum_{k=1}^q h_k(r) \bar{y}_k^{(m)} {}^t \mathbf{V}_{\bar{y}}^k + \sum_{k=1}^q h_k(r) \bar{z}_k^{(m)} {}^t \mathbf{V}_{\bar{z}}^k, \quad (2.1)$$

where $h_k(r)$ is the 1D shape function corresponding to beam node k (C_k), ${}^t \mathbf{x}_k$ is the position vector of beam node k , ${}^t \mathbf{V}_{\bar{y}}^k$ and ${}^t \mathbf{V}_{\bar{z}}^k$ are the orthonormal director vectors that define the cross-sectional Cartesian coordinate system at beam node k together with ${}^t \mathbf{V}_{\bar{x}}^k (= {}^t \mathbf{V}_{\bar{y}}^k \times {}^t \mathbf{V}_{\bar{z}}^k)$, and $\bar{y}_k^{(m)}$ and $\bar{z}_k^{(m)}$ denote the material position in the cross-sectional area of sub-beam m in the cross-sectional Cartesian coordinate system (Figs. 1(a) and (b)). Note that this geometry interpolation allows three translations and three rotations at each beam node.

An important feature of the continuum mechanics based beam element is that the cross-sectional geometry is modeled using cross-sectional elements defined by cross-sectional nodes as shown in Fig. 1(b). For a p -node cross-sectional element m corresponding to sub-beam m (shaded in gray in Fig. 1(b)), the material position in the cross-sectional area ($\bar{y}_k^{(m)}$ and $\bar{z}_k^{(m)}$) is interpolated as

$$\bar{y}_k^{(m)} = \sum_{j=1}^p h_j(s, t) \bar{y}_k^{j(m)}, \quad \bar{z}_k^{(m)} = \sum_{j=1}^p h_j(s, t) \bar{z}_k^{j(m)} \quad (2.2)$$

where $h_j(s, t)$ is the 2D shape function corresponding to cross-sectional node j and $\bar{y}_k^{j(m)}$ and $\bar{z}_k^{j(m)}$ are the coordinates of cross-sectional node j in the cross-sectional Cartesian coordinate system at beam node k .

In order to represent the geometry of layered beams involving slip kinematics, the discontinuous relative displacements between the layers due to the interlayer slips need to be included in Eq. (2.1). Let us consider a layered beam that consists of l -layers in the configuration at time t , as shown in Fig. 2(a). Each layer can be composed of several sub-beams, and the interlayer slips are allowed between the adjacent layers. For example, in Fig. 2(a), the layered beam consists of four layers (Layers 1–4) and allows slips at four interlayers; here, Layers 1 and 4 are composed of three sub-beams, and Layers 2 and 3 are composed of a single sub-beam.

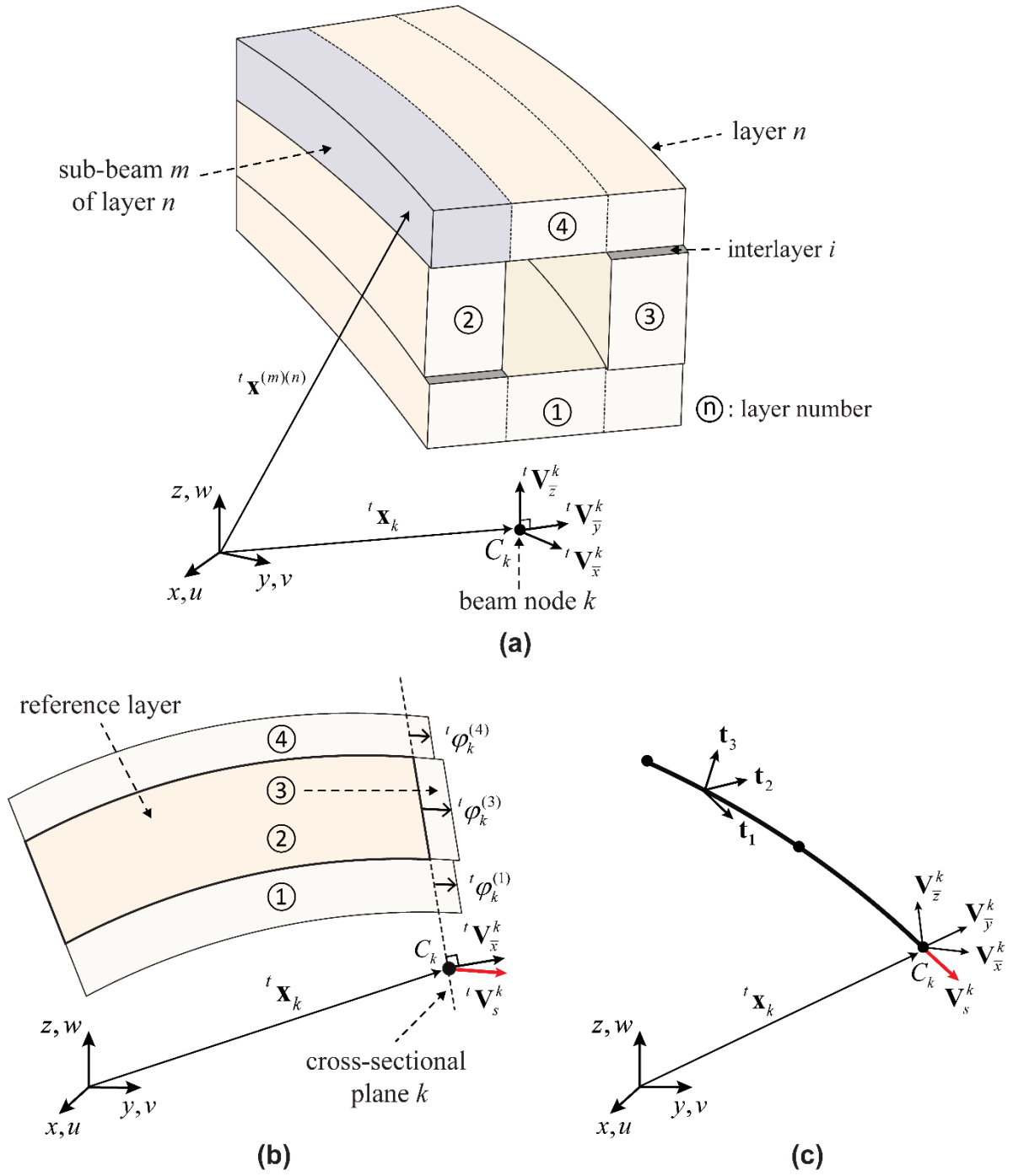


Fig. 2. Geometry of a layered beam: (a) A layered beam that consists of l -layers, (b) Side view of layer beam, and (c) Beam nodes and coordinate systems used in the beam element.

For sub-beam m belonging to layer n , the geometry interpolation of the layered beam including slip kinematics is obtained as

$${}^t \mathbf{x}^{(m)(n)} = \sum_{k=1}^q h_k(r) {}^t \mathbf{x}_k + \sum_{k=1}^q h_k(r) \bar{y}_k^{(m)(n)} {}^t \mathbf{V}_y^k + \sum_{k=1}^q h_k(r) \bar{z}_k^{(m)(n)} {}^t \mathbf{V}_z^k + \sum_{k=1}^q h_k(r) {}^t \varphi_k^{(n)} {}^t \mathbf{V}_s^k \quad (2.3)$$

where $\bar{y}_k^{(m)(n)}$ and $\bar{z}_k^{(m)(n)}$ denote the material position in the cross-section of sub-beam m of layer n , ${}^t \varphi_k^{(n)}$ is the layer DOF given to each layer n at beam node k , and ${}^t \mathbf{V}_s^k$ is the slip director vector that indicates the longitudinal direction of the beam in the configuration at time t .

The slip director vector ${}^t \mathbf{V}_s^k$ at beam node k is defined as

$${}^t \mathbf{V}_s^k = \frac{{}^t \mathbf{g}_x^k}{\|{}^t \mathbf{g}_x^k\|} \quad \text{with} \quad {}^t \mathbf{g}_x^k = \sum_{\xi=1}^q \frac{\partial h_\xi(r)}{\partial r} \Big|_{r=r_k} {}^t \mathbf{x}_\xi \quad (2.4)$$

where r_k is the coordinate of beam node k in the 1D natural coordinate system. Note that the slip director vector ${}^t \mathbf{V}_s^k$ is different from the director vector ${}^t \mathbf{V}_x^k$, which is orthonormal to the ${}^t \mathbf{V}_y^k$ and ${}^t \mathbf{V}_z^k$ in the cross-sectional Cartesian coordinate system (Figs. 2(b) and (c)).

In the geometry interpolation of the layered beam in Eq. (2.3), the layer DOF ${}^t \varphi_k^{(n)}$ denotes the relative displacement in the slip direction (${}^t \mathbf{V}_s^k$) at beam node k between the layer n and a reference layer as shown in Fig. 2(b). The reference layer can be arbitrarily selected and the layer DOFs ${}^t \varphi_k^{(n)}$ assigned to it should be fixed (set to be zero) because the displacements relative to itself is zero. Therefore, the cross-sectional plane of the reference layer at beam node k (cross-sectional plane k) becomes a basis plane to measure the relative displacements. In Fig. 2(b), Layer 2 is chosen as the reference layer, and the corresponding cross-sectional plane k is defined.

From the layer DOFs at beam node k , the slip displacement ${}^t u_s^{(i)}$ on interlayer i between the adjacent layers a and b is interpolated as

$${}^t u_s^{(i)} = \sum_{k=1}^q h_k(r) ({}^t \varphi_k^{(b)} - {}^t \varphi_k^{(a)}). \quad (2.5)$$

2.2 Incremental displacement interpolation

For sub-beam m belonging to layer n , the incremental displacement interpolation is obtained from the configurations at times $t + \Delta t$ and t

$$\begin{aligned}
{}_0\mathbf{u}^{(m)(n)} &= {}^{t+\Delta t}\mathbf{x}^{(m)(n)} - {}^t\mathbf{x}^{(m)(n)} \\
&= \sum_{k=1}^q h_k(r) {}_0\mathbf{u}_k + \sum_{k=1}^q h_k(r) \bar{y}_k^{(m)(n)} ({}^{t+\Delta t}\mathbf{V}_{\bar{y}}^k - {}^t\mathbf{V}_{\bar{y}}^k) + \sum_{k=1}^q h_k(r) \bar{z}_k^{(m)(n)} ({}^{t+\Delta t}\mathbf{V}_{\bar{z}}^k - {}^t\mathbf{V}_{\bar{z}}^k) \\
&\quad + \sum_{k=1}^q h_k(r) ({}^{t+\Delta t}\varphi_k^{(n)t+\Delta t} \mathbf{V}_s^k - {}^t\varphi_k^{(n)t} \mathbf{V}_s^k), \tag{2.6}
\end{aligned}$$

where ${}_0\mathbf{u}_k$ is the incremental nodal displacement from time t to $t + \Delta t$ at beam node k

$${}_0\mathbf{u}_k = [{}_0u_k \quad {}_0v_k \quad {}_0w_k]^T \tag{2.7}$$

Using the well-known Rodrigues formula for parametrization of finite rotations, the director vectors ${}^{t+\Delta t}\mathbf{V}_{\bar{x}}^k$, ${}^{t+\Delta t}\mathbf{V}_{\bar{y}}^k$, and ${}^{t+\Delta t}\mathbf{V}_{\bar{z}}^k$ in the configuration at time $t + \Delta t$ are represented in terms of the director vectors at time t

$${}^{t+\Delta t}\mathbf{V}_{\bar{x}}^k = \mathbf{R}({}_0\boldsymbol{\theta}^k) {}^t\mathbf{V}_{\bar{x}}^k, \quad {}^{t+\Delta t}\mathbf{V}_{\bar{y}}^k = \mathbf{R}({}_0\boldsymbol{\theta}^k) {}^t\mathbf{V}_{\bar{y}}^k, \quad \text{and} \quad {}^{t+\Delta t}\mathbf{V}_{\bar{z}}^k = \mathbf{R}({}_0\boldsymbol{\theta}^k) {}^t\mathbf{V}_{\bar{z}}^k \tag{2.8}$$

where $\mathbf{R}({}_0\boldsymbol{\theta}^k)$ is the finite rotation tensor, which is represented by the skew-symmetric matrix operator $\hat{\mathbf{R}}({}_0\boldsymbol{\theta}^k)$ with the incremental Eulerian angle vector ${}_0\boldsymbol{\theta}^k$ that consists of incremental Eulerian angles ${}_0\theta_x^k$, ${}_0\theta_y^k$, and ${}_0\theta_z^k$ from time t to $t + \Delta t$ as the following equations

$$\mathbf{R}({}_0\boldsymbol{\theta}^k) = \mathbf{I} + \frac{\sin {}_0\theta^k}{{}_0\theta^k} \hat{\mathbf{R}}({}_0\boldsymbol{\theta}^k) + \frac{1 - \cos {}_0\theta^k}{{}_0\theta^k)^2} \hat{\mathbf{R}}({}_0\boldsymbol{\theta}^k)^2, \tag{2.9}$$

$${}_0\boldsymbol{\theta}^k = [{}_0\theta_x^k \quad {}_0\theta_y^k \quad {}_0\theta_z^k]^T, \quad {}_0\theta^k = \sqrt{({}_0\theta_x^k)^2 + ({}_0\theta_y^k)^2 + ({}_0\theta_z^k)^2} \tag{2.10}$$

$$\hat{\mathbf{R}}({}_0\boldsymbol{\theta}^k) = \begin{bmatrix} 0 & -{}_0\theta_z^k & {}_0\theta_y^k \\ {}_0\theta_z^k & 0 & -{}_0\theta_x^k \\ -{}_0\theta_y^k & {}_0\theta_x^k & 0 \end{bmatrix}. \tag{2.11}$$

The slip director vector ${}^{t+\Delta t}\mathbf{V}_s^k$ in the configuration at time $t + \Delta t$ is approximated in terms of the slip director vector at time t and the incremental nodal displacement

$${}^{t+\Delta t}\mathbf{V}_s^k = \frac{{}^{t+\Delta t}\mathbf{g}_x^k}{\|{}^{t+\Delta t}\mathbf{g}_x^k\|} \approx {}^t\mathbf{V}_s^k + \frac{1}{\|{}^t\mathbf{g}_x^k\|} \sum_{\xi=1}^q \frac{\partial h_\xi(r)}{\partial r} \Big|_{r=r_k} {}_0\mathbf{u}_\xi. \tag{2.12}$$

Substituting Eq. (2.8) and Eq. (2.12) into Eq. (2.6), the incremental displacement of sub-beam m belonging to layer n becomes

$$\begin{aligned}
{}_0\mathbf{u}^{(m)(n)} &= \sum_{k=1}^q h_k(r) {}_0\mathbf{u}_k + \sum_{k=1}^q h_k(r) \bar{y}_k^{(m)(n)} (\mathbf{R}({}_0\boldsymbol{\theta}^k) - \mathbf{I})^t \mathbf{V}_y^k + \sum_{k=1}^q h_k(r) \bar{z}_k^{(m)(n)} (\mathbf{R}({}_0\boldsymbol{\theta}^k) - \mathbf{I})^t \mathbf{V}_z^k \\
&\quad + \sum_{k=1}^q h_k(r) ({}_0\varphi_k^{(n)t} \mathbf{V}_s^k + ({}^t\varphi_k^{(n)} + {}_0\varphi_k^{(n)}) \left(\frac{1}{\|{}^t\mathbf{g}_x^k\|} \sum_{\xi=1}^q h'_\xi(r) {}_0\mathbf{u}_\xi \right)), \tag{2.13}
\end{aligned}$$

where ${}_0\varphi_k^{(n)}$ is the incremental layer DOF corresponding to the layer n at beam node k .

The finite rotation tensor $\mathbf{R}({}_0\boldsymbol{\theta}^k)$ in Eq. (2.9) is linearized by the use of the first-order Taylor polynomial approximation

$$\mathbf{R}({}_0\boldsymbol{\theta}^k) = \mathbf{I} + \sum_{n=1}^{\infty} \frac{1}{n!} \hat{\mathbf{R}}({}_0\boldsymbol{\theta}^k)^n \approx \mathbf{I} + \hat{\mathbf{R}}({}_0\boldsymbol{\theta}^k) \tag{2.14}$$

Substituting Eq. (2.14) into Eq. (2.13) and applying the first-order approximation, the linearized incremental displacement ${}_0\bar{\mathbf{u}}^{(m)(n)}$ for sub-beam m of layer n is obtained

$$\begin{aligned}
{}_0\mathbf{u}^{(m)(n)} \approx {}_0\bar{\mathbf{u}}^{(m)(n)} &= \sum_{k=1}^q h_k(r) {}_0\mathbf{u}_k + \sum_{k=1}^q h_k(r) \bar{y}_k^{(m)(n)} \hat{\mathbf{R}}({}_0\boldsymbol{\theta}^k)^t \mathbf{V}_y^k + \sum_{k=1}^q h_k(r) \bar{z}_k^{(m)(n)} \hat{\mathbf{R}}({}_0\boldsymbol{\theta}^k)^t \mathbf{V}_z^k \\
&\quad + \sum_{k=1}^q h_k(r) ({}_0\varphi_k^{(n)t} \mathbf{V}_s^k + {}^t\varphi_k^{(n)} \left\| \frac{1}{\|{}^t\mathbf{g}_x^k\|} \sum_{\xi=1}^q h'_\xi(r) {}_0\mathbf{u}_\xi \right\|) \tag{2.15}
\end{aligned}$$

2.3 Incremental equilibrium equations

For sub-beam m belonging to layer n , the covariant component of the Green–Lagrange strain in the configuration at time t referred to the configuration at time 0 is given by

$${}_0\tilde{\boldsymbol{\epsilon}}^{(m)(n)} = \frac{1}{2} ({}^t\mathbf{g}_i^{(m)(n)} \cdot {}^t\mathbf{g}_j^{(m)(n)} - {}_0\mathbf{g}_i^{(m)(n)} \cdot {}_0\mathbf{g}_j^{(m)(n)}) \quad \text{with} \quad {}^t\mathbf{g}_i^{(m)(n)} = \frac{\partial {}^t\mathbf{X}^{(m)(n)}}{\partial r_i}, \tag{2.16}$$

where ${}^t\mathbf{g}_i^{(m)(n)}$ is the covariant base vector and r_i indicates the natural coordinates (r, s, t) : $r_1 = r$, $r_2 = s$ and $r_3 = t$.

The covariant component of the incremental Green–Lagrange strain is obtained from the strains in the configurations at time $t + \Delta t$ and t

$${}_0\tilde{\boldsymbol{\epsilon}}^{(m)(n)} = {}^{t+\Delta t}\tilde{\boldsymbol{\epsilon}}^{(m)(n)} - {}^t\tilde{\boldsymbol{\epsilon}}^{(m)(n)} \tag{2.17}$$

and it can be decomposed into linear and nonlinear parts, ${}_0\tilde{\boldsymbol{e}}^{(mn)}$ and ${}_0\tilde{\boldsymbol{\eta}}^{(mn)}$, respectively

$${}_0\tilde{\boldsymbol{\varepsilon}}_{ij}^{(m)(n)} = {}_0\tilde{\boldsymbol{e}}_{ij}^{(m)(n)} + {}_0\tilde{\boldsymbol{\eta}}_{ij}^{(m)(n)} \quad (2.18)$$

with

$${}_0\tilde{\boldsymbol{e}}_{ij}^{(m)(n)} = \frac{1}{2} ({}^t\mathbf{g}_i^{(m)(n)} \cdot \frac{\partial {}_0\mathbf{u}^{(m)(n)}}{\partial r_j} + {}^t\mathbf{g}_j^{(m)(n)} \cdot \frac{\partial {}_0\mathbf{u}^{(m)(n)}}{\partial r_i}) \quad (2.19)$$

and

$${}_0\tilde{\boldsymbol{\eta}}_{ij}^{(m)(n)} = \frac{1}{2} \frac{\partial {}_0\mathbf{u}^{(m)(n)}}{\partial r_i} \cdot \frac{\partial {}_0\mathbf{u}^{(m)(n)}}{\partial r_j}. \quad (2.20)$$

The incremental Green–Lagrange strain defined in the local Cartesian coordinate system is evaluated through the following transformation

$${}_0\bar{\boldsymbol{e}}_{ij}^{(m)(n)} = ({}^0\mathbf{t}_i \cdot {}^0\mathbf{g}^{k(m)(n)}) ({}^0\mathbf{t}_j \cdot {}^0\mathbf{g}^{l(m)(n)}) {}_0\tilde{\boldsymbol{e}}_{kl}^{(m)(n)}, \quad (2.21)$$

$${}_0\bar{\boldsymbol{\eta}}_{ij}^{(m)(n)} = ({}^0\mathbf{t}_i \cdot {}^0\mathbf{g}^{k(m)(n)}) ({}^0\mathbf{t}_j \cdot {}^0\mathbf{g}^{l(m)(n)}) {}_0\tilde{\boldsymbol{\eta}}_{kl}^{(m)(n)}, \quad (2.22)$$

where ${}^0\mathbf{g}^{k(m)(n)}$ is the contravariant base vector calculated using ${}^0\mathbf{g}^{k(m)(n)} \cdot {}^0\mathbf{g}_l^{(m)(n)} = \delta_l^k$ and ${}^0\mathbf{t}_i$ is the base vector of the local Cartesian coordinate system given by

$${}^0\mathbf{t}_1 = h_k(r) {}^0\mathbf{V}_{\bar{x}}^k, \quad {}^0\mathbf{t}_2 = h_k(r) {}^0\mathbf{V}_{\bar{y}}^k \quad \text{and} \quad {}^0\mathbf{t}_3 = h_k(r) {}^0\mathbf{V}_{\bar{z}}^k. \quad (2.23)$$

In the total Lagrangian formulation, the principle of virtual work for a layered beam is given in the configuration at time $t + \Delta t$

$$\int_{0_V} {}^{t+\Delta t}\bar{S}_{ij} \delta {}^{t+\Delta t}\bar{\boldsymbol{\varepsilon}}_{ij} d^0V + \sum_i \int_{0_L} {}^{t+\Delta t}F_s^{(i)} \delta {}^{t+\Delta t}u_s^{(i)} d^0L = {}^{t+\Delta t}\mathfrak{R}, \quad (2.24)$$

in which 0V and 0L denote the volume and length of the beam, respectively, in the configuration at time 0 , ${}^{t+\Delta t}\bar{S}_{ij}$ is the local second Piola–Kirchhoff stress, ${}^{t+\Delta t}\bar{\boldsymbol{\varepsilon}}_{ij}$ is the local Green–Lagrange strain, ${}^{t+\Delta t}F_s^{(i)}$ and ${}^{t+\Delta t}u_s^{(i)}$ are the slip force per unit length and the slip displacement at interlayer i , respectively, ${}^{t+\Delta t}\mathfrak{R}$ is the external virtual work, and δ denotes virtual quantities.

After linearizing Eq. (2.24) with ${}^{t+\Delta t}F_s^{(i)} = {}^tF_s^{(i)} + {}_0F_s^{(i)}$, the following incremental equilibrium equation is obtained

$$\begin{aligned} & \int_{0_V} \bar{C}_{ijkl} {}_0\bar{\boldsymbol{e}}_{ij} \delta {}_0\bar{\boldsymbol{e}}_{kl} d^0V + \int_{0_V} {}^t\bar{S}_{ij} \delta {}_0\bar{\boldsymbol{\eta}}_{ij} d^0V + \sum_i \int_{0_L} K_s^{(i)} {}_0u_s^{(i)} \delta {}_0u_s^{(i)} d^0L \\ & = {}^{t+\Delta t}\mathfrak{R} - \int_{0_V} {}^t\bar{S}_{ij} \delta {}_0\bar{\boldsymbol{e}}_{ij} d^0V - \sum_i \int_{0_L} {}^tF_s^{(i)} \delta {}_0u_s^{(i)} d^0L, \end{aligned} \quad (2.25)$$

where \bar{C}_{ijkl} is the material law tensor for beams, ${}_0\bar{e}_{ij}$ and ${}_0\bar{\eta}_{ij}$ are the linear and nonlinear parts of the incremental local Green–Lagrange strain, and ${}_0u_s^{(i)}$ and ${}_0K_s^{(i)}$ are the incremental interlayer slip displacement and the corresponding connection stiffness at interlayer i , respectively.

The constitutive relations used in Eq. (2.25) are

$${}_0\bar{S}_{ij} = \bar{C}_{ijkl} {}_0\bar{e}_{kl} \quad \text{and} \quad {}_0F_s^{(i)} = {}_0K_s^{(i)} {}_0u_s^{(i)}, \quad (2.26)$$

where ${}_0\bar{S}_{ij}$ denotes the incremental second Piola–Kirchhoff stress and ${}_0F_s^{(i)}$ is the incremental slip force per unit length at interlayer i .

Expressing Eq. (2.25) as a sum of integrations over the volume of each sub-beam m of layer n in the configuration at time 0 (${}^0V^{(m)(n)}$),

$$\begin{aligned} & \sum_n \sum_m \int_{{}^0V^{(m)(n)}} \bar{C}_{ijkl}^{(m)(n)} {}_0\bar{e}_{ij}^{(m)(n)} \delta {}_0\bar{e}_{kl}^{(m)(n)} d{}^0V^{(m)(n)} + \sum_n \sum_m \int_{{}^0V^{(m)(n)}} {}^t\bar{S}_{ij}^{(m)(n)} \delta {}_0\bar{\eta}_{ij}^{(m)(n)} d{}^0V^{(m)(n)} \\ & + \sum_i \int_{{}^0L} {}_0K_s^{(i)} {}_0u_s^{(i)} \delta {}_0u_s^{(i)} d{}^0L = {}^{t+\Delta t}\mathfrak{R} - \sum_n \sum_m \int_{{}^0V^{(m)(n)}} {}^t\bar{S}_{ij}^{(m)(n)} \delta {}_0\bar{e}_{ij}^{(m)(n)} d{}^0V^{(m)(n)} - \sum_i \int_{{}^0L} {}^tF_s^{(i)} \delta {}_0u_s^{(i)} d{}^0L. \end{aligned} \quad (2.27)$$

In the beam formulation, only five covariant components of the Green–Lagrange strain are of interest, (i.e. $(i, j) \in \{(1, 1), (1, 2), (2, 1), (1, 3), (3, 1)\}$), and the material law tensor has only five non-zero components: $\bar{C}_{1111} = E$ and $\bar{C}_{1212} = \bar{C}_{2121} = \bar{C}_{1313} = \bar{C}_{3131} = G$ with Young’s modulus E and shear modulus G .

2.4 Finite element formulations

In a q -node continuum mechanics based beam element, the nodal DOFs vector ${}_0\mathbf{U}$ consists of the DOFs vector ${}_0\mathbf{U}_k$ at beam node k

$${}_0\mathbf{U} = \left[{}_0\mathbf{U}_1^T \quad {}_0\mathbf{U}_2^T \quad \dots \quad {}_0\mathbf{U}_q^T \right]^T \quad (2.28)$$

where ${}_0\mathbf{U}_k = \left[{}_0u_k \quad {}_0v_k \quad {}_0w_k \quad {}_0\theta_x^k \quad {}_0\theta_y^k \quad {}_0\theta_z^k \quad {}_0\varphi_k^{(1)} \quad \dots \quad {}_0\varphi_k^{(l)} \right]^T$. (2.29)

Employing Eq. (2.28), the incremental displacements ${}_0\bar{\mathbf{u}}^{(m)(n)}$ for sub-beam m of layer n in Eq. (2.15) is represented in terms of the nodal DOFs vector ${}_0\mathbf{U}$:

$${}_0\bar{\mathbf{u}}^{(m)(n)} = \left[\mathbf{L}_1^{(m)(n)} \quad \mathbf{L}_2^{(m)(n)} \quad \dots \quad \mathbf{L}_q^{(m)(n)} \right] {}_0\mathbf{U} = \mathbf{L}^{(m)(n)} {}_0\mathbf{U} \quad (2.30)$$

$$\text{where } \mathbf{L}_k^{(m)(n)} = \left[\begin{array}{c} \left(h_k(r) + {}^t\phi_k^{(n)}(r) \right) \mathbf{I} \quad -h_k(r) \left(\bar{y}_k^{(m)(n)} \hat{\mathbf{R}}({}^t\mathbf{V}_{\bar{y}}^k) + \bar{z}_k^{(m)(n)} \hat{\mathbf{R}}({}^t\mathbf{V}_{\bar{z}}^k) \right) \quad \mathbf{0} \\ +h_k(r) {}^t\mathbf{V}_s^k \mathbf{Q}^{(n)} \end{array} \right] \quad (2.31)$$

$$\text{with } {}^t\phi_k^{(n)}(r) = \sum_{\xi=1}^q \frac{\partial h_k(r)}{\partial r} \Big|_{r=r_\xi} h_\xi(r) \frac{{}^t\phi_\xi^{(n)}}{\|{}^t\mathbf{g}_x^\xi\|}, \quad (2.32)$$

and $\mathbf{Q}^{(n)}$ is a Boolean matrix for the layer DOFs ${}_0\phi_k^{(n)}$ such that

$${}_0\phi_k^{(n)} = \mathbf{Q}^{(n)} {}_0\mathbf{U}_k. \quad (2.33)$$

Similarly, the incremental slip displacement ${}_0\mathbf{u}_s^{(i)}$ at interlayer i is represented in terms of the nodal DOFs vector ${}_0\mathbf{U}$

$${}_0\mathbf{u}_s^{(i)} = \sum_{k=1}^q h_k(r) ({}_0\phi_k^{(b)} - {}_0\phi_k^{(a)}) = \mathbf{H}_s^{(i)} {}_0\mathbf{U}, \quad (2.34)$$

where $\mathbf{H}_s^{(i)}$ is the shape function matrix for the slip displacement at interlayer i , which is constructed according to the layer DOFs of the adjacent two layers a and b located on both sides of interlayer i .

The linear and nonlinear parts of the covariant Green–Lagrange strain in Eq. (2.19) and Eq. (2.20) are also expressed in terms of ${}_0\mathbf{U}$:

$${}_0\tilde{\mathbf{e}}_{ij}^{(m)(n)} = \frac{1}{2} \left({}^t\mathbf{g}_i^{(m)(n)} \cdot \frac{\partial \mathbf{L}^{(m)(n)}}{\partial r_j} + {}^t\mathbf{g}_j^{(m)(n)} \cdot \frac{\partial \mathbf{L}^{(m)(n)}}{\partial r_i} \right) {}_0\mathbf{U} = \mathbf{B}_{ij}^{(m)(n)} {}_0\mathbf{U}, \quad (2.35)$$

$${}_0\tilde{\boldsymbol{\eta}}_{ij}^{(m)(n)} = \frac{1}{2} {}_0\mathbf{U}^T \left(\frac{\partial \mathbf{L}^{(m)(n)}}{\partial r_i} \frac{\partial \mathbf{L}^{(m)(n)}}{\partial r_j} \right) {}_0\mathbf{U} = \frac{1}{2} {}_0\mathbf{U}^T \mathbf{N}_{ij}^{(m)(n)} {}_0\mathbf{U}. \quad (2.36)$$

The local Green–Lagrange strains are obtained using Eq. (2.21), Eq. (2.22), Eq. (2.35), and Eq. (2.36):

$${}_0\bar{\mathbf{e}}_{ij}^{(m)(n)} = ({}_0\mathbf{t}_i \cdot {}_0\mathbf{g}^{k(m)(n)}) ({}_0\mathbf{t}_j \cdot {}_0\mathbf{g}^{l(m)(n)}) \mathbf{B}_{kl}^{(m)(n)} {}_0\mathbf{U} = \bar{\mathbf{B}}_{ij}^{(m)(n)} {}_0\mathbf{U}, \quad (2.37)$$

$${}_0\bar{\boldsymbol{\eta}}_{ij}^{(m)(n)} = \frac{1}{2} {}_0\mathbf{U}^T ({}_0\mathbf{t}_i \cdot {}_0\mathbf{g}^{k(m)(n)}) ({}_0\mathbf{t}_j \cdot {}_0\mathbf{g}^{l(m)(n)}) \mathbf{N}_{kl}^{(m)(n)} {}_0\mathbf{U} = \frac{1}{2} {}_0\mathbf{U}^T \bar{\mathbf{N}}_{ij}^{(m)(n)} {}_0\mathbf{U}. \quad (2.38)$$

The virtual local Green–Lagrange strains and the virtual interlayer slip displacement are

$$\delta {}_0\bar{\mathbf{e}}_{ij}^{(m)(n)} = \bar{\mathbf{B}}_{ij}^{(m)(n)} \delta {}_0\mathbf{U}, \quad \delta {}_0\bar{\boldsymbol{\eta}}_{ij}^{(m)(n)} = \delta {}_0\mathbf{U}^T \bar{\mathbf{N}}_{ij}^{(m)(n)} {}_0\mathbf{U} \quad \text{and} \quad \delta {}_0\mathbf{u}_s^{(i)} = \mathbf{H}_s^{(i)} \delta {}_0\mathbf{U}. \quad (2.39)$$

Substituting Eq. (2.34) and Eqs. (2.37)–(2.39) into Eq. (2.27), the following finite element formulation is obtained with the tangent stiffness matrix ${}^t\mathbf{K}$:

$${}^t\mathbf{K}_0 \mathbf{U} = {}^{t+\Delta t}\mathbf{R} - {}^t_0\mathbf{F}_i \quad \text{with} \quad {}^t\mathbf{K} = {}^t\mathbf{K}_L + {}^t\mathbf{K}_{NL} + {}^t\mathbf{K}_s, \quad (2.40)$$

$$\text{where } {}^t\mathbf{K}_L = \sum_n \sum_m \int_{0V^{(m)(n)}} \bar{\mathbf{B}}_{ij}^{(m)(n)\text{T}} {}_0\bar{\mathbf{C}}_{ijkl} \bar{\mathbf{B}}_{kl}^{(m)(n)} dV^{(m)(n)}, \quad (2.41)$$

$${}^t\mathbf{K}_{NL} = \sum_n \sum_m \int_{0V^{(m)(n)}} \bar{\mathbf{N}}_{ij}^{(m)(n)} {}^t\bar{\mathbf{S}}_{ij} dV^{(m)(n)}, \quad (2.42)$$

$${}^t\mathbf{K}_s = \sum_i \int_{0L} \mathbf{H}_s^{(i)\text{T}} {}_0K_s^{(i)} \mathbf{H}_s^{(i)} d^0L, \quad (2.43)$$

$${}^t_0\mathbf{F} = \sum_n \sum_m \int_{0V^{(m)(n)}} \bar{\mathbf{B}}_{ij}^{(m)(n)\text{T}} {}^t\bar{\mathbf{S}}_{ij} dV^{(m)(n)} + \sum_i \int_{0L} \mathbf{H}_s^{(i)\text{T}} {}^tF_s^{(i)} dL. \quad (2.44)$$

The complete tangent stiffness matrix for the layered beam analysis can be constructed by the assemblage of the elemental stiffness matrices using the direct stiffness procedure. Because the layer DOF ${}_0\varphi_k^{(n)}$ on the reference layer is fixed as mentioned before, the actual number of DOFs used for an l -layer beam is $(6 + l - 1)$ (three translations, three rotations, and $(l - 1)$ layer DOFs) at each beam node. In 2D analysis of layered beams, $(3 + l - 1)$ DOFs (two translations, one rotation, and $(l - 1)$ layer DOFs) are required.

The incremental displacement ${}_0\mathbf{U}$ is obtained in each incremental step by solving Eq. (2.40). Then, the position of each beam node k and the layer DOFs at beam node k are additively updated as

$${}^{t+\Delta t}\mathbf{x}_k = {}^t\mathbf{x}_k + \begin{bmatrix} {}_0\mathbf{u}_k \\ {}_0\mathbf{v}_k \\ {}_0\mathbf{w}_k \end{bmatrix} \quad \text{and} \quad {}^{t+\Delta t}\varphi_k^{(n)} = {}^t\varphi_k^{(n)} + {}_0\varphi_k^{(n)}. \quad (2.45)$$

2.5 Numerical examples

In this section, we demonstrate the modeling capability and performance of the continuum mechanics based beam element in linear and nonlinear analyses of layered beams. To model the layered beams, 2-node continuum mechanics based beam elements are used, and the reduced integration scheme is adopted along the beam length direction to avoid shear locking [26]. For the cross-section modeling, 4-node or 16-node cross-sectional elements are used, and 2×2 and 4×4 Gauss integrations are performed on each cross-sectional element, respectively.

In order to solve nonlinear equilibrium equations, the standard full Newton–Raphson iterative scheme is used. Material nonlinearities in beam layers are implemented using the von Mises plasticity model with linear isotropic hardening law, and the nonlinear load-slip relationship at the interlayers is modeled using a 1D nonlinear constitutive model corresponding to the particular connection properties. At each integration point in the layered beam model, the constitutive equations are implicitly solved using the return mapping scheme [32].

In order to assess the proposed beam finite element, the results obtained from the present beam model are compared with the reference solutions, which are obtained from previous analytical or experimental studies or from 3D solid element models in the commercial software ADINA [33]. In the 3D solid element models, the whole layered beam structures are modeled by using 27-node 3D solid elements where the interlayers are modeled as thin solid layers with thickness $t_s^{(i)}$, which is chosen to be $1/1000^{\text{th}}$ of the beam height. The orthotropic material model is adopted to model the slip behaviors allowing only longitudinal slips in the interlayer zone, in which the shear modulus corresponding to the longitudinal slip at interlayer i is given as $G_s^{(i)} = K_s^{(i)} t_s^{(i)} / b_s^{(i)}$ wherein $b_s^{(i)}$ and $t_s^{(i)}$ are the width and thickness, respectively, of interlayer i . The other material moduli are restrained by large values (ten thousand times the shear modulus) to prevent uplift and slip in other directions. Throughout the following numerical examples E denotes Young’s modulus, and Poisson’s ratio is considered to be zero. Incremental nonlinear analysis is performed unless otherwise mentioned.

2.5.1 Simply supported two-layer beam

Consider a two-layer simply supported beam with a deformable interlayer as shown in Fig. 3(a). The beam is subjected to both uniformly distributed transverse and axial loads. The interlayer behavior is characterized by a linear load-slip relation with a constant connection stiffness, $K_s = 50 \text{ MN/m}^2$. This problem was analyzed first by Girhammar and Gopu [7] with closed form solutions and has been studied in several other researches [14–16].

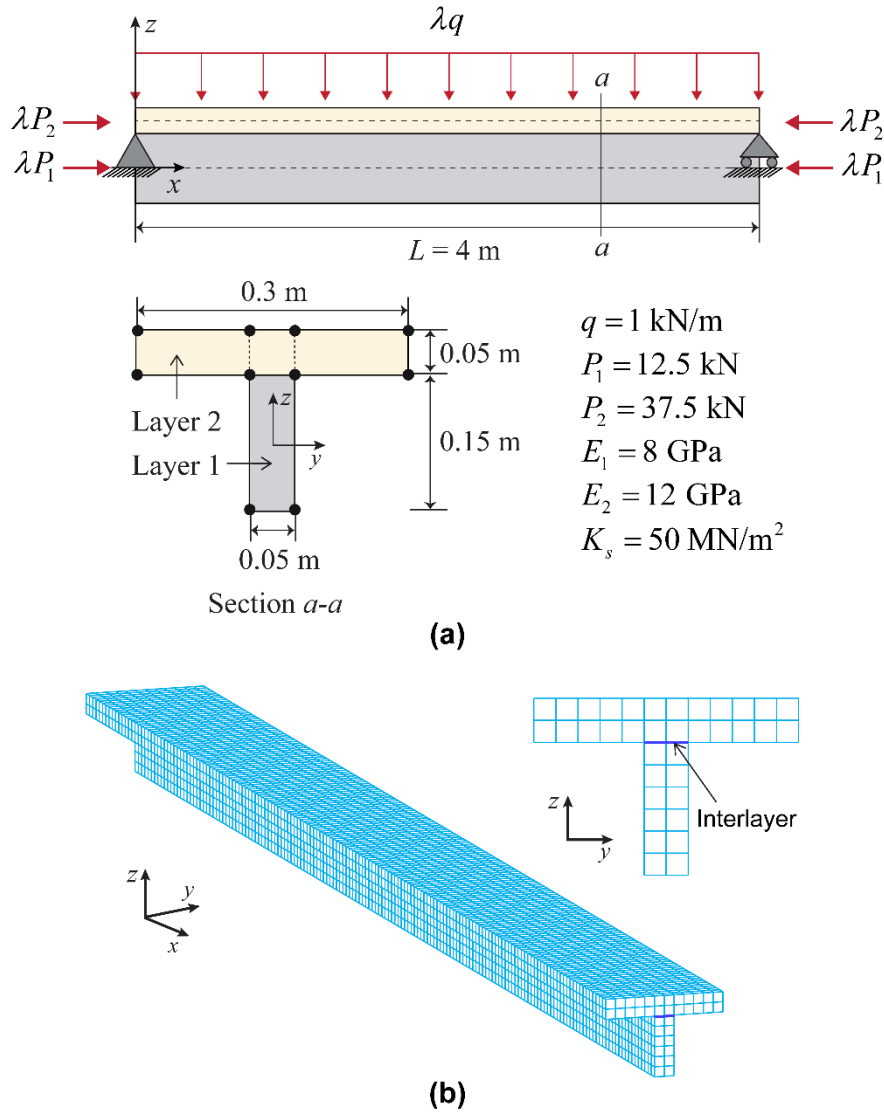


Fig. 3. Simply supported two-layer beam problem: (a) Problem description (E denotes Young's modulus) and (b) Solid element model used to obtain reference solutions.

The beam is modeled using 20 continuum mechanics based beam elements ($21 \times 7 = 147$ DOFs) and the cross-section is discretized with four 4-node cross-sectional elements (Fig. 3(a)). The load levels of both the transverse and axial loads increase equally by employing a magnification factor λ . For comparison, the beam with a rigid interlayer connection is also considered and this case is modeled as a single layer beam without interlayer. In order to obtain reference solutions, 27-node solid elements (6,080 elements and 187,725 DOFs) are used in the solid element model presented in Fig. 3(b). Both transverse and axial loads are applied to the solid element model by employing equivalent pressures.

Fig. 4 shows the load-displacement curves for the z -directional displacement w at the midpoint of the beam in both the cases of rigid ($K_s = \infty$) and deformable ($K_s = 50 \text{ MN/m}^2$) interlayer connections. The present beam model well exhibits the nonlinear response due to the interaction between bending and compression. As expected, the presence of the deformable interlayer increases the deflections and nonlinearity. Table 1 presents the maximum z -directional displacements w at the midpoint of the beam for four load levels ($\lambda = 0.5, 1, 1.5$, and 2).

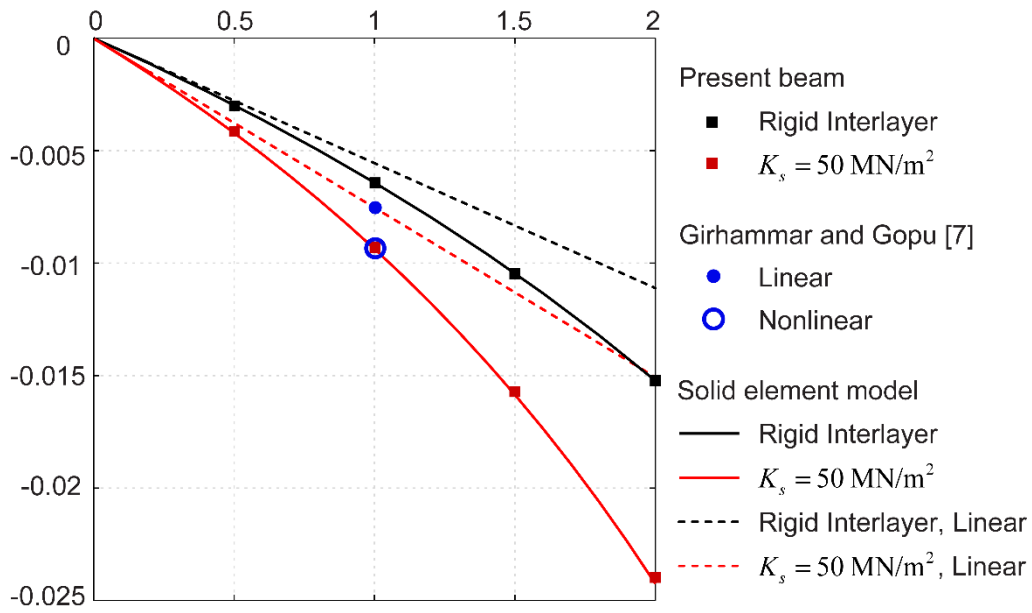


Fig. 4. Load-displacement curves for the z -directional displacement w at the midpoint of the beam obtained from the present beam and solid element model in the simply supported two-layer beam problem.

Table 1. z -directional displacement w at the midpoint of the beam for four load levels ($\lambda = 0.5, 1, 1.5$, and 2) in the simply supported two-layer beam problem (unit: m).

	w at $x = L/2$			
	$\lambda = 0.5$	$\lambda = 1$	$\lambda = 1.5$	$\lambda = 2$
Present beam	-4.171E-03	-9.266E-03	-1.567E-02	-2.396E-02
Solid element model	-4.201E-03	-9.321E-03	-1.585E-02	-2.425E-02
Girhammar and Gopu [7] (Analytical)	-	-9.276E-03	-	-
P. Krawczyk and B. Rebora [14]	-	-9.276E-03	-	-
Saje et al [15]	-	-9.274E-03	-	-
Battini et al [16]	-	-9.249E-03	-	-

2.5.2 Simply supported two-layer tapered beam

A simply supported two-layer tapered beam, which has varying cross-sections along the beam length, is considered as shown in Fig. 5(a). The geometric and material properties of the beam are similar to those of the two-layer beam problem in Section 2.5.1; however, the cross-sectional dimensions linearly decrease from $x = 0$ to $x = L$, except for the thicknesses of both the layers (b_1 and h_2). The cross-sectional dimension of the beam at a distance x is defined by $\alpha(x)$, which is a linearly decreasing function from α_0 (at $x = 0$) to α_L (at $x = L$). In this problem, several varying cross-sectional geometries of the beam are tested according to various α_L values (from $\alpha_L = 0.3$ to 0.9) with a constant $\alpha_0 = 1$. The beam is subjected to a uniformly distributed transverse load, $q = 1 \text{ kN/m}$. The constant connection stiffness for a deformable interlayer is $K_s = 50 \text{ MN/m}^2$.

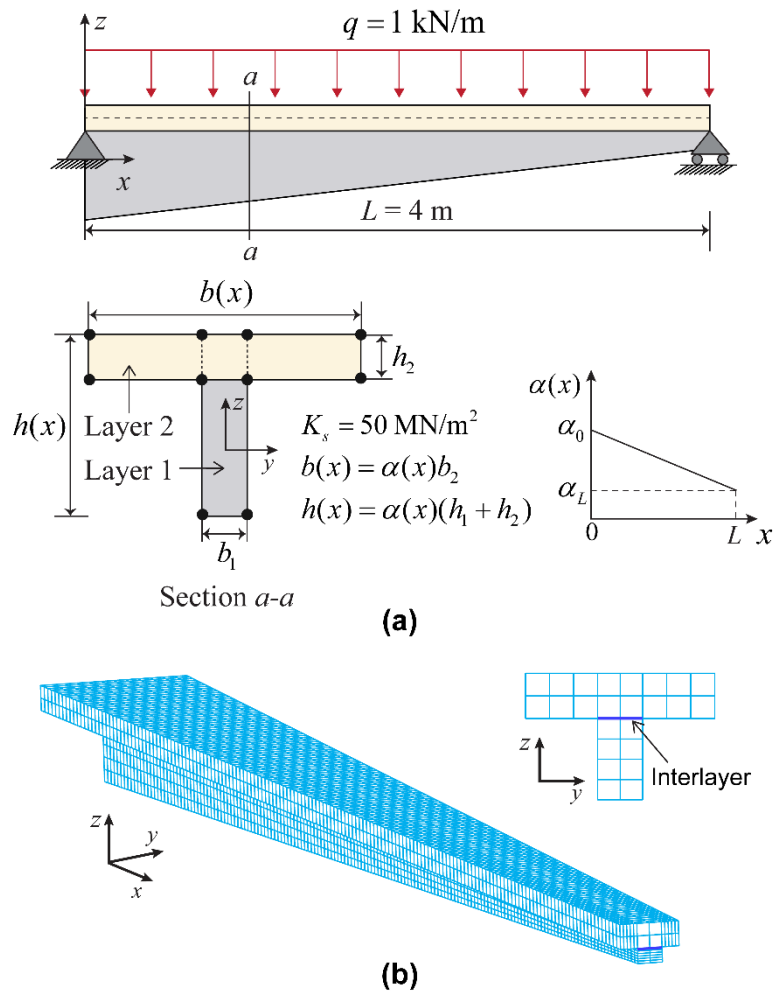


Fig. 5. Simply supported two-layer tapered beam: (a) Problem description where $b_1 = 0.05 \text{ m}$, $b_2 = 0.3 \text{ m}$, $h_1 = 0.15 \text{ m}$, and $h_2 = 0.05 \text{ m}$ and (b) Solid element model used to obtain reference solutions.

The beam is modeled using 20 continuum mechanics based beam elements ($21 \times 7 = 147$ DOFs) and the cross-section is discretized with four 4-node cross-sectional elements. The reference solutions are obtained using 27-node solid elements (6,080 elements and 187,725 DOFs) as shown in Fig. 5(b). The linear analysis is performed.

Fig. 6 shows the maximum deflections w_{\max} obtained for various α_L values. The present beam model exhibits good agreement with the reference solutions, even when α_L becomes small where the cross-sectional dimension changes sharply along the beam length. Table 2 presents the maximum deflections w_{\max} for the four values of α_L .

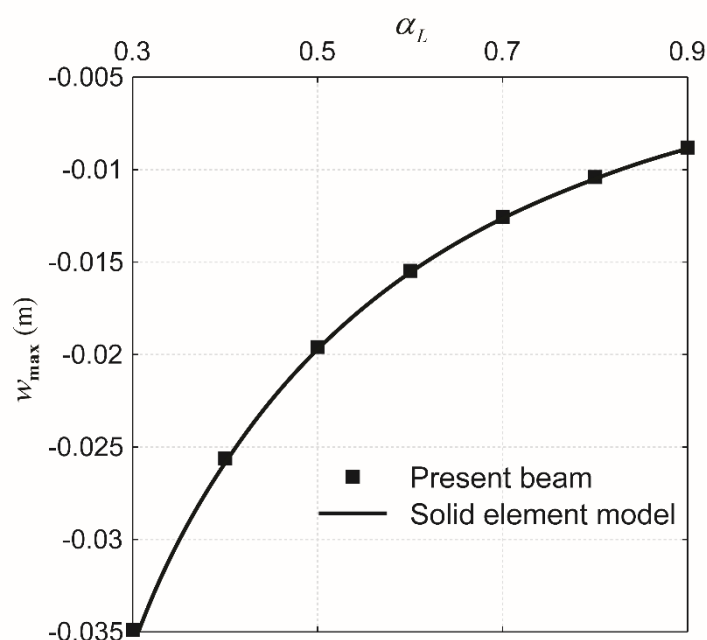


Fig. 6. Maximum deflections of the beam according to α_L in the simply supported two-layer tapered beam problem.

Table 2. Maximum displacement w_{\max} calculated in four cases of varying cross-sectional geometries ($\alpha_L = 0.3, 0.5, 0.7$, and 0.9) in the simply supported two-layer beam with varying cross-section problem (unit: m).

	Maximum displacement w_{\max}			
	$\alpha_L = 0.3$	$\alpha_L = 0.5$	$\alpha_L = 0.7$	$\alpha_L = 0.9$
Present beam	-3.4884E-02	-1.9590E-02	-1.2545E-02	-8.8043E-03
Solid element model	-3.5305E-02	-1.9697E-02	-1.2635E-02	-8.8764E-03

2.5.3 Roll-up of a cantilever cross-shaped three-layer beam

Consider a cantilever cross-shaped three-layer beam subjected to tip bending moment M_y as shown in Fig. 7. The beam is clamped at $x = 0$, and the interlayer connection stiffnesses are zero ($K_s^{(1)} = K_s^{(2)} = 0$). A similar problem of cantilever beam that has two layers was previously discussed in Refs. [14, 16]. The beam is modeled by 20 continuum mechanics based beam elements ($21 \times 7 = 147$ DOFs), and the cross-section is discretized using five 4-node cross-sectional elements.

The analytical relation between the tip bending moment M_y and roll-up angle θ of Layer 3 is given by

$$M_y = M_1 + M_2 + M_3, \quad M_i = \frac{E_i I_i}{R_i}, \quad I_i = \frac{b_i h_i^3}{12} \quad (2.46)$$

$$\text{with } R_3 = \frac{L}{\theta}, \quad R_2 = R_3 + \frac{1}{2}(h_2 + h_3), \quad R_1 = R_3 + \frac{1}{2}(h_1 + 2h_2 + h_3). \quad (2.47)$$

The corresponding interlayer slips, s_1 and s_2 , are evaluated using the following equations

$$s_1(x) = (R_2 + \frac{1}{2}h_2)(\frac{1}{R_2} - \frac{1}{R_1})x, \quad s_2(x) = (R_2 - \frac{1}{2}h_2)(\frac{1}{R_3} - \frac{1}{R_2})x. \quad (2.48)$$

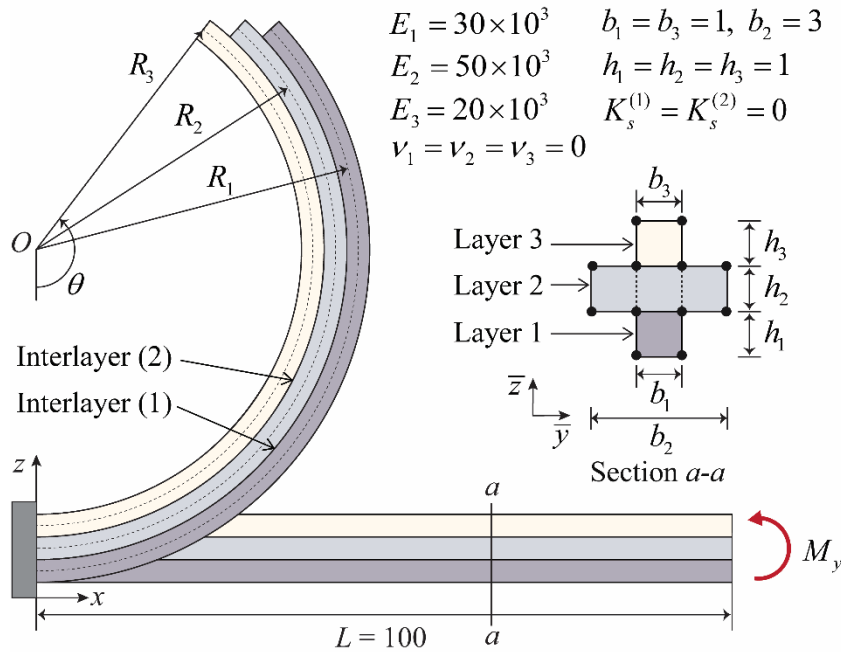


Fig. 7. Cantilever cross-shaped three-layer beam subjected to tip bending moment M_y .

The results obtained from the present beam model are compared with the analytically calculated solutions. Fig. 8(a) shows the deformed shapes of the beam when the roll-up angle θ becomes $\theta = \pi/2$, π , $3\pi/2$, and 2π . Figs. 8(b) and (c) show the load-displacement curves for the x - and z -directional displacements (u and w) at the free tip with respect to the tip bending moment M_y . Fig. 9 presents the load-slip displacement curves at the free tip. The results demonstrate that the present beam model shows good agreement with the analytical model, and well predicts a large rotation behavior of the layered beam such that the roll-up angle becomes $\theta = 2\pi$.

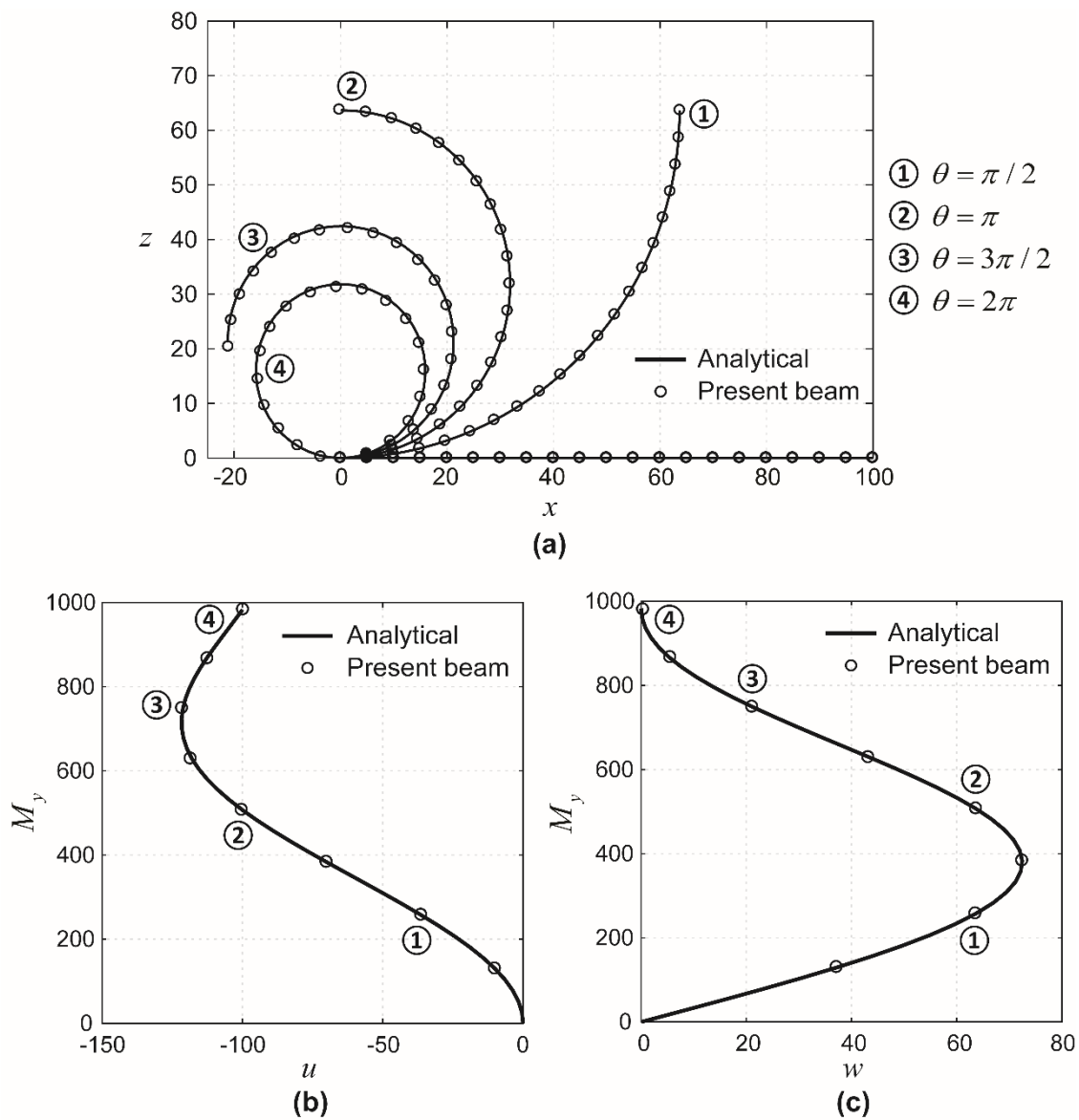


Fig. 8. Numerical results in the cantilever cross-shaped three-layer beam problem: (a) Deformed shapes of the beam at four load levels when $\theta = \pi/2$, π , $3\pi/2$, and 2π , and (b) and (c) Load-displacement curves of x - and z -directional displacements (u and w) at the free tip.

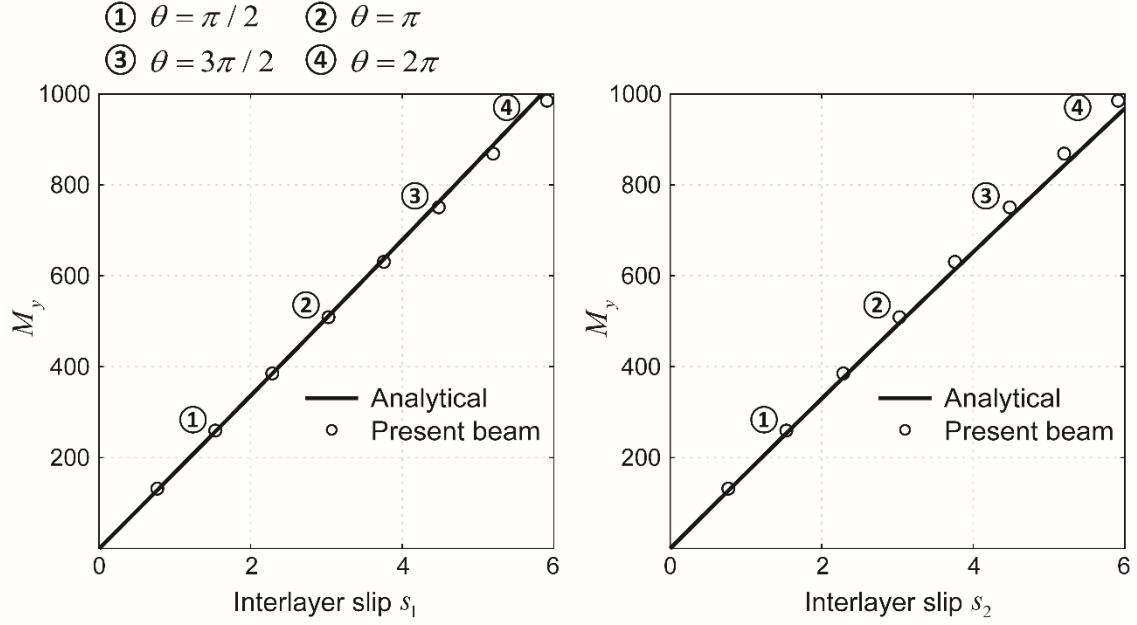


Fig. 9. Load-slip displacement curves at the free tip of the beam in the cantilever cross-shaped three-layer beam problem.

2.5.4 Buckling of a simply supported two-layer beam

Consider buckling of a simply supported two-layer beam with a deformable interlayer of constant connection stiffness $K_s = 49 \text{ MN/m}^2$ as shown Fig. 10. At the end of the beam, an axial load P is applied on the cross-section of Layer 1 with a z -directional eccentricity e , which is measured from the center line of Layer 1. Three eccentricities are considered: 0.015 m, 0.01325 m, and 0.0115 m. The beam is simply supported at the loading points.

The beam is modeled using 30 continuum mechanics based beam elements ($31 \times 7 = 217$ DOFs) and the cross-section is discretized using four 4-node cross-sectional elements. In order to calculate the load vector for the beam model, the eccentric axial load P on Layer 1 is considered as a uniform axial pressure $P/A^{(1)(1)}$, and a moment $M_y = Pe$. The load vector for the beam element at $x = L$ is calculated using the following equation:

$${}^{t+\Delta t}\mathbf{R}_e = \int_{A^{(1)(1)}} \mathbf{L}^{(1)(1)T} \Big|_{r=r'} \mathbf{f}^{(1)(1)} dA^{(1)(1)} + [0 \ 0 \ 0 \ 0 \ M_y \ 0 \ 0]^T, \quad (2.49)$$

where superscript (1)(1) indicates a cross-sectional element (1) belonging to Layer 1 (see the cross-sectional modeling in Fig. 10), $\mathbf{L}^{(1)(1)}$ is the interpolation matrix in Eq. (2.30), $\mathbf{f}^{(1)(1)} = [P/A^{(1)(1)} \quad 0 \quad 0]^T$ (N/m²), and r' is the natural coordinate at $x = L$. The load vector for the beam element at $x = 0$ is obtained similarly.

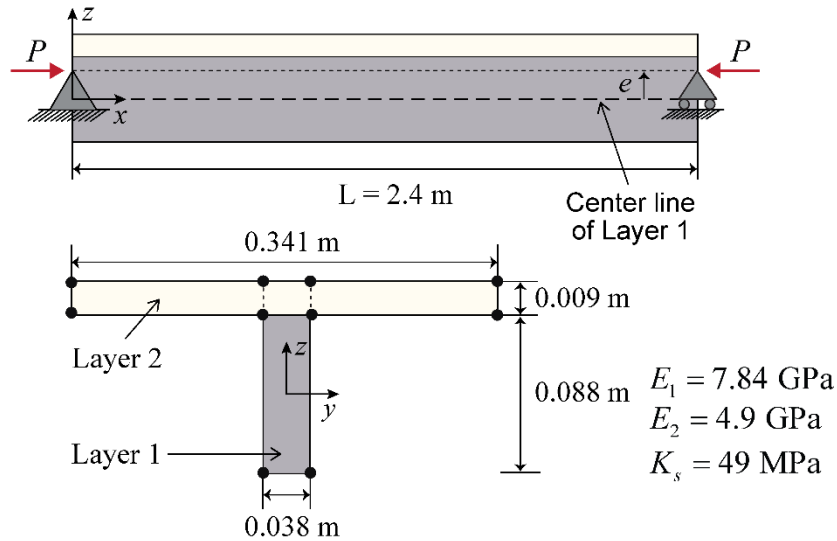


Fig. 10. Buckling of simply supported two-layer beam subjected to axial load P with an eccentricity e .

Table 3. z -directional displacement w at the midpoint of the beam in three cases of eccentricities e in the buckling of the simply supported two-layer beam problem (unit: m).

		w at $x = L/2$		
		$P = 10$ kN	$P = 20$ kN	$P = 40$ kN
Kamiya [6] (Analytical)	$e = 0.015$ m	-3.6039E-04	-9.5737E-04	-4.4805E-03
	$e = 0.01325$ m	8.5568E-05	1.7726E-04	3.8231E-04
	$e = 0.0115$ m	5.3153E-04	1.3119E-03	5.2451E-03
Present beam	$e = 0.015$ m	-3.6094E-04	-9.6009E-04	-4.5426E-03
	$e = 0.01325$ m	8.5709E-05	1.7879E-04	3.9762E-04
	$e = 0.0115$ m	5.3239E-04	1.3180E-03	5.3430E-03

Fig. 11 compares the deflection curves along the beam length at three load levels ($P = 10$ kN, 20 kN, and 40 kN) in each case of eccentricity with the analytical solutions obtained from Ref. [6]. As shown in Fig. 11, the buckling mode shapes change depending on the eccentricities. The present beam model exhibits good agreement with the analytical solutions. Table 3 shows the deflection at the midpoint of the beam for each case.

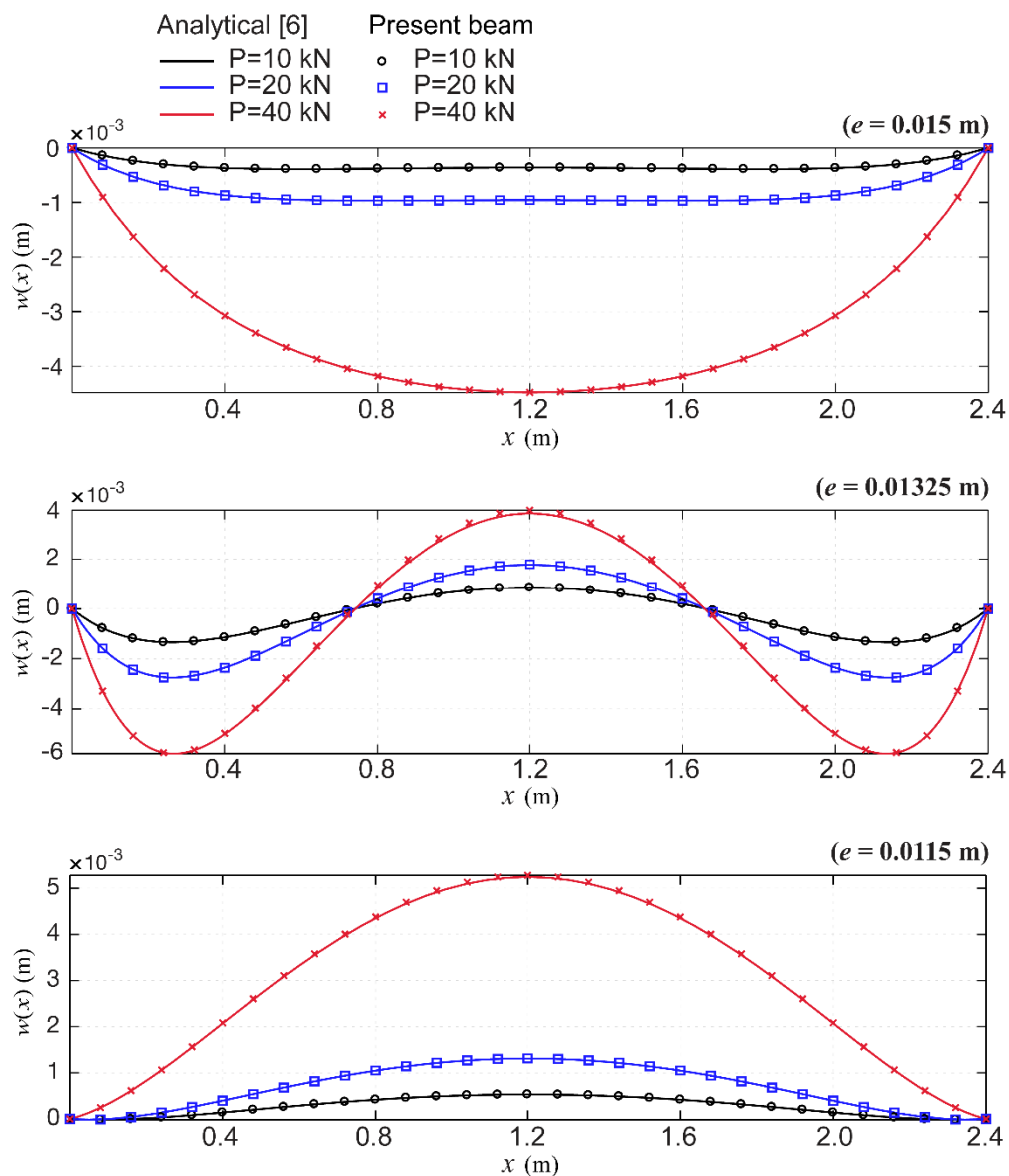


Fig. 11. Deflection curves along the beam length according to three eccentricities e (0.015 m, 0.01325 m, and 0.0115 m) in the buckling of two-layer simply supported beam.

2.5.5 Cantilever four-layer sandwich beam

A cantilever four-layer sandwich beam has three deformable interlayers as shown in Fig. 12(a). The beam is composed of two elasto-plastic materials: Material 1 for Layers 1 and 4 (colored gray) and Material 2 for Layers 2 and 3 (colored yellow). As seen in Fig. 12(a):

- **Material cases**
 - Material 1: Young's modulus $E_1 = 200$ GPa , initial yield stress $Y_1 = 100$ MPa , and linear hardening modulus $H_1 = 5$ GPa .
 - Material 2: Young's modulus $E_2 = 50$ GPa , initial yield stress $Y_2 = 80$ MPa , and linear hardening modulus $H_2 = 20$ GPa .

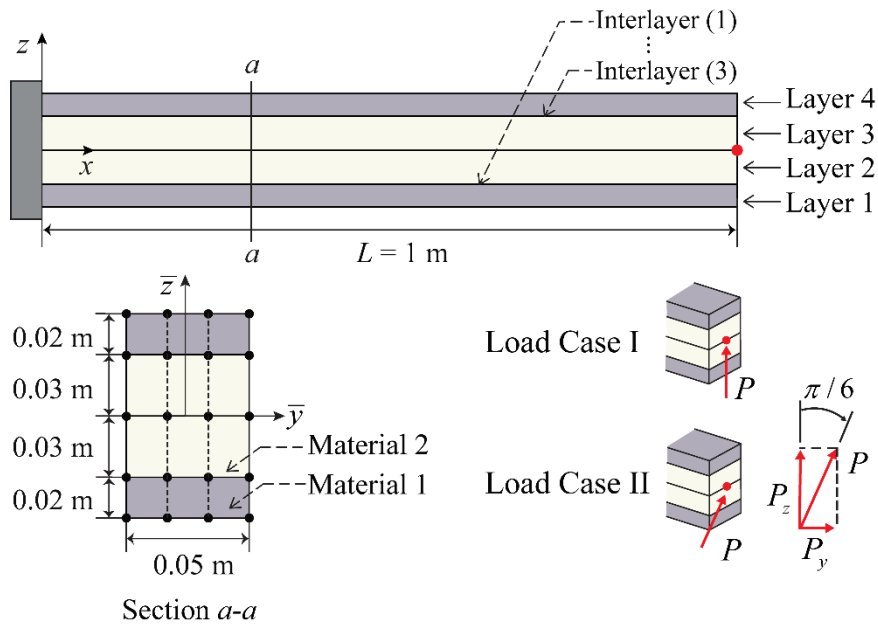
Two load cases and two interlayer cases are considered as follows:

- **Load cases**
 - Load Case I: A shear force P is applied at the free tip in the z -direction.
 - Load Case II: A shear force P is applied at the free tip at an angle of $\pi / 6$ with respect to the z -direction.
- **Interlayer cases**
 - Interlayer Case I : $K_s^{(1)} = 200$ MN/m² , $K_s^{(2)} = 500$ MN/m² , $K_s^{(3)} = 100$ MN/m²
 - Interlayer Case II : $K_s^{(1)} = 80$ MN/m² , $K_s^{(2)} = 300$ MN/m² , $K_s^{(3)} = 40$ MN/m²

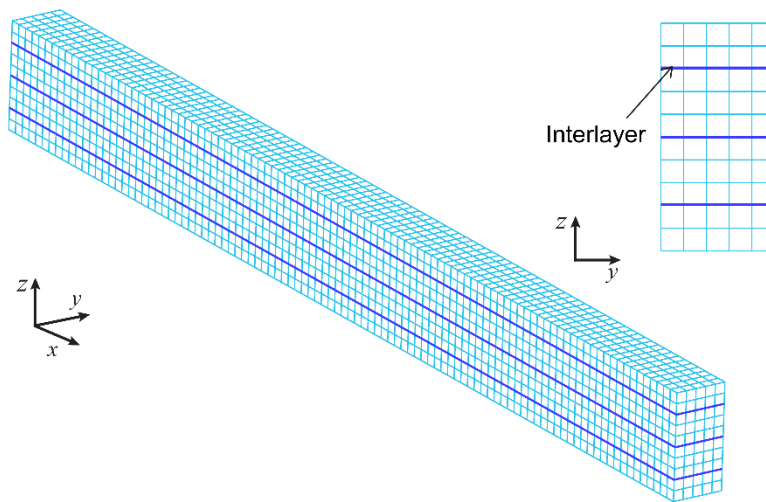
The beam is modeled using 10 continuum mechanics based beam elements ($11 \times 9 = 99$ DOFs). The cross-section of each layer is discretized by three 4-node cross-sectional elements; thus, twelve 4-node cross-sectional elements are used in total. In order to capture the elasto-plastic behavior accurately, 4×4 Gauss integration points are used in each cross-sectional element. For comparison, the beam with rigid interlayer connections is also considered, and this case is modeled as a single layer beam without interlayers.

To obtain reference solutions, 27-node solid elements (6,500 elements and 178,200 DOFs) are used in the solid element model presented in Fig. 12(b). The shear forces in both Load Cases I and II are applied to the solid element model using equivalent pressures at the free tip ($x = L$). In the calculation of the reference solutions, 50 load steps are used.

Fig. 13(a) shows the load-displacement curves for the z -directional displacement w at the free tip when Load Case I is considered. Good agreements are observed with the reference solutions. Figs. 13(b) and (c) show the von Mises stress distributions on the cross-section at $x = L/2$ obtained from the present beam and solid element models, respectively, when $P = 15$ kN. Table 4 presents the displacement w at the free tip under $P = 15$ kN in Load Case I.

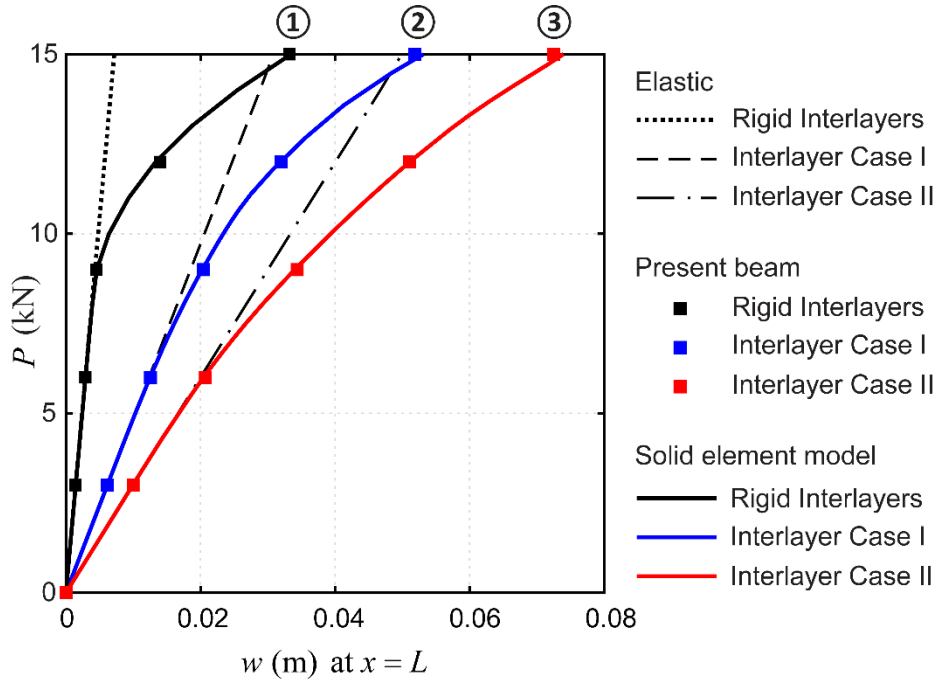


(a)

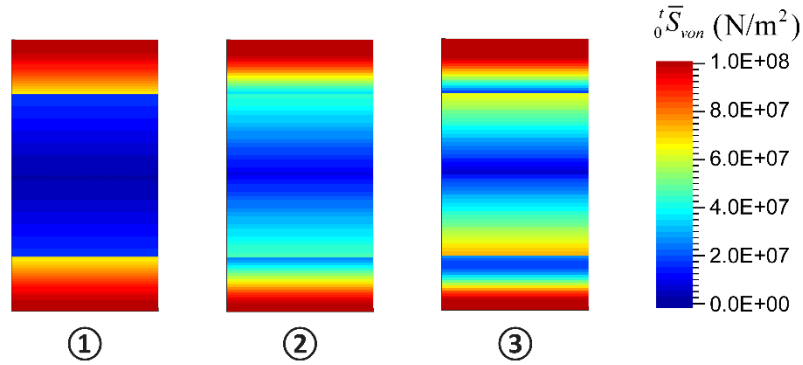


(b)

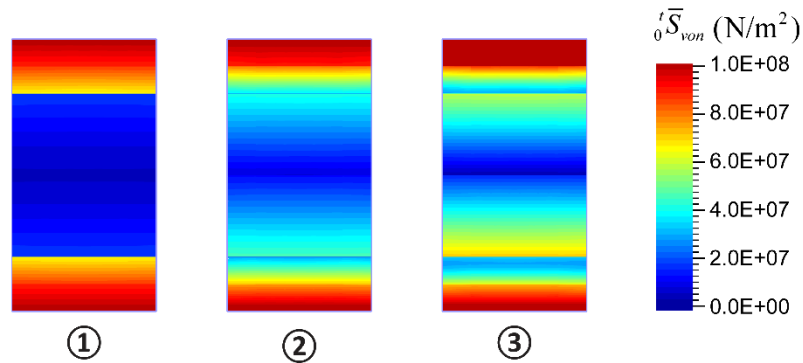
Fig. 12. Cantilever four-layer sandwich beam problem: (a) Problem description and (b) Solid element model used to obtain reference solutions.



(a)



(b)



(c)

Fig. 13. Numerical results in Load Case I for the cantilever four-layer sandwich beam problem: (a) Load-displacement curves for z-directional displacement w at the free tip, and (b) and (c) Distributions of the von Mises stress obtained from the present beam and solid element models, respectively, when $P = 15$ kN .

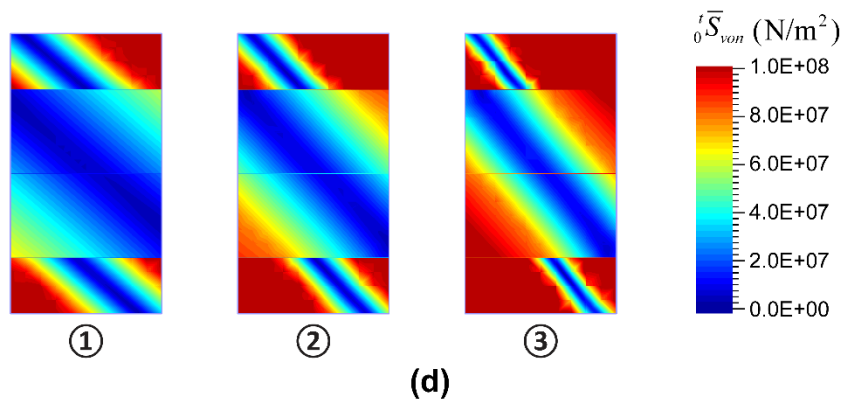
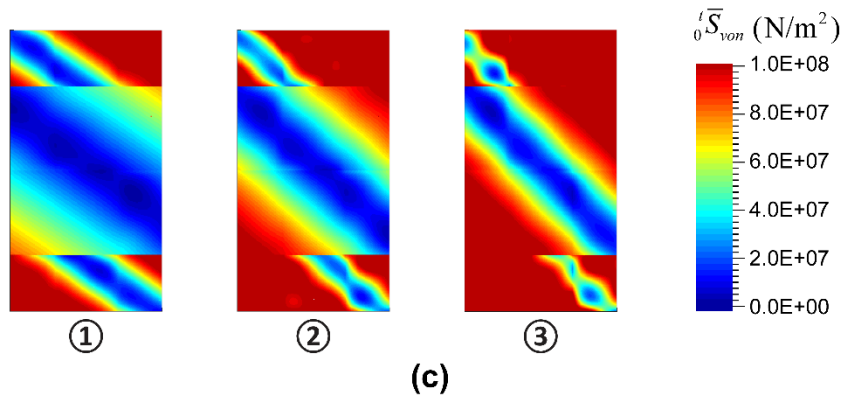
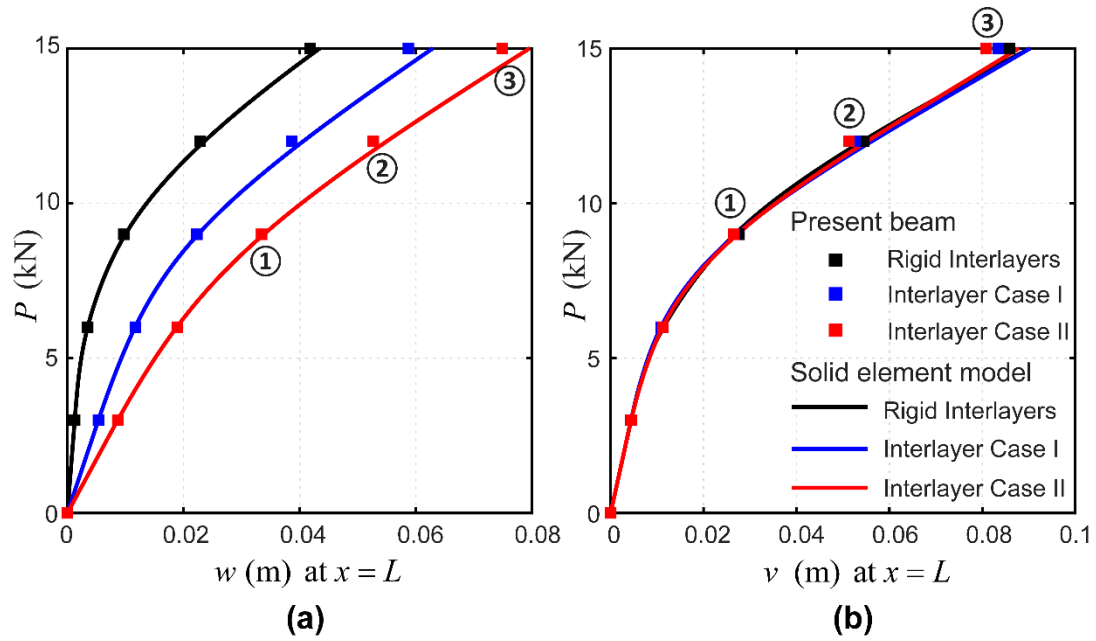


Fig. 14. Numerical results in Load Case II for the cantilever four-layer sandwich beam problem: (a) and (b) Load-displacement curves for z - and y -directional displacements (w and v) at the free tip, and (c) and (d) Distributions of the von Mises stress obtained from the present beam and solid element model, respectively, when $P = 9 \text{ kN}$, 12 kN , and 15 kN in Interlayer Case II.

Figs. 14(a) and (b) show the load-displacement curves for the displacements w and v at the free tip in Load Case II. Whereas the interlayer connection stiffness considerably influences the z -directional displacement w , the effect is largely negligible in the y -directional displacement v . Figs. 14(c) and (d) show the von Mises stress distributions on the cross-section at $x = L/2$ obtained from the present beam and solid element models, respectively, as P increases ($P = 9 \text{ kN}$, 12 kN , and 15 kN) in Interlayer Case II. Table 5 presents the displacements w and v at the free tip in Load Case II.

Table 4. z -directional displacement w at the free tip under $P = 15 \text{ kN}$ in Load Case I of the cantilever four-layer sandwich beam problem (unit: m).

	Displacement w at $x = L$		
	Rigid interlayers	Interlayer Case I	Interlayer Case II
Elastic	7.1865E-03	3.0842E-02	4.9919E-02
Present beam	3.3237E-02	5.1889E-02	7.2552E-02
Solid element model	3.3449E-02	5.3144E-02	7.4146E-02

Table 5. z - and y -directional displacements (w and v) at the free tip under $P = 15 \text{ kN}$ in Load Case II of the cantilever four-layer sandwich beam problem (unit: m).

		Displacement at $x = L$		
		Rigid interlayers	Interlayer Case I	Interlayer Case II
w	Present beam	4.2796E-02	5.8710E-02	7.4860E-02
	Solid element model	4.3466E-02	6.2934E-02	7.9601E-02
v	Present beam	8.6832E-02	8.3405E-02	8.0849E-02
	Solid element model	9.0285E-02	8.9372E-02	8.7854E-02

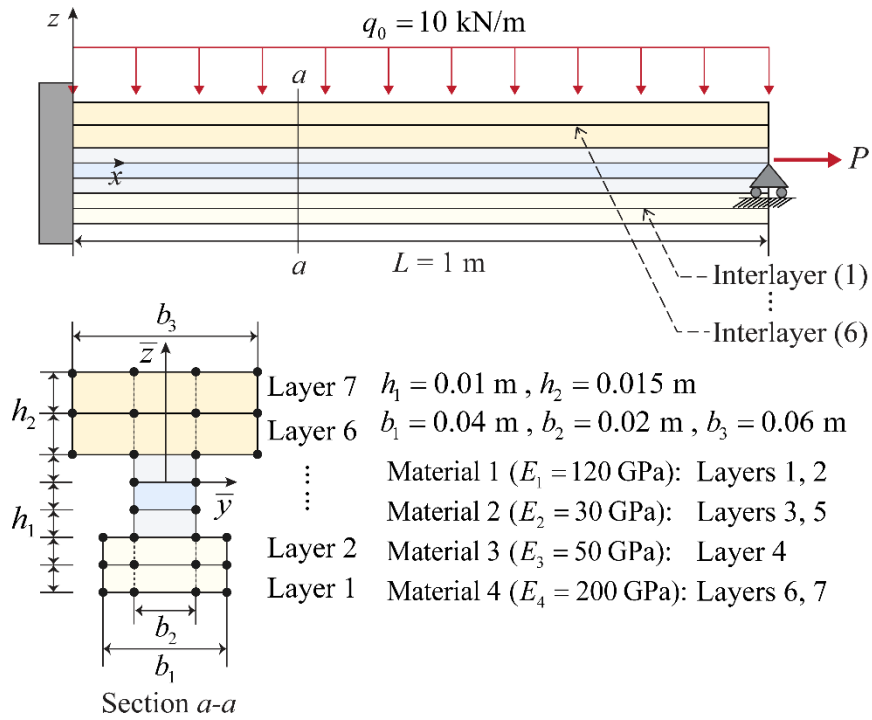
2.5.6 Seven-layer I-section beam

Let us consider a seven-layer I-section beam subjected to both a uniformly distributed transverse load $q_0 = 10 \text{ kN/m}$ and a tip axial load P as shown in Fig. 15(a). The beam is fully clamped at $x = 0$ and hinged at $x = L$. The beam is composed of four elastic materials (Materials 1, 2, 3, and 4), see Fig. 15(a).

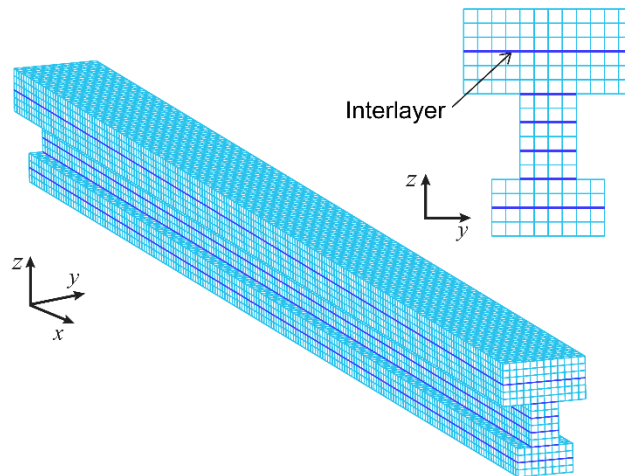
Two interlayer cases are considered:

- **Interlayer cases**

- Interlayer Case I: $K_s^{(1)} = 150 \text{ MN/m}^2$, $K_s^{(2)} = K_s^{(5)} = 80 \text{ MN/m}^2$,
 $K_s^{(3)} = K_s^{(4)} = 50 \text{ MN/m}^2$, $K_s^{(6)} = 100 \text{ MN/m}^2$
- Interlayer Case II: $K_s^{(1)} = K_s^{(2)} = K_s^{(3)} = K_s^{(4)} = K_s^{(5)} = K_s^{(6)} = 0$



(a)



(b)

Fig. 15. Seven-layer I-section beam problem: (a) Problem description and (b) Solid element model used to obtain reference solutions.

The beam is modeled using 20 continuum mechanics based beam elements ($21 \times 12 = 252$ DOFs), and the cross-section is discretized using fifteen 4-node cross-sectional elements. Reference solutions are obtained using 27-node solid elements (32,800 elements and 878,134 DOFs), as presented in Fig. 15(b). For comparison, a beam with rigid interlayer connections is considered, and this case is modeled as a single layer beam without interlayers.

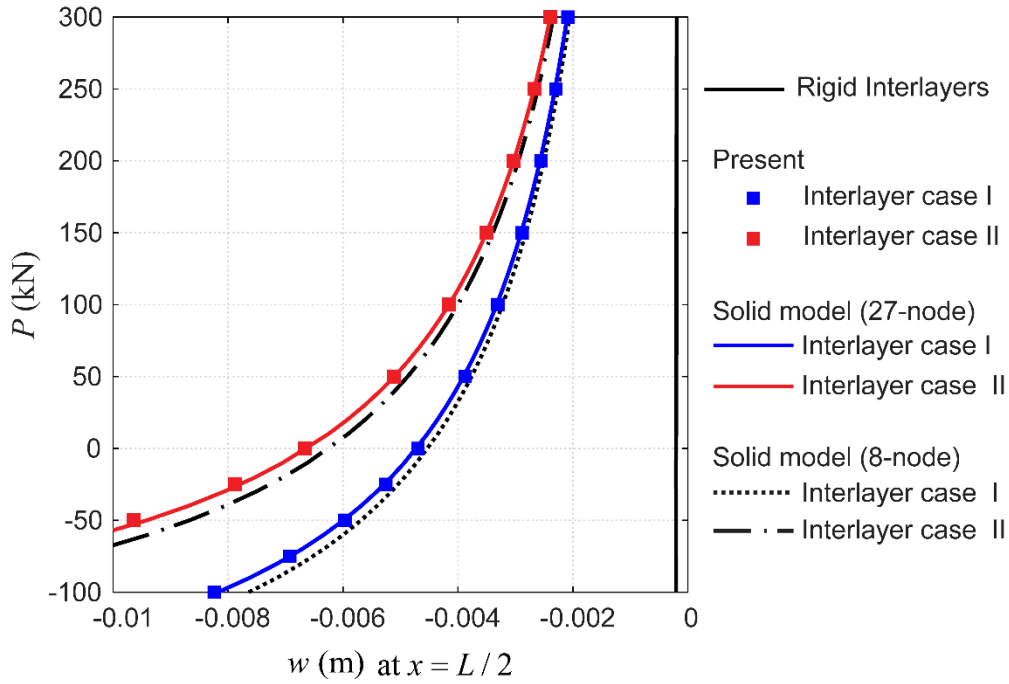


Fig. 16. Load-displacement curves for z -directional displacement w at the beam center according to tip axial load P varying from $P = -100$ kN to 300 kN with a constant transverse load $q_0 = 10$ kN/m in the seven-layer I-section beam problem.

Fig. 16 shows the load-displacement curves for the z -directional displacement w at the midpoint of the beam as the tip axial load P varies from compression ($P = -100$ kN) to tension ($P = 300$ kN) with a constant uniformly distributed load $q_0 = 10$ kN/m. The present beam model accurately predicts the nonlinear response due to the interaction between bending and compression. Because of the interaction between the transverse and axial loads, the deflection of the beam decreases when the tensile axial load P increases. Meanwhile, the deflection increases when the magnitude of the compressive axial load P increases. As expected, the presence of the deformable interlayers results in more flexible responses. The rigid interlayer case exhibits a

significantly stiffer behavior. The present beam model very well captures nonlinear responses of the multi-layered beam with deformable interlayers. Table 6 presents the displacement w at the midpoint of the beam when $P = 300$ kN and $P = -50$ kN.

Table 6. z -directional displacement w at the midspan of the beam under tensile axial load $P = 300$ kN and compressive axial load $P = -50$ kN with a uniformly distributed transverse load $q_0 = 10$ kN/m in the seven-layer I-section beam problem (unit: m).

		w at $x = L/2$	
		Interlayer Case I	Interlayer Case II
$P = 300$ kN	Present beam	-2.0883E-03	-2.3913E-03
	Solid element model	-2.0992E-03	-2.3933E-03
$P = -50$ kN	Present beam	-5.9667E-03	-9.6398E-03
	Solid element model	-5.9916E-03	-9.4123E-03

2.5.7 Cantilever four-layer box beam

A cantilever four-layer box beam is subjected to a tip shear load P as shown in Fig. 17(a). Unlike typical layered beam geometries studied before, Layers 1 and 4 are connected with two other layers positioned in parallel simultaneously. The four interlayers are located through two columns in pairs. All the layers of the beam are composed of a linear elastic material with Young's modulus $E = 100$ GPa.

Two interlayer cases with constant connection stiffnesses are tested:

- **Interlayer cases**

- Interlayer Case I: $K_s^{(1)} = K_s^{(4)} = \alpha K$, $K_s^{(2)} = K_s^{(3)} = K$
- Interlayer Case II: $K_s^{(2)} = K_s^{(2)} = K_s^{(3)} = K_s^{(4)} = (1 + \alpha)K / 2$,

where $K = 200$ MN/m² and α is a ratio varying from 0.05 to 1. In Interlayer Case I, the connection stiffnesses of Interlayers (1) and (4) vary depending on α , and those for Interlayers (2) and (3) are constant. In Interlayer Case II, the connection stiffnesses of all the interlayers are identical; it is the average of those in Interlayer Case I.

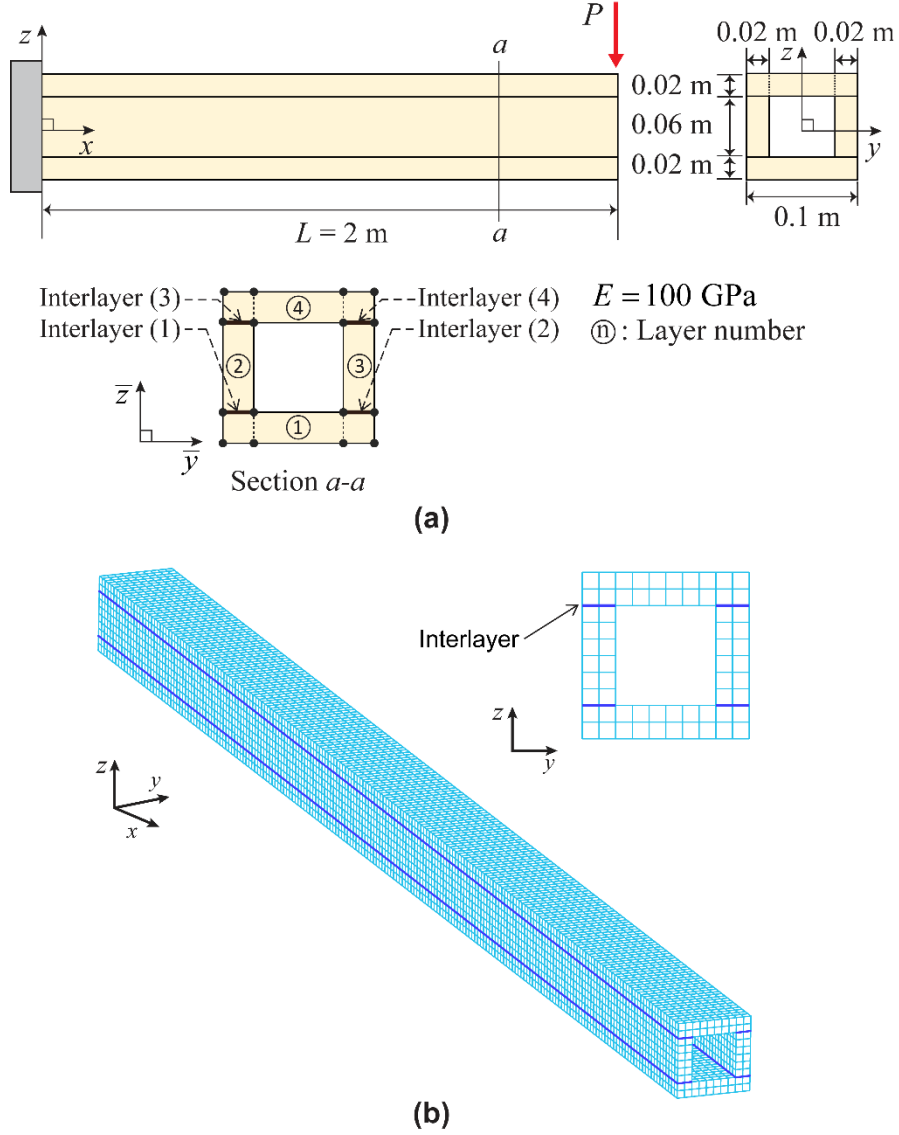


Fig. 17. Cantilever four-layer box beam problem: (a) Problem description and (b) Solid element model used to obtain reference solutions.

The beam is modeled using 10 continuum mechanics based beam elements ($11 \times 9 = 99$ DOFs), and the cross-section is discretized by eight 4-node cross-sectional elements. The beam model has four layer DOFs corresponding to the four layers. The slip displacements at the four interlayers at beam node k are evaluated as follows:

$$s_1^k = \varphi_k^{(2)} - \varphi_k^{(1)}, \quad s_2^k = \varphi_k^{(3)} - \varphi_k^{(1)}, \quad s_3^k = \varphi_k^{(4)} - \varphi_k^{(2)} \quad \text{and} \quad s_4^k = \varphi_k^{(4)} - \varphi_k^{(3)}. \quad (2.50)$$

The reference solutions are obtained from the solid model using 27-node solid elements (14,400 elements and 432,000 DOFs) as presented in Fig. 17(b). In this problem, linear behavior of the beam was considered.

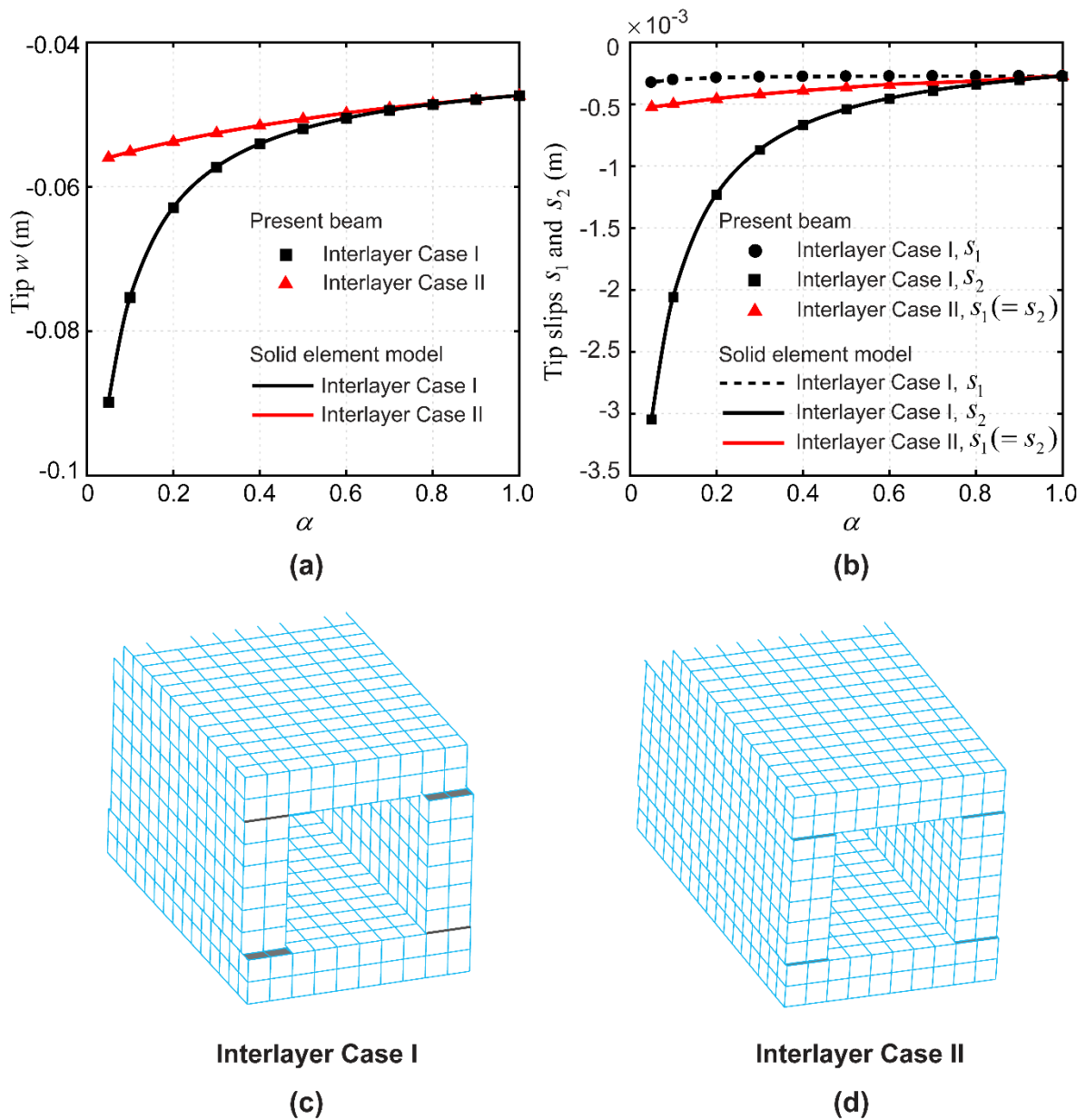


Fig. 18. Numerical results and deformed shapes for the cantilever four-layer box beam problem: (a) and (b) z -directional displacement w and slip displacements s_1 and s_2 at the free tip according to the interlayer connection stiffness ratio α , and (c) and (d) Deformed shapes at the free tip in Interlayer Cases I and II, respectively.

Figs. 18(a) and (b) show the z -directional displacement w and interlayer slips (s_1 and s_2) at the free tip for various values of α . For the lower values of α , the effect of the connection stiffness difference between the interlayers positioned in parallel increases, thus the differences in the results between Interlayer Case I and II increase. The results obtained from the proposed beam model exhibit excellent agreements with the reference

solutions in both Interlayer Cases I and II. Figs. 18(c) and (d) compare the deformed configurations at the free tip of the beam in Interlayer Cases I and II, respectively. Table 7 presents the displacement w and the interlayer slips (s_1 and s_2) at the free tip when $\alpha = 0.5$ and 0.05 in Interlayer Case I and II, respectively.

Table 7. z -directional displacement w and slip displacements s_1 and s_2 at the free tip in two interlayer cases ($\alpha = 0.5$ and 0.05) in the cantilever four-layer box beam problem (unit: m).

			Displacements at $x = L$		
			w	s_1	s_2
Interlayer Case I	$\alpha = 0.5$	Solid element model	-5.1965E-02	-5.3857E-04	-2.7535E-04
		Present beam	-5.1994E-02	-5.4229E-04	-2.7825E-04
	$\alpha = 0.05$	Solid element model	-8.9762E-02	-3.0361E-03	-3.2189E-04
		Present beam	-8.9869E-02	-3.0486E-03	-3.2805E-04
Interlayer Case II	$\alpha = 0.5$	Solid element model	-5.0597E-02	-3.6410E-04	-3.6410E-04
		Present beam	-5.0636E-02	-3.6715E-04	-3.6715E-04
	$\alpha = 0.05$	Solid element model	-5.5935E-02	-5.1893E-04	-5.1893E-04
		Present beam	-5.5971E-02	-5.2278E-04	-5.2278E-04

2.5.8 Comparison with experimental test1: Nailed two-layer wood beam

In order to validate the performance of the present beam finite element in practical problems, a comparison between the present beam model and the experimental results by Wheat and Calixto in [8] was made. In the experimental test in Ref [8], a two-layer beam composed of solid wood (Layer 1) nailed to plywood sheathing (Layer 2) is considered as shown in Fig. 19(a). An eccentric axial load P is applied on the cross-section of the solid wood at the end of the beam ($x = L$) where the eccentricity e is measured from the center line of the solid wood.

In the experimental test in Ref [8], the material property of the beam and the load-slip relation at an interlayer were determined through a series of experimental test. The elastic modulus of the solid wood and plywood sheathing are calculated from simple span beam tests. The interlayer is connected with connectors (6d

common nails) in two rows, and the constitutive relationship between magnitude of shear force \bar{F}_s (N) and magnitude of slip δ (m) in the single connector is determined using empirically derived Foshi-Bonac equation [34] shown in Fig. 19(b). The slip force per unit length F_s (N/m) at the interlayer is calculated as:

$$F_s = \frac{n}{s} \bar{F}_s \quad (2.51)$$

where n is the number of connectors per row and s is the spacing between the rows ($n = 2$ and $s = 0.178$ m). For a more detailed experimental procedure, see [8].

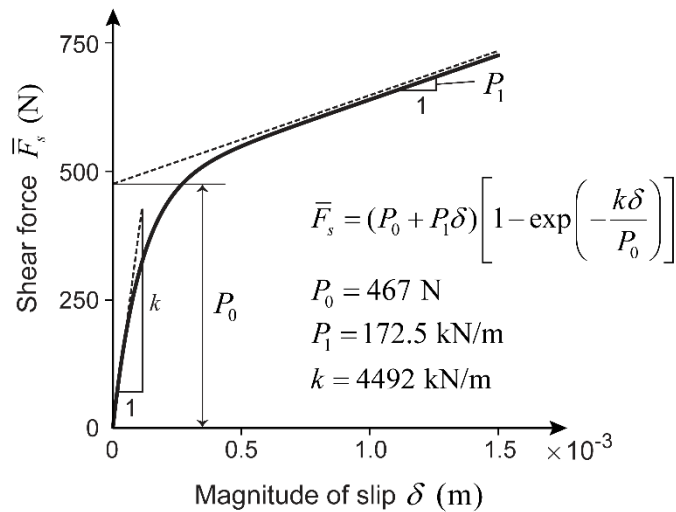
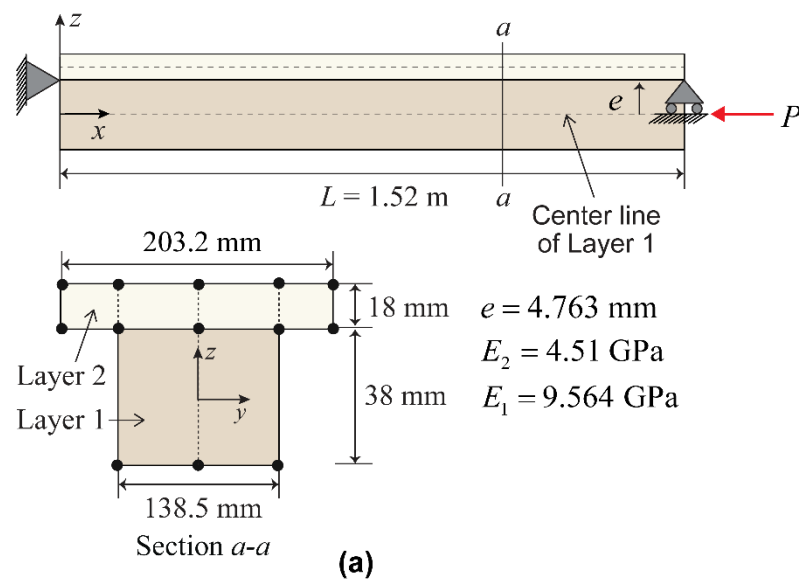


Fig. 19. Nailed two-layer wood beam problem: (a) Problem description and (b) Foshi-Bonac load-slip curve and material parameters used.

In the present beam model, the beam is modeled using 20 continuum mechanics based beam elements ($21 \times 7 = 147$ DOFs) and the cross-section is discretized using six 4-node cross-sectional elements. Load vector for the beam model is calculated as similar way in section 2.5.4. Note that the experimental specimen used in [8] was composed such that plywood sheathing is 25.4 mm shorter than the solid wood to ensure axial and rotational movement at the end of the beam, however, this slight length difference between the Layer 1 and 2 is neglected in the present beam model.

Fig. 20 shows the load-displacement curves for the z -directional displacement w at the midspan of the beam compared with the experimental results in [8]. Good agreement is obtained in an overall range even where the deflection increases rapidly according to the small increase in axial load P . Table 8 presents the z -directional displacement w at the midspan of the beam for three load levels ($P = 10$ kN, 20 kN, and 30 kN).

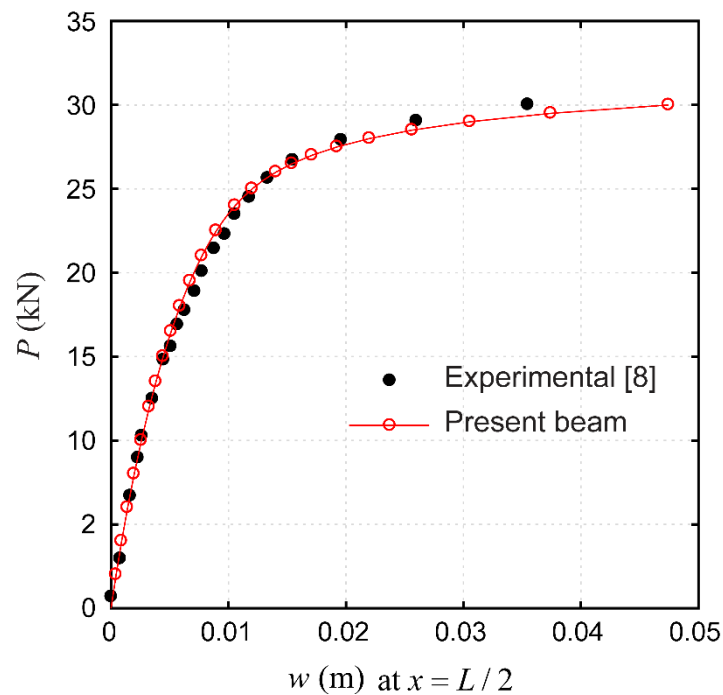


Fig. 20. Load-displacement curves for the deflection w at the midspan of the beam according to the eccentric axial load P in the nailed two-layer wood beam problem.

Table 8. z -directional displacement w at the midpoint of the beam for three load levels ($P = 10$ kN, 20 kN, and 30 kN) in the nailed two-layer wood beam problem (unit: m).

	w at $x = L/2$		
	$P = 10$ kN	$P = 20$ kN	$P = 30$ kN
Present beam	2.5872E-03	7.0583E-03	4.7478E-02

2.5.9 Comparison with experimental test2: Mode II delamination test of ENF specimen

The present beam model is compared with the experimental data and the numerical simulation in pure Mode II delamination test of ENF specimen conducted by Camanho and Dávila [36] and Turon et al. [37]. In the experimental tests, end notched flexure (ENF) test was performed to investigate onset and propagation of delamination under pure Mode II loading condition. The ENF specimen is simply supported, and pure mode II loading condition is applied by concentrated load P at the midspan of the specimen.

In the experimental test, the ENF specimen is made of unidirectional AS4/PEEK carbon-fiber reinforced composite of 102-mm-long, 25.4 mm-wide, two 1.56-mm-thick arms with an initial delamination length $a_0 = 39.3$ mm. For the numerical simulation, the arms of the specimen are modeled by solid elements, and the cohesive interface is modeled by 8-node decohesion elements. The initial delamination is modeled by open decohesion elements along the length. Under a single Mode II loading condition, the decohesion element uses a bi-linear constitutive relationship that relates tractions τ to the relative displacements δ as shown in Fig. 21(b) where K is the penalty stiffness, τ^0 is the interlaminar shear strength for Mode II, G_{IIc} is pure Mode II interlaminar fracture toughness which is the area under $\tau - \delta$ curve, and d is a scalar damage variable ($K = 10^6$ N/mm³, $\tau^0 = 100$ MPa, and $G_{IIc} = 1.719$ kJ/m²).

In the present beam model, the ENF specimen is modeled using 102 continuum mechanics based beam elements ($102 \times 7 = 7014$ DOFs), and the cross-section is discretized using two 16-node cross-sectional elements as shown in Fig. 21(a). The penalty stiffness K is used as the initial interlayer connection stiffness for the linear load-slip behavior at the cohesive interface range. After the shear traction τ reaches τ^0 , the interlayer stiffnesses are set to be gradually reduced to zero to represent the softening behavior. The initial delamination

range is modeled by zero interlayer connection stiffness. Since only pure Mode II delamination occurs in ENF test, the material property is modeled as isotropic elastic material with $E = E_{11}$ and $G = G_{12} = G_{13}$.

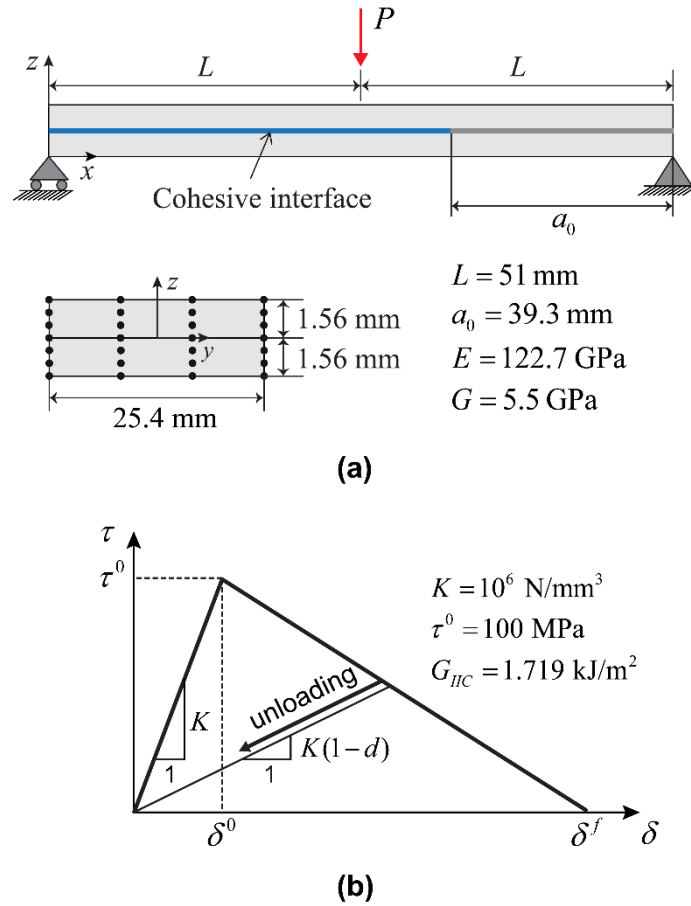


Fig. 21. Mode II delamination test of ENF specimen: (a) Problem description and (b) Bi-linear constitutive relationship used in cohesive interface.

Fig. 22 shows the load-displacement curves for the z -directional displacement w at the midspan of the ENF specimen model. The results obtained from the present beam model are compared with the ones obtained in experimental test and numerical simulation in [37]. Before the onset of damage initiation, the present beam model shows completely identical behavior with the numerical result in [37]. After the damage initiation, the response of present beam model is more similar to the experimental data than numerical simulation in [37]. Table 9 compares the maximum loads P_{\max} obtained from the experimental test, numerical simulation in [37], and the present beam model.

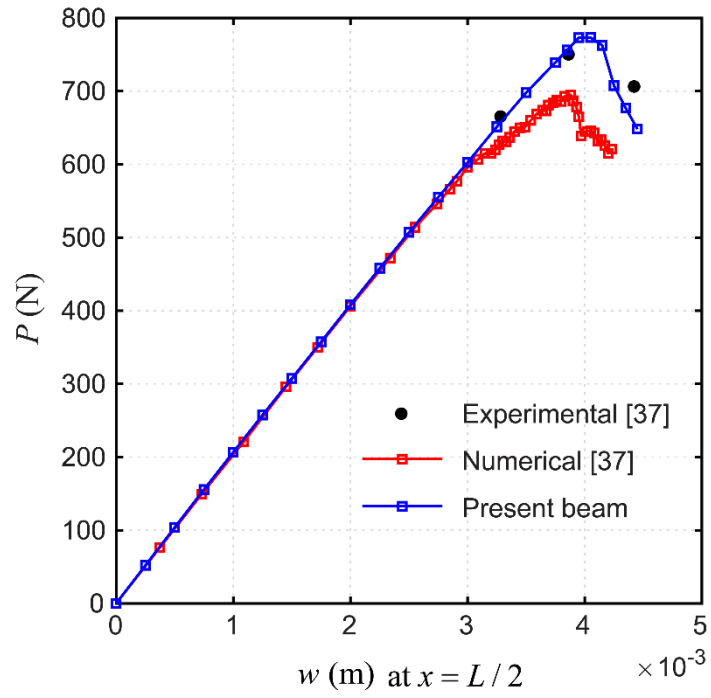


Fig. 22. Load-displacement curves for the z -directional displacement w at the midspan of the beam according to the concentrated load P in the Mode II delamination test of ENF specimen problem.

Table 9. Maximum loads P_{\max} in the Mode II delamination test of ENF specimen problem (unit: N).

	Experimental [37]	Numerical [37]	Present beam
Maximum loads P_{\max}	748.4	697.1	773.3

2.6 Concluding remarks

3.6.1 Summary

In Chapter 2, continuum mechanics based beam elements for linear and nonlinear analyses of multi-layered composite beams with interlayer slips were presented, and their performance was demonstrated through several representative numerical examples. The proposed beam finite element exhibits excellent predictive and modeling capabilities to deal with various complex multi-layered beam problems. Complicated layered beam geometries including arbitrary numbers of layers and interlayers, varying and composite cross-sections, and eccentricities can be easily modeled, and their geometric and material nonlinear behaviors as well as nonlinear load-slip relations at interlayers are accurately predicted.

The main objective of the study presented Chapter 2 is aimed to develop new efficient and accurate beam finite element for linear and nonlinear analyses of multi-layered composite beams including interlayer slips. Most of the previous studies focused largely on simple two- and three-layer beams, and therefore nonlinear behaviors of general multi-layered beams are very rarely discussed. Most notably, the proposed new beam finite element can model the complicated layered beam geometries of arbitrarily positioned multi-layered beams as a single beam model without additional interface elements or constraints. As in most previous studies, interlayer slips only in the longitudinal direction of the beam was taken into account the slip kinematics. However, it is necessary to consider lateral slip and uplift behaviors at the interlayers for the complete 3D simulation of layered beams, especially when torsional loading is dominant or delamination occurs. To achieve this, much complicated kinematics including cross-sectional distortion, warping, and their interactions with bending, stretching, twisting, and shearing should be studied.

3.6.2 Future works

In general, the layered beam structures consist of multiple layers, and these layers are connected by interlayer connections, such as mechanical connectors or adhesive connection. As the interlayers of layered beam structures are incompletely connected, flexible behavior occurs in the interlayers and these interlayers are the most vulnerable in many cases. Therefore, the behavior of the layered beam structures is significantly affected by not only the characteristics of the layers that constitute the body of the beam but also by the characteristics of interlayer

connections and the behavior at interlayers. Thus, it is necessary to consider lateral slips uplift behaviors at the interlayers in addition to the interlayer slips in longitudinal direction of the beam for the complete 3D simulation of the layered beams, especially when torsional loading is dominant or delamination occurs.

However, there were only few studies of lateral slip behaviors, which were focusing mainly on experimental tests of two-layer beams. It is known that there is no mixed-mode test method available incorporating Mode III loading until now, and even the interlayer behaviors under pure Mode III loading conditions are very rarely discussed so far. Incorporating lateral slips and uplifts behaviors in general 3D behaviors is not simple works within beam theories. Because, to do this, not only the interlayer behaviors themselves, but also relevant distorted mode on the cross-section of the layered beam should also be taken account into the kinematics. This distorted mode is closely coupled with the warped shape of individual layer and whole layered beam geometries as well as layer-wise bending, and significantly affected by the interlayer connection properties and loading conditions. Moreover, this distorted mode become even more complex as the number of layer increases. (for an example, there is only a single lateral mode in a two-layer beam, but there could be three different lateral modes in a three-layer beam depending on the layer-wise loading conditions.) In fact, slips in longitudinal and lateral direction together with uplift at interlayers is a part of the more general damage mechanics theory, in which each of them belongs to Mode II, Mode III and Mode I failures, respectively.

There are three failure modes that may occur in interlayers: Mode I referred to as the normal mode or opening mode; Mode II, which is the shear mode in the in-plane direction; and Mode III, which is the out-of-plane shear mode. For beam structures, Mode II occurs most frequently among the three failure modes. In a practical perspective, a beam is a structural member that primarily resists laterally applied loads, which are forces or moments applied perpendicular to the longitudinal axis of the beam. The case in which the axial load is additionally considered is often referred to as beam-columns separately, but beams and beam-columns are generally referred to as beams.

Under the geometrical and load conditions of these general beam members, the interlayer behavior is mainly affected by interlayer slips in longitudinal direction (Mode II). For these reasons, most of previous researches regarding the behaviors of the layered beam have been focused on interlayer slips in longitudinal direction except some special cases. In cases where torsional behavior is dominant in layered beams or delamination occurs, however, the behavior of Modes I and II in interlayer regions becomes more important than that of in Mode II

direction. Therefore, to more accurately predict the 3D behavior of layered beams under more general conditions, additional follow-up research is required to expand the current model so that the interlayer behaviors in Mode I and II directions as well as the interlayer slips can be incorporated to the beam kinematics.

Chapter 3. Continuum mechanics based beam elements for multi-layered helically stranded cable structures

Helically stranded cable structures, which are commonly known as wire ropes or cables, are defined as an assemblage of multiple wires twisted into a helix geometry. These cable structures generally have multiple layers that consists of helical wires or strands, and composed of various materials, such as metal, plastic, rubber, and composite materials depending on the application and design conditions. Cable structures have been used in various fields because they have flexible structural characteristics due to relatively low bending rigidity while withstanding large axial loads. For example, they have been used in various engineering fields, such as simple copper wires and power cables that are used in everyday life, cables for railways, ships, and automobiles, optical cables, submarine cables, and so on.

In general, the cable structures consist of multiple layers of helical wires flexibly connected, there exist flexible behavior between the wires in addition to the global behaviors that occurs uniformly in the entire cable. The behavior of the cable structures is significantly affected by the connections between the wires in a cable because the degree of inter-wire connections determines the flexible characteristics of the cable, and has a major influence on the entire behavior of the cable. Therefore, in order to describe the kinematics cable structures appropriately, it is necessary to closely consider not only the global behavior of the entire cable structure but also the individual behaviors of the wires including inter-wire slip and wire local rotation.

In the mechanical behaviors of the cables, the axial and torsional deformation modes are closely coupled due to their structural characteristics. The appropriate torque balance condition is very important in the design of cables, because the cables are vulnerable to torsional loads that may loosen the helical structure. The design procedure to full the torque balanced cables generally requires many experiments and numerical verifications. Moreover, the cable structures are often subjected to large deformation and rotation under various loading conditions, such as tension, bending, and torsion, and failure or damage inside the cables may incur massive expenses in many cases. Therefore, accurate prediction of the mechanical behavior of the cables also considering the geometrical and material nonlinearities within a short period of time is a crucial issue for the precise design and accurate analysis of the cables.

Obviously, well-prepared experimental tests perform an important role in obtaining reliable results of the behaviors of the cables, but typically, the laboratory experiments are difficult to conduct, and take much time and expense in many cases. There have been very few experimental tests concerning the mechanical behavior of the cables reported in the literature [39-42], which considered simple straight strand cables under axial loading cases. According to the growing demand in predicting the cable behavior, many studies regarding analytical models [43–59] have been carried out for widening the understanding of the cable behaviors. Although these analytical models give acceptable results, most of their validity are based on the linear elastic assumptions and are also limited to simple axial or bending load cases.

With the advancement of the finite element (FE) method, many FE model has been developed and broadly used for design and analysis of cable structures. Numerous studies have been conducted for the numerical models to analyze the behavior of the cable structures [60–70]. The full solid FE model has been successfully used to predict complicated behaviors of the cable structures including the detailed contact deformation between the wires and various failures inside the cable. However, it generally requires complex modeling procedure and considerable computational cost even in simple analysis models. In the case of the simplified 2D cross-sectional axisymmetric solid model, there are limitations in considering deformations and loading conditions varying in the longitudinal direction of the cable. The approximated models using equivalent stiffness are also used for a simplicity, but it cannot properly deal with the complex cross-sectional geometries and individual behavior of the wires including inter-wire slip. Layer-wise beam models, which models the wires in a cable as individual beam models, give acceptable results in many cases; however, it is necessary to implement constraints for contact and penetration conditions between the wires and cores, and the number of constraints increases substantially as the numbers of layers and wires increase.

The main objective the works presented in this chapter is to propose a new continuum mechanics based beam finite element for efficient analysis of multi-layered helically stranded cable structures. The main feature of the proposed beam finite element is an advanced modeling capability that originates from the general 3D geometry and displacement interpolations of the continuum mechanics based beams. The continuum mechanics based beam formulation enables much simpler and more efficient modeling procedure using relatively small number of the degree of freedom (DOF) because the entire geometry of the helically stranded cable is modeled as a single beam model instead of modeling the individual sub-components. Thus, it is possible to deal with the behavior of the

entire cable structure regardless of the numbers of layers and sub-components that constitute the cable

In the following sections, nonlinear kinematics of multi-layered helically stranded cable structures allowing inter-wire slips together with individual wire rotations and finite element formulation are presented. Geometry and displacement interpolations for strand cables are described in detail, and linearized incremental equilibrium equations are derived based on the total Lagrangian formulation. Finally, the finite element discretization procedure is presented. The performance and predictive capability of the proposed beam finite elements are demonstrated through several representative numerical examples.

3.1 Basic assumptions and local coordinate systems of helically stranded cable structures

Cable structures are used in various geometries depending on the practical situations and design conditions. As the most basic cable structure, a structure in which a single wire acting as core is surrounded by a layer of wires is referred to as a strand. This strand is used as the basic structure and expanded to various types of cable structures. Fig. 23 shows a strand cable structure composed of three-layer and 17-wire as an example. In this thesis, the proposed beam finite element deals with the behaviors of the multi-layered stranded cable structures focusing on the most common condition that the entire cable structure including each wire that constitutes the cable behaves maintaining their helical geometries. In other words, the kinematics of strand cable structures that behave integrally with the entire structure of the cable is considered without considering extreme failure modes, such as the separation of a particular wire and the failure of the helical structure of the entire cable.

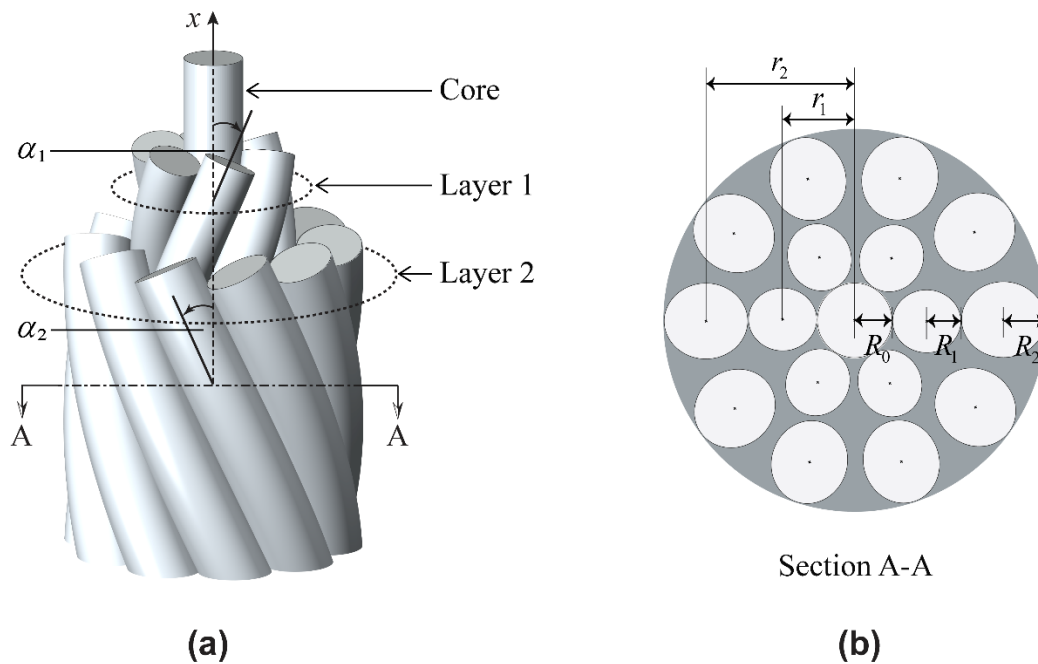


Fig. 23. Geometry of helically stranded cable: (a) A three-layer strand cable consists of and 17-wire where α_n is lay angle of layer n , (b) cross-section of the three-layer strand cable where r_n and R_n are winding radius and radius of wires in layer n respectively.

Expressing these basic conditions mathematically, the centers of each wire that constitutes a cable are located on the surface of the flexible cylinder that has the winding radius r_n , which denotes the rotating radius of the wires in layer n , as a radius, and the helix line that represents the center line of these wires follows the behavior of the flexible cylinder, which can be said to represent the structure of the entire cable (Fig. 24). As the wires that constitute the cable are not connected through complete rigid connection, the individual local behavior of the wires occurs in addition to the global behavior of the entire cable structure. Therefore, inter-wire slips in the longitudinal direction of the cable and the individual wire local rotations occur due to the local behavior of the wires. In order to represent the kinematics of cable structures properly, it is necessary to consider the global behavior of the entire cable structure as well as the individual behavior of the wires including the inter-wire slips and wire local rotations altogether.

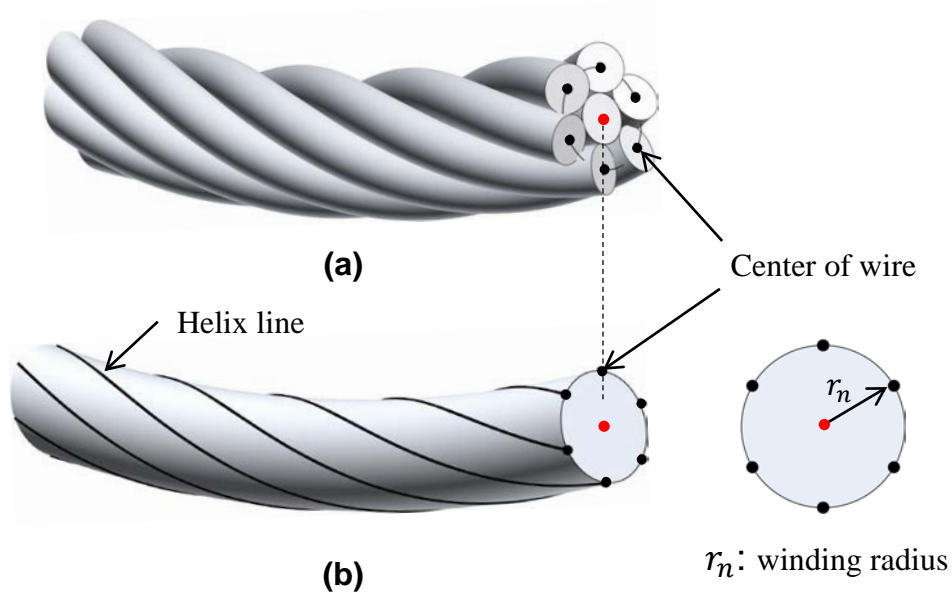


Fig. 24. (a) A 7-wire helically stranded cable structure and (b) Flexible cylinder whose radius is r_n , which is winding radius of the outer wire of the cable in (a).

The following three coordinate frames are used to represent the kinematics of the helically stranded cable structures based on continuum mechanics based formulation (Fig. 25): Coordinate frame $\{0\}$, which is the fixed coordinate system with the basis $\{\mathbf{x}\} = \{\mathbf{e}_1 \quad \mathbf{e}_2 \quad \mathbf{e}_3\}$; coordinate frame $\{1\}$ (marked in blue), which is the cable local coordinate system with the basis $\{{}^t\mathbf{V}_x^k\} = \{{}^t\mathbf{V}_x^k \quad {}^t\mathbf{V}_y^k \quad {}^t\mathbf{V}_z^k\}$ whose origin is located on the center of cable at the beam node k ; coordinate frame $\{2\}$ (marked in red), which is the wire local coordinate system with the basis $\{{}^t\mathbf{n}^{k(m)(n)}\} = \{{}^t\mathbf{n}_x^{k(m)(n)} \quad {}^t\mathbf{n}_y^{k(m)(n)} \quad {}^t\mathbf{n}_z^{k(m)(n)}\}$ whose origin is located on the center of the wire m at the beam node k . The transformation between the coordinate frame from $\{a\}$ to $\{b\}$ is represented through the transformation operator $[{}^a\mathbf{T}_b]$.

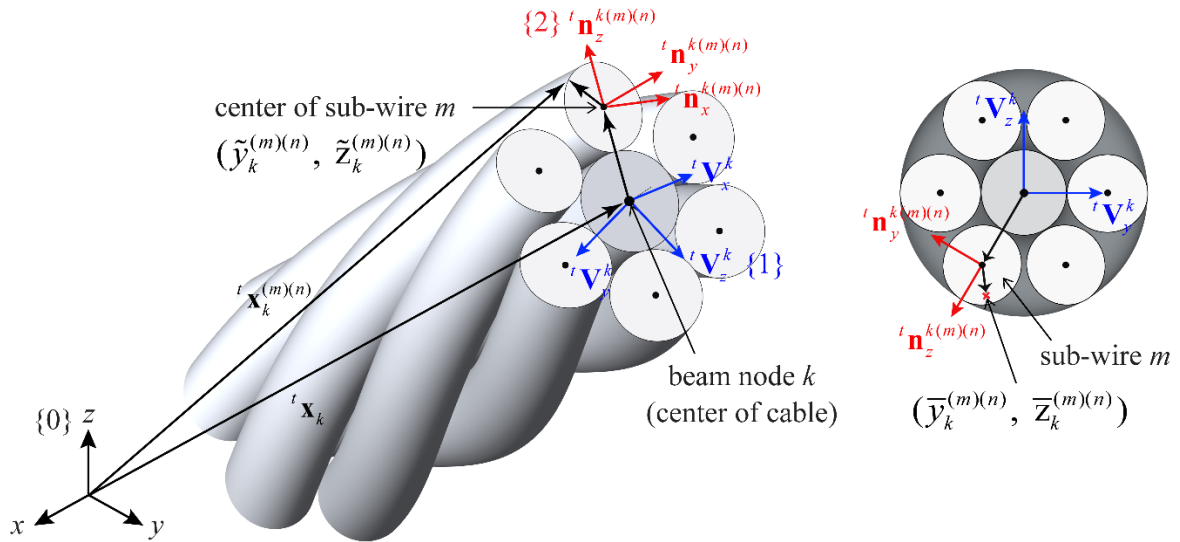


Fig. 25. Concept of the multi-director continuum beam finite element for helically stranded cable structures where three coordinate system $\{0\}$, $\{1\}$ and $\{2\}$ are employed to represent the geometry of the strand cable.

3.2 Nonlinear kinematics of helically stranded cable structures

In this section, the nonlinear kinematics of the continuum mechanics based beam that represents the helically stranded cable structures is presented. The geometry interpolation of the continuum mechanics based beam element is directly degenerated from an assemblage of 3D solid finite elements that models the wires in the cable structures. Each wire belonging to the layer in the cable structures here is named as a sub-wire (Fig. 25). In the following formulations, a superscript t denotes the load levels and incremental variables in the static nonlinear analyses rather than the actual time as in dynamic analyses.

The geometry interpolation of sub-wire m belonging to layer n of the cable is given by

$${}^t \mathbf{x}^{(m)(n)} = \sum_i h_i(r, s, t) {}^t \mathbf{x}_i^{(m)(n)} \quad (3.1)$$

in which $h_i(r, s, t)$ denotes the general 3-D interpolation function defined in natural coordinate system (r, s, t) and ${}^t \mathbf{x}_i^{(m)(n)}$ is nodal position vector of node i in the sub-wire m . Assuming the cross-sections originally normal to the helix line of each wire remain plane and undistorted during deformations and the nodes are placed on the cross-sectional plane of the wire, the 3-D interpolation function in Eq. (3.1) can be replaced by the multiplication of 1-D and 2-D interpolation functions,

$${}^t \mathbf{x}^{(m)(n)} = \sum_{k=1}^q \sum_{j=1}^p h_k(r) h_j(s, t) {}^t \mathbf{x}_k^{j(m)(n)} \quad (3.2)$$

where ${}^t \mathbf{x}_k^{j(m)(n)}$ indicates the nodal position vector of the cross-sectional node j on the cross-sectional plane k of the sub-wire m of the layer n , $h_k(r)$ and $h_j(s, t)$ are the 1-D and 2-D shape functions, and p and q are determined depending on the number of cross-sectional nodes and cross-sectional plane used.

Considering the sub-wire m belong to layer n , the cross-sectional position at the beam node k in the configuration at time t is represented by a sequence of multiplication of matrices, which consists of combined operations of rotation and translation with respect to the successive current coordinate frames,

$$\begin{bmatrix} {}^t \mathbf{x}_k^{(m)(n)} \\ 1 \end{bmatrix} = \begin{bmatrix} [\mathbf{I}] & {}^t \mathbf{x}_k \\ 0 & 1 \end{bmatrix} \begin{bmatrix} {}^t [{}^0 \mathbf{T}_{1(k)}] & \mathbf{0} \\ 0 & 1 \end{bmatrix} \begin{bmatrix} [\mathbf{I}] & \tilde{\mathbf{x}}_k^{(m)(n)} \\ 0 & 1 \end{bmatrix} \begin{bmatrix} {}^t [{}^{1(k)} \mathbf{T}_{2(k)(m)}] & \mathbf{0} \\ 0 & 1 \end{bmatrix} \begin{bmatrix} [\mathbf{I}] & \bar{\mathbf{x}}_k^{(m)(n)} \\ 0 & 1 \end{bmatrix} \begin{bmatrix} {}^t \varphi_k^{(m)(n)} & {}^t \bar{\mathbf{V}}_s^k \\ 1 & \end{bmatrix} \quad (3.3)$$

with
$${}^t \mathbf{X}_k^{(m)(n)} = \begin{bmatrix} {}^t x_k & {}^t y_k & {}^t z_k \end{bmatrix}^T, \quad (3.4)$$

$$\tilde{\mathbf{x}}_k^{(m)(n)} = \begin{bmatrix} \tilde{x}_k^{(m)(n)} & \tilde{y}_k^{(m)(n)} & \tilde{z}_k^{(m)(n)} \end{bmatrix}^T, \quad (3.5)$$

$$\bar{\mathbf{x}}_k^{(m)(n)} = \begin{bmatrix} \bar{x}_k^{(m)(n)} & \bar{y}_k^{(m)(n)} & \bar{z}_k^{(m)(n)} \end{bmatrix}^T, \quad (3.6)$$

where ${}^t \begin{bmatrix} a & \mathbf{T}_b \end{bmatrix}$ is the coordinate transform matrix from coordinates $\{a\}$ to $\{b\}$, ${}^t \varphi_k^{(m)(n)}$ is the wire DOF given to each sub-wire m belong to layer n at beam node k , and ${}^t \tilde{\mathbf{V}}_s^k$ is the slip director vector represented on the wire local coordinate system $\{2\}$, which indicates the longitudinal direction of the cable structure in the configuration at time t . Note that $\tilde{x}_k^{(m)(n)}$ and $\bar{x}_k^{(m)(n)}$ in Eqs (3.5) and (3.6) are zero.

In Eq. (3.3), each matrix form is the 4×4 matrix operator called homogeneous transform, which denotes mapping from one frame to another. The matrix operator is constructed by 3×3 rotation matrix and 3×1 position vector, and a row $[0 \ 0 \ 0 \ 1]$ is added as the last row of the matrix operator. For more detailed descriptions, see Refs [72-74].

Substituting ${}^t \mathbf{X}_k^{(m)(n)}$ into Eq. (3.2), the geometry interpolation of the sub-wire m belong to layer n in the configuration at time t is obtained as follows.

$$\begin{aligned} {}^t \mathbf{x}^{(m)(n)} &= \sum_{k=1}^q h_k(r) ({}^t \mathbf{X}_k^{(m)(n)}) \\ &= \sum_{k=1}^q h_k(r) \left({}^t \mathbf{x}_k + {}^t \begin{bmatrix} 0 & \mathbf{T}_{1(k)} \end{bmatrix} \tilde{\mathbf{x}}_k^{(m)(n)} + {}^t \begin{bmatrix} 0 & \mathbf{T}_{1(k)} \end{bmatrix} {}^t \begin{bmatrix} 1 & \mathbf{T}_{2(k)(m)} \end{bmatrix} \bar{\mathbf{x}}_k^{(m)(n)} + {}^t \varphi_k^{(m)(n)} {}^t \mathbf{V}_s^k \right) \end{aligned} \quad (3.7)$$

An significant feature of the continuum mechanics based beam formulation for helically stranded cable structures is that the cross-sectional geometry of each wire is interpolated using cross-sectional nodes and elements defined on the wire local Cartesian coordinate system at beam node k as shown in Fig. 26. For a p -node cross-sectional element m corresponding to sub-wire m of layer n , the material position in the cross-sectional area ($\bar{y}_k^{(m)(n)}$ and $\bar{z}_k^{(m)(n)}$) is interpolated as

$$\bar{y}_k^{(m)(n)} = \sum_{j=1}^p h_j(s, t) \bar{y}_k^{j(m)(n)}, \quad \bar{z}_k^{(m)(n)} = \sum_{j=1}^p h_j(s, t) \bar{z}_k^{j(m)(n)} \quad (3.8)$$

where $h_j(s, t)$ is the 2D shape function corresponding to cross-sectional node j and $\bar{y}_k^{j(m)(n)}$ and $\bar{z}_k^{j(m)(n)}$ are the coordinates of cross-sectional node j in the wire local Cartesian coordinate system defined on the center of wire m at the beam node k .

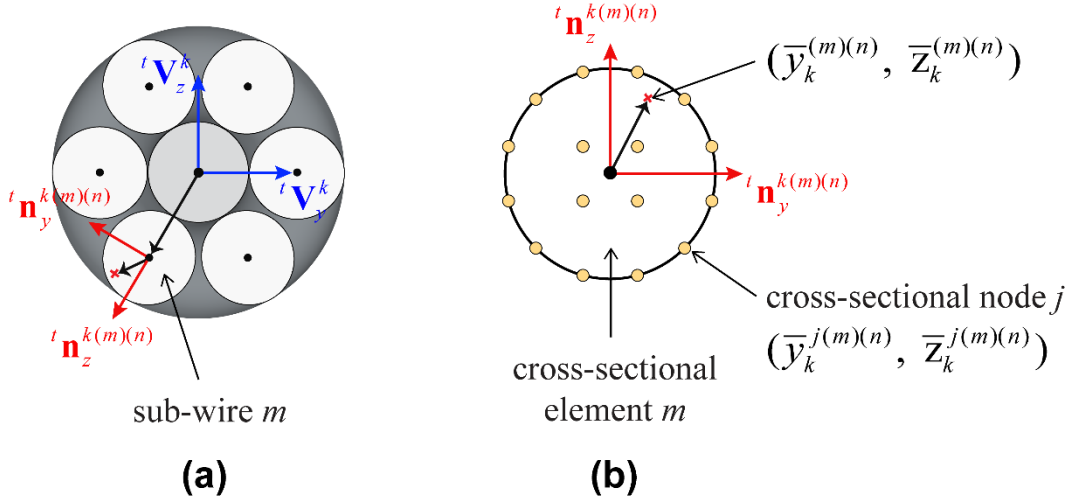


Fig. 26. Cross-sectional modeling of helically stranded cable using cross-sectional nodes and elements: (a) Cross-sectional geometry of a 7-wire strand cable, and (b) Cross-section of sub-wire m at beam node k modeled by p -node cross-sectional elements, where $p = 16$.

In a similar manner, the cross-sectional position of sub-wire m belong to layer n at the beam node k in the deformed configuration at time $t + \Delta t$ is obtained,

$$\begin{aligned} \begin{bmatrix} t+\Delta t \mathbf{x}_k^{(m)(n)} \\ 1 \end{bmatrix} &= \left(\begin{bmatrix} [\mathbf{I}] & t+\Delta t \mathbf{x}_k \\ \mathbf{0} & 1 \end{bmatrix} \begin{bmatrix} {}^t [{}^0 \mathbf{T}_{1(k)}] & \mathbf{0} \\ \mathbf{0} & 1 \end{bmatrix} \begin{bmatrix} \mathbf{R}({}_0 \tilde{\boldsymbol{\theta}}_c^k) & \mathbf{0} \\ \mathbf{0} & 1 \end{bmatrix} \begin{bmatrix} [\mathbf{I}] & \tilde{\mathbf{x}}_k^{(m)(n)} \\ \mathbf{0} & 1 \end{bmatrix} \begin{bmatrix} {}^t [{}^{1(k)} \mathbf{T}_{2(k)(m)}] & \mathbf{0} \\ \mathbf{0} & 1 \end{bmatrix} \right) \\ &\cdot \left(\begin{bmatrix} \mathbf{R}({}_0 \bar{\boldsymbol{\theta}}_w^{k(n)}) & \mathbf{0} \\ \mathbf{0} & 1 \end{bmatrix} \begin{bmatrix} [\mathbf{I}] & \bar{\mathbf{x}}_k^{(m)(n)} \\ \mathbf{0} & 1 \end{bmatrix} \begin{bmatrix} t+\Delta t \phi_k^{(m)(n)} & t+\Delta t \bar{\mathbf{v}}_s^k \\ & 1 \end{bmatrix} \right). \end{aligned} \quad (3.9)$$

where $\mathbf{R}({}_0 \boldsymbol{\theta}^k)$ is the finite rotation tensor, which is represented by the skew-symmetric matrix operator $\hat{\mathbf{R}}({}_0 \boldsymbol{\theta}^k)$ with the incremental Eulerian angle vector ${}_0 \boldsymbol{\theta}^k$ that consists of incremental Eulerian angles ${}_0 \theta_x^k$, ${}_0 \theta_y^k$, and ${}_0 \theta_z^k$ from time t to $t + \Delta t$ as the following equations

$$\mathbf{R}({}_0 \boldsymbol{\theta}^k) = \mathbf{I} + \frac{\sin {}_0 \theta^k}{{}_0 \theta^k} \hat{\mathbf{R}}({}_0 \boldsymbol{\theta}^k) + \frac{1 - \cos {}_0 \theta^k}{{}_0 \theta^k)^2} \hat{\mathbf{R}}({}_0 \boldsymbol{\theta}^k)^2, \quad (3.10)$$

$${}^0\boldsymbol{\theta}^k = \begin{bmatrix} {}^0\theta_x^k & {}^0\theta_y^k & {}^0\theta_z^k \end{bmatrix}^T, \quad {}_0\theta^k = \sqrt{({}^0\theta_x^k)^2 + ({}^0\theta_y^k)^2 + ({}^0\theta_z^k)^2} \quad (3.11)$$

$$\hat{\mathbf{R}}({}_0\boldsymbol{\theta}^k) = \begin{bmatrix} 0 & -{}_0\theta_z^k & {}^0\theta_y^k \\ {}^0\theta_z^k & 0 & -{}_0\theta_x^k \\ -{}_0\theta_y^k & {}^0\theta_x^k & 0 \end{bmatrix} \quad (3.12)$$

In Eq. (3.9), two rotation variables were used. First, the cable rotation variable ${}_0\tilde{\boldsymbol{\theta}}_c^k$ for representing the rotation behavior that uniformly occurs in the entire cable structure, and wire rotation variable ${}_0\bar{\boldsymbol{\theta}}_w^{k(n)}$ for representing the rotation behavior that individually occurs in each wire. The cable local rotation ${}_0\tilde{\boldsymbol{\theta}}_c^k$ is defined based on the cable local coordinate system at beam node k and rotates the coordinate frame $\{1\}$. The wire local rotation ${}_0\bar{\boldsymbol{\theta}}_w^{k(n)}$ is defined based on the wire local coordinate system at beam node k and rotates the coordinate frame $\{2\}$ in each wire.

Substituting ${}^t\mathbf{x}_k^{(m)(n)}$ into Eq. (3.2), the geometry interpolation of the sub-wire m belong to layer n in the deformed configuration at time $t + \Delta t$ is obtained as follows.

$$\begin{aligned} {}^{t+\Delta t}\mathbf{x}^{(m)(n)} &= \sum_{k=1}^q h_k(r) ({}^{t+\Delta t}\mathbf{x}_k^{(m)(n)}) \\ &= \sum_{k=1}^q h_k(r) \left({}^{t+\Delta t}\mathbf{x}_k + {}^t \begin{bmatrix} 0 & \mathbf{T}_{1(k)} \end{bmatrix} \mathbf{R}({}_0\tilde{\boldsymbol{\theta}}_c^k) \tilde{\mathbf{x}}_k^{(m)(n)} + {}^t \begin{bmatrix} 0 & \mathbf{T}_{1(k)} \end{bmatrix} \mathbf{R}({}_0\tilde{\boldsymbol{\theta}}_c^k) {}^t \begin{bmatrix} 1(k) & \mathbf{T}_{2(k)(m)} \end{bmatrix} \mathbf{R}({}_0\bar{\boldsymbol{\theta}}_w^{k(n)}) \bar{\mathbf{x}}_k^{(m)(n)} \right. \\ &\quad \left. + {}^{t+\Delta t}\boldsymbol{\varphi}_k^{(m)(n)} \quad {}^{t+\Delta t}\mathbf{V}_s^k \right) \end{aligned} \quad (3.13)$$

3.3 Incremental displacement interpolation

In Eq (3.13), all the rotation variables are described with respect to the current coordinate frames, which are cable local and wire local cross-sectional Cartesian coordinate system at the beam node k . In order to calculate the linearized incremental displacement field, the rotation variables ${}_0\tilde{\boldsymbol{\theta}}_c^k$ and ${}_0\bar{\boldsymbol{\theta}}_w^{k(n)}$ are represented with respect to the fixed reference frame $\{0\}$,

$$\begin{aligned}
{}^{t+\Delta t}\mathbf{x}^{(m)(n)} &= \sum_{k=1}^q h_k(r) \left({}^{t+\Delta t}\mathbf{x}_k^{(m)(n)} \right) \\
&= \sum_{k=1}^q h_k(r) \left({}^{t+\Delta t}\mathbf{x}_k + \mathbf{R}({}_0\boldsymbol{\theta}_c^k)^t \left[{}^0\mathbf{T}_{1(k)} \right] \tilde{\mathbf{x}}_k^{(m)(n)} + \mathbf{R}({}_0\boldsymbol{\theta}_w^{k(m)(n)}) \mathbf{R}({}_0\boldsymbol{\theta}_c^k)^t \left[{}^0\mathbf{T}_{2(k)(m)(n)} \right] \bar{\mathbf{x}}_k^{(m)(n)} \right. \\
&\quad \left. + {}^{t+\Delta t}\varphi_k^{(m)(n)} {}^{t+\Delta t}\mathbf{V}_s^k \right) \tag{3.14}
\end{aligned}$$

where

$$\mathbf{R}({}_0\boldsymbol{\theta}_c^k)^t \left[{}^0\mathbf{T}_{1(k)} \right] = {}^t \left[{}^0\mathbf{T}_{1(k)} \right] \mathbf{R}({}_0\tilde{\boldsymbol{\theta}}_c^k), \tag{3.15}$$

and

$$\mathbf{R}({}_0\boldsymbol{\theta}_c^k)^t \left[{}^0\mathbf{T}_{2(k)(m)} \right] \mathbf{R}({}_0\bar{\boldsymbol{\theta}}_w^{k(n)}) = \mathbf{R}({}_0\boldsymbol{\theta}_w^{k(m)(n)}) \mathbf{R}({}_0\boldsymbol{\theta}_c^k)^t \left[{}^0\mathbf{T}_{2(k)(m)} \right]. \tag{3.16}$$

Using Eq. (3.7) and Eq. (3.14), the incremental displacement interpolation for sub-wire m belonging to layer n of the cable is obtained from the configurations at times $t + \Delta t$ and t ,

$$\begin{aligned}
{}_0\mathbf{u}^{(m)(n)} &= {}^{t+\Delta t}\mathbf{x}^{(m)(n)} - {}^t\mathbf{x}^{(m)(n)} \\
&= \sum_{k=1}^q h_k(r) \left({}_0\mathbf{u}_k + \left(\mathbf{R}({}_0\boldsymbol{\theta}_c^k) - \mathbf{I} \right)^t \left[{}^0\mathbf{T}_{1(k)} \right] \tilde{\mathbf{x}}_k^{(m)(n)} + \left(\mathbf{R}({}_0\boldsymbol{\theta}_w^{k(m)(n)}) \mathbf{R}({}_0\boldsymbol{\theta}_c^k) - \mathbf{I} \right)^t \left[{}^0\mathbf{T}_{2(k)(m)(n)} \right] \right. \\
&\quad \left. + \sum_{k=1}^q h_k(r) \left({}^{t+\Delta t}\varphi_k^{(m)(n)} {}^{t+\Delta t}\mathbf{V}_s^k - {}^t\varphi_k^{(m)(n)} {}^t\mathbf{V}_s^k \right), \right) \tag{3.17}
\end{aligned}$$

where ${}_0\mathbf{u}_k$ is the incremental nodal displacement from time t to $t + \Delta t$ at beam node k

$${}_0\mathbf{u}_k = \left[{}_0u_k \quad {}_0v_k \quad {}_0w_k \right]^T \tag{3.18}$$

The finite rotation tensor $\mathbf{R}({}_0\boldsymbol{\theta}_c^k)$ and $\mathbf{R}({}_0\boldsymbol{\theta}_w^{k(m)(n)})$ are linearized by the use of the first-order Taylor polynomial approximation

$$\mathbf{R}({}_0\boldsymbol{\theta}_c^k) = \mathbf{I} + \sum_{n=1}^{\infty} \frac{1}{n!} \hat{\mathbf{R}}({}_0\boldsymbol{\theta}_c^k)^n \approx \mathbf{I} + \hat{\mathbf{R}}({}_0\boldsymbol{\theta}_c^k), \tag{3.19}$$

and

$$\mathbf{R}({}_0\boldsymbol{\theta}_w^{k(m)(n)}) = \mathbf{I} + \sum_{n=1}^{\infty} \frac{1}{n!} \hat{\mathbf{R}}({}_0\boldsymbol{\theta}_w^{k(m)(n)})^n \approx \mathbf{I} + \hat{\mathbf{R}}({}_0\boldsymbol{\theta}_w^{k(m)(n)}). \tag{3.20}$$

The slip director vector ${}^{t+\Delta t}\mathbf{V}_s^k$ in the configuration at time $t + \Delta t$ is approximated in terms of the slip director vector at time t and the incremental nodal displacement

$${}^{t+\Delta t}\mathbf{V}_s^k = \frac{{}^{t+\Delta t}\mathbf{g}_x^k}{\|{}^{t+\Delta t}\mathbf{g}_x^k\|} \approx {}^t\mathbf{V}_s^k + \frac{1}{\|{}^t\mathbf{g}_x^k\|} \sum_{\xi=1}^q \frac{\partial h_{\xi}(r)}{\partial r} \Big|_{r=r_k} {}_0\mathbf{u}_{\xi}. \tag{3.21}$$

Substituting Eqs. (3.19), (3.20) and (3.21) into Eq. (3.17), the incremental displacement of sub-wire m belonging to layer n becomes

$$\begin{aligned}
{}_0\mathbf{u}^{(m)(n)} \approx & \sum_{k=1}^q h_k(r) \left(({}_0\mathbf{u}_k) + \hat{\mathbf{R}}({}_0\boldsymbol{\theta}_c)^t [{}^0\mathbf{T}_{1(k)}] \tilde{\mathbf{x}}_k^{(m)(n)} + \left(\hat{\mathbf{R}}({}_0\boldsymbol{\theta}_c) + \hat{\mathbf{R}}({}_0\boldsymbol{\theta}_w^{k(m)(n)}) \right)^t [{}^0\mathbf{T}_{2(k)(m)(n)}] \bar{\mathbf{x}}_k^{(m)(n)} \right. \\
& + \hat{\mathbf{R}}({}_0\boldsymbol{\theta}_w^{k(m)(n)}) \hat{\mathbf{R}}({}_0\boldsymbol{\theta}_c)^t [{}^0\mathbf{T}_{2(k)(m)(n)}] \bar{\mathbf{x}}_k^{(m)(n)} \\
& \left. + {}_0\varphi_k^{(m)(n)} {}^t\mathbf{V}_s^k + \left({}^t\varphi_k^{(m)(n)} + {}_0\varphi_k^{(m)(n)} \right) \left(\frac{1}{\|{}^t\mathbf{g}_x^k\|} \sum_{\xi=1}^q h'_\xi(r) {}_0\mathbf{u}_\xi \right) \right), \quad (3.22)
\end{aligned}$$

where ${}_0\varphi_k^{(m)(n)}$ is the incremental layer DOF corresponding to the layer n at beam node k .

In Eq. (3.22), all the rotation variables are expressed with respect to the fixed coordinate frame $\{0\}$. As the cable local rotation at beam node k uniformly occurs in the entire cable structure with respect to a single coordinate frame $\{1\}$, it can be expressed based on the fixed coordinate frame $\{0\}$. In the case of the wire local rotation, however, the rotation variables should be expressed based on the wire local coordinate system in order to represent all the wire local rotation in the same layer without using different DOFs for each wire. Because the wires in the same layer have the equivalent curvature and twist values, but each of them has different rotating axes. Therefore, expressing the wire local rotation with respect to the local axis of each wire, the wire local rotation of all the wires in the same layer can be defined using an angle vector.

Using Eqs. (3.16) and (3.22) and applying the first-order approximation, the linearized incremental displacement ${}_0\bar{\mathbf{u}}^{(m)(n)}$ for sub-beam m of layer n is obtained

$$\begin{aligned}
{}_0\mathbf{u}^{(m)(n)} \approx & {}_0\bar{\mathbf{u}}^{(m)(n)} = \sum_{k=1}^q h_k(r) \left(({}_0\mathbf{u}_k) + \hat{\mathbf{R}}({}_0\boldsymbol{\theta}_c) [{}^t\mathbf{V}^k] \tilde{\mathbf{x}}_k^{(m)(n)} + \hat{\mathbf{R}}({}_0\boldsymbol{\theta}_c) [{}^t\mathbf{n}^{k(m)(n)}] \bar{\mathbf{x}}_k^{(m)(n)} \right. \\
& + [{}^t\mathbf{n}^{k(m)(n)}] \hat{\mathbf{R}}({}_0\bar{\boldsymbol{\theta}}_w^{k(n)}) \bar{\mathbf{x}}_k^{(m)(n)} + \hat{\mathbf{R}}({}_0\boldsymbol{\theta}_c) [{}^t\mathbf{n}^{k(m)(n)}] \hat{\mathbf{R}}({}_0\bar{\boldsymbol{\theta}}_w^{k(n)}) \bar{\mathbf{x}}_k^{(m)(n)} \\
& \left. + {}_0\varphi_k^{(m)(n)} {}^t\mathbf{V}_s^k + {}^t\varphi_k^{(m)(n)} \left(\frac{1}{\|{}^t\mathbf{g}_x^k\|} \sum_{\xi=1}^q h'_\xi(r) {}_0\mathbf{u}_\xi \right) \right), \quad (3.23)
\end{aligned}$$

where

$$[{}^t\mathbf{V}^k] = \begin{bmatrix} {}^t\mathbf{V}_x^k & {}^t\mathbf{V}_y^k & {}^t\mathbf{V}_z^k \end{bmatrix}, \quad (3.24)$$

$$[{}^t\mathbf{n}^{k(m)(n)}] = \begin{bmatrix} {}^t\mathbf{n}_x^{k(m)(n)} & {}^t\mathbf{n}_y^{k(m)(n)} & {}^t\mathbf{n}_z^{k(m)(n)} \end{bmatrix}. \quad (3.25)$$

3.4 Incremental equilibrium equations

The covariant component of the Green–Lagrange strain for sub-wire m belonging to layer n , in the configuration at time t referred to the configuration at time 0 is given by

$${}^t_0\tilde{\mathcal{E}}_{ij}^{(m)(n)} = \frac{1}{2}({}^t\mathbf{g}_i^{(m)(n)} \cdot {}^t\mathbf{g}_j^{(m)(n)} - {}^0\mathbf{g}_i^{(m)(n)} \cdot {}^0\mathbf{g}_j^{(m)(n)}) \quad \text{with} \quad {}^t\mathbf{g}_i^{(m)(n)} = \frac{\partial {}^t\mathbf{x}^{(m)(n)}}{\partial r_i}, \quad (3.26)$$

where ${}^t\mathbf{g}_i^{(m)(n)}$ is the covariant base vector and r_i indicates the natural coordinates (r, s, t) : $r_1 = r$, $r_2 = s$ and $r_3 = t$.

The covariant component of the incremental Green–Lagrange strain is obtained from the strains in the configurations at time $t + \Delta t$ and t

$${}^0\tilde{\mathcal{E}}_{ij}^{(m)(n)} = {}^{t+\Delta t}{}^0\tilde{\mathcal{E}}_{ij}^{(m)(n)} - {}^t{}^0\tilde{\mathcal{E}}_{ij}^{(m)(n)} \quad (3.27)$$

and it can be decomposed into linear and nonlinear parts, ${}^0\tilde{\mathcal{e}}_{ij}^{(m)(n)}$ and ${}^0\tilde{\mathcal{h}}_{ij}^{(m)(n)}$, respectively,

$${}^0\tilde{\mathcal{E}}_{ij}^{(m)(n)} = {}^0\tilde{\mathcal{e}}_{ij}^{(m)(n)} + {}^0\tilde{\mathcal{h}}_{ij}^{(m)(n)}, \quad (3.28)$$

with

$${}^0\tilde{\mathcal{e}}_{ij}^{(m)(n)} = \frac{1}{2}({}^t\mathbf{g}_i^{(m)(n)} \cdot \frac{\partial {}^0\mathbf{u}^{(m)(n)}}{\partial r_j} + {}^t\mathbf{g}_j^{(m)(n)} \cdot \frac{\partial {}^0\mathbf{u}^{(m)(n)}}{\partial r_i}) \quad (3.29)$$

and

$${}^0\tilde{\mathcal{h}}_{ij}^{(m)(n)} = \frac{1}{2} \frac{\partial {}^0\mathbf{u}^{(m)(n)}}{\partial r_i} \cdot \frac{\partial {}^0\mathbf{u}^{(m)(n)}}{\partial r_j}. \quad (3.30)$$

The incremental Green–Lagrange strain components, which are described in the wire local Cartesian coordinate system defined on the center helix line of wire m , is evaluated through the following transformation

$${}^0\bar{\mathcal{e}}_{ij}^{(m)(n)} = ({}^0\mathbf{t}_i^{(m)(n)} \cdot {}^0\mathbf{g}^{k(m)(n)}) ({}^0\mathbf{t}_j^{(m)(n)} \cdot {}^0\mathbf{g}^{l(m)(n)}) {}^0\tilde{\mathcal{e}}_{kl}^{(m)(n)}, \quad (3.31)$$

$${}^0\bar{\mathcal{h}}_{ij}^{(m)(n)} = ({}^0\mathbf{t}_i^{(m)(n)} \cdot {}^0\mathbf{g}^{k(m)(n)}) ({}^0\mathbf{t}_j^{(m)(n)} \cdot {}^0\mathbf{g}^{l(m)(n)}) {}^0\tilde{\mathcal{h}}_{kl}^{(m)(n)}, \quad (3.32)$$

where ${}^0\mathbf{g}^{k(m)(n)}$ is the contravariant base vector calculated using ${}^0\mathbf{g}^{k(m)(n)} \cdot {}^0\mathbf{g}_l^{(m)(n)} = \delta_l^k$ and ${}^0\mathbf{t}_i^{(m)(n)}$ is the base vector of the wire local Cartesian coordinate system, which are determined by

$${}^0\mathbf{t}_1^{(m)(n)} = h_k(r) {}^0\mathbf{n}_x^{k(m)(n)}, \quad {}^0\mathbf{t}_2^{(m)(n)} = h_k(r) {}^0\mathbf{n}_y^{k(m)(n)} \quad \text{and} \quad {}^0\mathbf{t}_3^{(m)(n)} = h_k(r) {}^0\mathbf{n}_z^{k(m)(n)}. \quad (3.33)$$

The linearized equilibrium equation in the total Lagrangian formulation is given by [26]

$$\int_{^0V} \bar{C}_{ijkl} \bar{e}_{ij} \delta_0 \bar{e}_{kl} d^0V + \int_{^0V} {}^t\bar{S}_{ij} \delta_0 \bar{\eta}_{ij} d^0V = {}^{t+\Delta t}\mathfrak{R} - \int_{^0V} {}^t\bar{S}_{ij} \delta_0 \bar{e}_{ij} d^0V, \quad (3.34)$$

in which 0V and 0L denote the volume and length of the beams, respectively, in the configuration at time 0, \bar{C}_{ijkl} is the material law tensor for beams, ${}^0\bar{e}_{ij}$ and ${}^0\bar{\eta}_{ij}$ are the linear and nonlinear parts of the incremental local Green–Lagrange strain, ${}^{t+\Delta t}{}^0\bar{S}_{ij}$ is the local second Piola–Kirchhoff stress, ${}^{t+\Delta t}{}^0\bar{e}_{ij}$ is the local Green–Lagrange strain, ${}^{t+\Delta t}\mathfrak{R}$ is the external virtual work, and δ denotes virtual quantities.

Expressing Eq. (3.34) as a sum of integrations over the volume of each sub-wire m of layer n in the configuration at time 0 (${}^0V^{(m)(n)}$),

$$\begin{aligned} & \sum_n \sum_m \int_{^0V^{(m)(n)}} \bar{C}_{ijkl}^{(m)(n)} \bar{e}_{ij}^{(m)(n)} \delta_0 \bar{e}_{kl}^{(m)(n)} d^0V^{(m)(n)} + \sum_n \sum_m \int_{^0V^{(m)(n)}} {}^t\bar{S}_{ij}^{(m)(n)} \delta_0 \bar{\eta}_{ij}^{(m)(n)} d^0V^{(m)(n)} \\ & = {}^{t+\Delta t}\mathfrak{R} - \sum_n \sum_m \int_{^0V^{(m)(n)}} {}^t\bar{S}_{ij}^{(m)(n)} \delta_0 \bar{e}_{ij}^{(m)(n)} d^0V^{(m)(n)} \end{aligned} \quad (3.35)$$

In the beam formulation, only five covariant components of the Green–Lagrange strain are of interest, (i.e. $(i, j) \in \{(1, 1), (1, 2), (2, 1), (1, 3), (3, 1)\}$), and the material law tensor has only five non-zero components: $\bar{C}_{1111} = E$ and $\bar{C}_{1212} = \bar{C}_{2121} = \bar{C}_{1313} = \bar{C}_{3131} = G$ with Young’s modulus E and shear modulus G .

3.5 Finite element formulations

In a q -node continuum mechanics based beam element, the nodal DOFs vector ${}^0\mathbf{U}$ consists of the DOFs vector ${}^0\mathbf{U}_k$ at beam node k

$${}^0\mathbf{U} = \left[{}^0\mathbf{U}_1^T \quad {}^0\mathbf{U}_2^T \quad \dots \quad {}^0\mathbf{U}_q^T \right]^T \quad (3.36)$$

where

$${}^0\mathbf{U}_k = \left[{}^0\mathbf{u}_k \quad {}^0\boldsymbol{\theta}_c^k \quad {}^0\bar{\boldsymbol{\theta}}_w^{k(1)} \quad \dots \quad {}^0\bar{\boldsymbol{\theta}}_w^{k(n_L)} \quad {}^0\boldsymbol{\Phi}_k \right]^T \quad (3.37)$$

with

$${}^0\mathbf{u}_k = \left[{}^0u_k \quad {}^0v_k \quad {}^0w_k \right]^T, \quad (3.38)$$

$${}^0\boldsymbol{\theta}_c^k = \left[{}^0\theta_{cx}^k \quad {}^0\theta_{cy}^k \quad {}^0\theta_{cz}^k \right]^T, \quad (3.39)$$

$${}^0\bar{\boldsymbol{\theta}}_w^{k(n)} = \left[{}^0\bar{\theta}_{wx}^{k(n)} \quad {}^0\bar{\theta}_{wy}^{k(n)} \quad {}^0\bar{\theta}_{wz}^{k(n)} \right]^T, \quad (3.40)$$

$${}_0\boldsymbol{\Phi}_k = \begin{bmatrix} {}_0\varphi_k^{(1)} & \cdots & {}_0\varphi_k^{(n_w)} \end{bmatrix}^T, \quad (3.41)$$

and n_L and n_w denote the total number of layers and wires of the cable, respectively.

Employing Eq. (3.36), the incremental displacements ${}_0\bar{\mathbf{u}}^{(m)(n)}$ for sub-wire m of layer n in Eq. (3.23) is represented in terms of the nodal DOFs vector ${}_0\mathbf{U}$:

$${}_0\bar{\mathbf{u}}^{(m)(n)} = \begin{bmatrix} \mathbf{L}_1^{(m)(n)} & \mathbf{L}_2^{(m)(n)} & \cdots & \mathbf{L}_q^{(m)(n)} \end{bmatrix} {}_0\mathbf{U} = \mathbf{L}^{(m)(n)} {}_0\mathbf{U} \quad (3.42)$$

$$\text{where } \mathbf{L}_k^{(m)(n)} = \begin{bmatrix} \left(h_k(r) + {}^t\phi_k^{(m)(n)}(r) \right) \mathbf{I} & -h_k(r) \left({}^t\Psi_1^{k(m)(n)} \right) & -h_k(r) \left({}^t\Psi_2^{k(m)(n)} \right) & \mathbf{0} \right] \\ + h_k(r) {}^t\mathbf{V}_s^k \mathbf{Q}^{(m)(n)} \end{bmatrix} \quad (3.43)$$

$$\text{with } {}^t\phi_k^{(m)(n)}(r) = \sum_{\xi=1}^q \frac{\partial h_k(r)}{\partial r} \Big|_{r=r_\xi} h_\xi(r) \frac{{}^t\varphi_\xi^{(m)(n)}}{\|{}^t\mathbf{g}_x^\xi\|}, \quad (3.44)$$

$${}^t\Psi_1^{k(m)(n)} = \tilde{y}_k^{(m)(n)} \hat{\mathbf{R}}({}^t\mathbf{V}_y^k) + \tilde{z}_k^{(m)(n)} \hat{\mathbf{R}}({}^t\mathbf{V}_z^k) + \bar{y}_k^{(m)(n)} \hat{\mathbf{R}}({}^t\mathbf{n}_y^{k(m)(n)}) + \bar{z}_k^{(m)(n)} \hat{\mathbf{R}}({}^t\mathbf{n}_z^{k(m)(n)}), \quad (3.45)$$

$${}^t\Psi_2^{k(m)(n)} = \bar{y}_k^{(m)(n)} \left[{}^t\mathbf{n}^{k(m)(n)} \right] \hat{\mathbf{R}}(\mathbf{e}_2) + \bar{z}_k^{(m)(n)} \left[{}^t\mathbf{n}^{k(m)(n)} \right] \hat{\mathbf{R}}(\mathbf{e}_3), \quad (3.46)$$

and $\mathbf{Q}^{(m)(n)}$ is a Boolean matrix for the wire DOFs ${}_0\varphi_k^{(m)(n)}$ such that

$${}_0\varphi_k^{(m)(n)} = \mathbf{Q}^{(m)(n)} {}_0\mathbf{U}_k. \quad (3.47)$$

The linear and nonlinear parts of the covariant Green–Lagrange strain in Eq. (3.29) and Eq. (3.30) are also expressed in terms of ${}_0\mathbf{U}$:

$${}_0\tilde{\mathbf{e}}_{ij}^{(m)(n)} = \frac{1}{2} \left({}^t\mathbf{g}_i^{(m)(n)} \cdot \frac{\partial \mathbf{L}^{(m)(n)}}{\partial r_j} + {}^t\mathbf{g}_j^{(m)(n)} \cdot \frac{\partial \mathbf{L}^{(m)(n)}}{\partial r_i} \right) {}_0\mathbf{U} = \mathbf{B}_{ij}^{(m)(n)} {}_0\mathbf{U}, \quad (3.48)$$

$${}_0\tilde{\boldsymbol{\eta}}_{ij}^{(m)(n)} = \frac{1}{2} {}_0\mathbf{U}^T \left(\frac{\partial \mathbf{L}^{(m)(n)T}}{\partial r_i} \frac{\partial \mathbf{L}^{(m)(n)}}{\partial r_j} \right) {}_0\mathbf{U} = \frac{1}{2} {}_0\mathbf{U}^T \mathbf{N}_{ij}^{(m)(n)} {}_0\mathbf{U}. \quad (3.49)$$

The local Green–Lagrange strains are obtained using Eq. (3.29), Eq. (3.30), Eq. (3.48), and Eq. (3.49):

$${}_0\bar{\mathbf{e}}_{ij}^{(m)(n)} = ({}_0\mathbf{t}_i^{(m)(n)} \cdot {}_0\mathbf{g}^{k(m)(n)}) ({}_0\mathbf{t}_j^{(m)(n)} \cdot {}_0\mathbf{g}^{l(m)(n)}) \mathbf{B}_{kl}^{(m)(n)} {}_0\mathbf{U} = \bar{\mathbf{B}}_{ij}^{(m)(n)} {}_0\mathbf{U}, \quad (3.50)$$

$${}_0\bar{\boldsymbol{\eta}}_{ij}^{(m)(n)} = \frac{1}{2} {}_0\mathbf{U}^T ({}_0\mathbf{t}_i^{(m)(n)} \cdot {}_0\mathbf{g}^{k(m)(n)}) ({}_0\mathbf{t}_j^{(m)(n)} \cdot {}_0\mathbf{g}^{l(m)(n)}) \mathbf{N}_{kl}^{(m)(n)} {}_0\mathbf{U} = \frac{1}{2} {}_0\mathbf{U}^T \bar{\mathbf{N}}_{ij}^{(m)(n)} {}_0\mathbf{U}. \quad (3.51)$$

The virtual local Green–Lagrange strains are obtained

$$\delta_0 \bar{e}_{ij}^{(m)(n)} = \bar{\mathbf{B}}_{ij}^{(m)(n)} \delta_0 \mathbf{U} \quad \text{and} \quad \delta_0 \bar{\eta}_{ij}^{(m)(n)} = \delta_0 \mathbf{U}^T \bar{\mathbf{N}}_{ij}^{(m)(n)} \mathbf{U}. \quad (3.52)$$

Substituting Eqs. (3.50)–(3.52) into Eq. (3.35), the following finite element formulation is constructed with the tangent stiffness matrix ${}^t \mathbf{K}$:

$${}^t \mathbf{K}_0 \mathbf{U} = {}^{t+\Delta t} \mathbf{R} - {}^t \mathbf{F}_i \quad \text{with} \quad {}^t \mathbf{K} = {}^t \mathbf{K}_L + {}^t \mathbf{K}_{NL}, \quad (3.53)$$

where

$${}^t \mathbf{K}_L = \sum_n \sum_m \int_{0V^{(m)(n)}} \bar{\mathbf{B}}_{ij}^{(m)(n)T} {}^t \bar{C}_{ijkl} \bar{\mathbf{B}}_{kl}^{(m)(n)} dV^{(m)(n)}, \quad (3.54)$$

$${}^t \mathbf{K}_{NL} = \sum_n \sum_m \int_{0V^{(m)(n)}} \bar{\mathbf{N}}_{ij}^{(m)(n)} {}^t \bar{S}_{ij} dV^{(m)(n)}, \quad (3.55)$$

$${}^t \mathbf{F} = \sum_n \sum_m \int_{0V^{(m)(n)}} \bar{\mathbf{B}}_{ij}^{(m)(n)T} {}^t \bar{S}_{ij} dV^{(m)(n)}. \quad (3.56)$$

The complete tangent stiffness matrix for the analysis of helically stranded cable structure can be constructed by the assemblage of the elemental stiffness matrices using the direct stiffness procedure. For the analysis of cable structure that consists of n_L -layer and n_w -wire, the proposed beam finite element model uses $(6 + 3n_L + n_w)$ DOFs at each beam node (three translation and three rotation variables for cable structure, three wire rotation variables per each layer, and wire DOFs required per each wire to represent the relative slip displacement).

The incremental displacement ${}_0 \mathbf{U}$ is obtained in each incremental step by solving Eq. (3.53). Then, the position vector of each beam node k and the wire DOFs at beam node k are additively updated as

$${}^{t+\Delta t} \mathbf{x}_k = {}^t \mathbf{x}_k + \begin{bmatrix} {}_0 \mathbf{u}_k \\ {}_0 \mathbf{v}_k \\ {}_0 \mathbf{w}_k \end{bmatrix} \quad \text{and} \quad {}^{t+\Delta t} \varphi_k^{(m)(n)} = {}^t \varphi_k^{(m)(n)} + {}_0 \varphi_k^{(m)(n)}. \quad (3.57)$$

The basis vectors of cable local and wire local coordinate frames are updated as follows:

$$\begin{bmatrix} {}^{t+\Delta t} \mathbf{V}^k \end{bmatrix} = \mathbf{R}({}_0 \boldsymbol{\theta}_c^k) \begin{bmatrix} {}^t \mathbf{V}^k \end{bmatrix}, \quad (3.58)$$

$$\begin{bmatrix} {}^{t+\Delta t} \mathbf{n}^{k(m)(n)} \end{bmatrix} = \mathbf{R}({}_0 \boldsymbol{\theta}_c^k) \begin{bmatrix} {}^t \mathbf{n}^{k(m)(n)} \end{bmatrix} \mathbf{R}({}_0 \bar{\boldsymbol{\theta}}_w^{k(n)}). \quad (3.59)$$

3.6 Numerical examples

In this section, we demonstrate the modeling capability and performance of the continuum mechanics based beam elements for the helically stranded cable structures. To model the helically stranded cable structures, 2-node continuum mechanics based beam elements are used, and the reduced integration scheme is adopted along the longitudinal direction to avoid shear locking [24]. For the cross-section modeling, 9-, 16- and 25-node cross-sectional elements are used, and 3×3 , 4×4 and 5×5 Gauss integration is performed in each cross-sectional element respectively.

In order to solve nonlinear equilibrium equations, solutions are obtained using the standard full Newton–Raphson iterative scheme. For material nonlinear problems, the von Mises plasticity model with linear isotropic hardening law is implemented. At each integration point in the beam model, the constitutive equations are implicitly solved using the return mapping scheme [30]. In order to assess the proposed beam finite element, the results obtained from the present beam model are compared with the reference solutions, which are obtained from analytical theory in [55] or experimental results from previous research.

3.6.1 Convergence study of 7-wire strand cable under tension

First, the modeling capability of the proposed beam element model according to the degree of the helical geometry of the strand cable are examined. As shown in Fig. 26, for a 7-wire cantilever cable of length $L = 10$ subjected to tip axial loading $F_x = 1000$, various helical geometry is tested while the lay angle α , which is the rotating angle of the wires with respect to longitudinal axis of the cable, increases from 0° to 30° . The radii of the core and outer wires are $R_0 = 0.125$ and $R_1 = 0.1$, respectively, and materials of the core and the wires are linear elastic with Young's modulus $E = 28.5 \times 10^6$ and Poisson's ratio $\nu = 0$.

When constructing numerical model for the finite element analysis of a cable, the minimum number of finite elements required for appropriate results is generally dependent on the helical geometry of the wires that constitute the cable, not on the length of the entire cable. This is because the length of the wound wires changes depending on the lay angle, even if the length of the entire cable is the same. Therefore, the required number of

elements are determined based on the pitch length (or lay length), which is the length of the cable while the wires rotates 360° with respect to the longitudinal axis of the cable. In the present beam model, the various geometries of the strand cables are modeled using continuum mechanics based beam elements in which the total number of elements used are determined based on the number of elements per pitch length N_p , and the cross-section of the core and wires are discretized using 16-node cross-sectional elements.

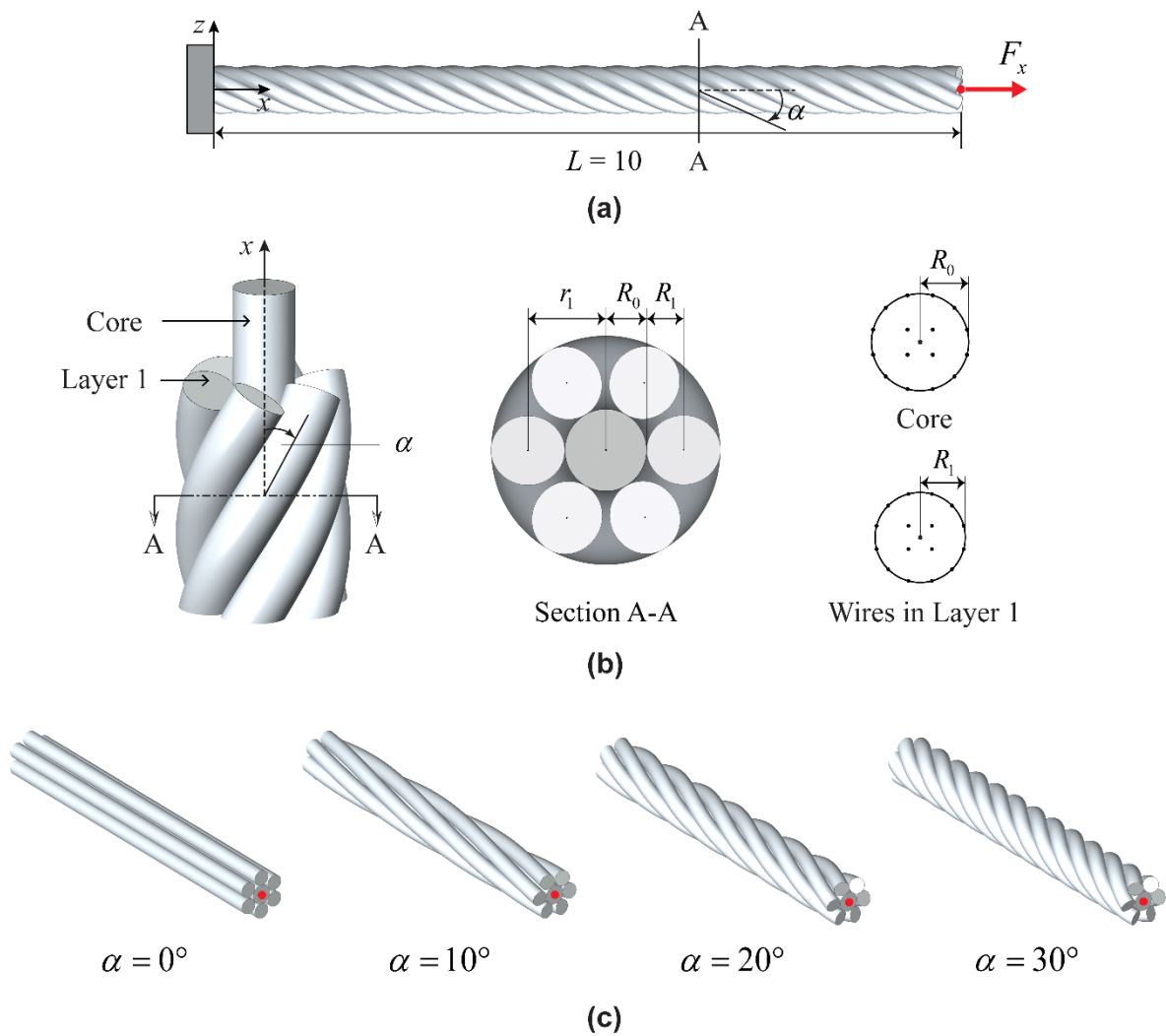


Fig. 27. Cantilever 7-wire strand cable subjected to tip tensile loading $F_x = 1000$: (a) Problem description, (b) Cross-sectional geometry of the strand cable, and (c) Various helical geometries of the strand cable when lay angle $\alpha = 0^\circ$, 10° , 20° and 30° .

Fig. 28 compares the axial displacements and torsional angles at the tip of the strand cables obtained from the present beam model with the analytical references as the number of elements per pitch length increase from $N_p = 4$ to 20. When insufficient number of elements per pitch length is used such as $N_p = 4$, considerable differences from the analytical references are observed as the precision of the numerical model is low. In order to obtain the numerical results consistent with the analytical references for all lay angles, at least 20 elements per pitch length is required. The use of 20 elements per pitch length ($N_p = 20$) means that one element is used whenever the wires rotate 18° . When 20 elements per pitch were used, the differences between the results obtained from the present beam model and the analytical reference are less than 2%.

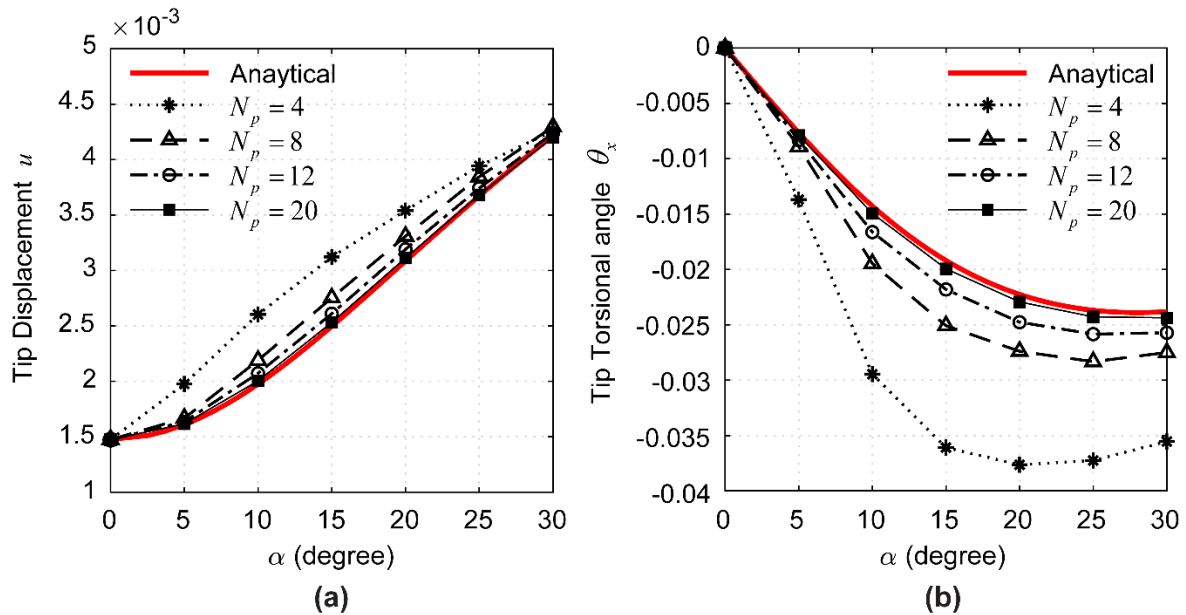


Fig. 28. (a) and (b) Tip displacement and torsional angle under tensile loading F_x obtained from the various geometries of strand cables (from $\alpha = 0^\circ$ to 30°) when number of element per pitch length $N_p = 4, 8, 12$ and 20 .

3.6.2 Convergence study of 7-wire strand cable under bending

In the second example (Fig. 29), the modeling performance and the required number of elements per pitch length are examined when a 7-wire strand cable is subjected to tip bending moment $M_y = 100$. The geometric and material properties of the cable are same to those of the two-layer beam problem in section 3.5.1 except for

the loading condition. As in the section 3.5.1, the geometries of the strand cables according to the lay angles from $\alpha = 0^\circ$ to 30° are modeled using continuum mechanics based beam elements. The total number of elements used are determined based on the number of elements per pitch length N_p , and the cross-section of the core and wires are discretized using 16-node cross-sectional elements.

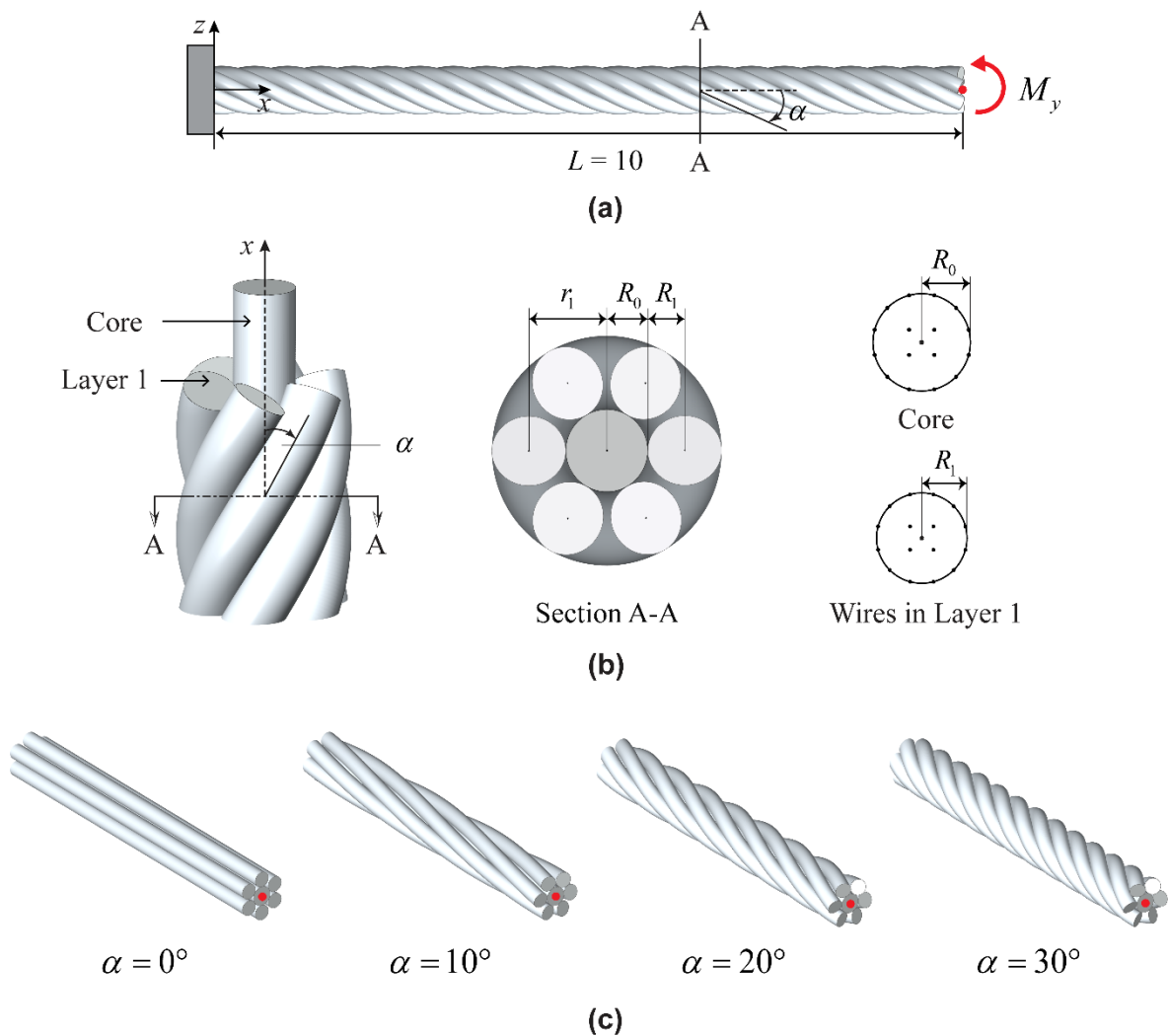


Fig. 29. Cantilever 7-wire strand cable subjected to tip bending moment $M_y = 100$: (a) Problem description, (b) Cross-sectional geometry of the strand cable, and (c) Various helical geometries of the strand cable when lay angle $\alpha = 0^\circ$, 10° , 20° and 30° .

Fig. 30 compares the deflections and bending angles at the tip of the strand cable obtained from the present beam model with the analytical references as the number of elements per pitch length increase from $N_p = 4$ to 20. In the case of strand cable subjected to bending moment required more elements per pitch than those (20 elements per pitch) required in the case subjected to tensile loading. As shown in Fig. 30, approximately 30 elements per pitch length is required to obtain the same degree of accuracy as in tension problem of section 3.5.1 for all the lay angle ranging from 0° to 30° . The use of 30 elements per pitch means that one element is used whenever the wires rotate 12° .

It is observed that the behaviors of the cable subjected to bending moment required more detailed numerical modeling rather than those under uniform tension. This is mainly because the effect of inter-wire slip behavior increases in the bending dominated loading conditions, thus the cable subjected to the bending moment exhibits more complex behaviors than the one under the uniform tensile loading.

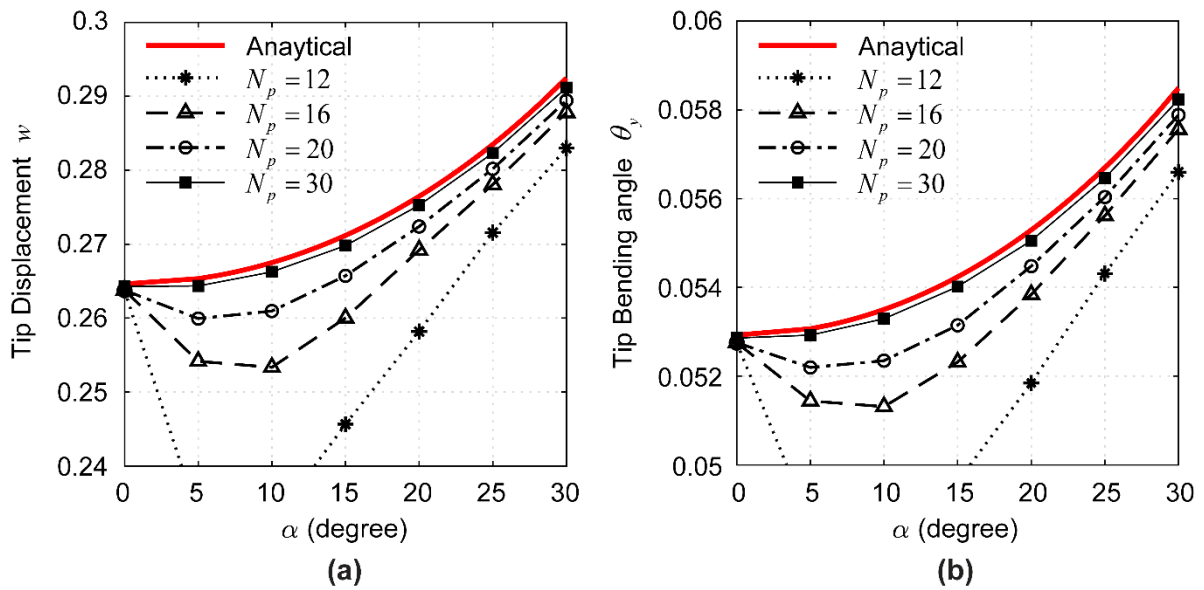


Fig. 30. (a) and (b) Tip displacement and torsional angle under bending moment M_y obtained from the various geometries of strand cables (from $\alpha = 0^\circ$ to 30°) when number of element per pitch length $N_p = 12, 16, 20$ and 30 .

3.6.3 Cross-sectional interpolation test

For the strand cable that has the same geometric and material properties as those in section 3.5.1 and 3.5.2, the influence of the cross-sectional interpolation is tested considering both uniform tension $F_x = 1000$ and bending moment $M_y = 100$ (Load Case I and Load Case II in Fig. 31(a)). For both load cases, the cross section of the core and wire are interpolated using 9-, 16-, and 25-node cross-sectional elements as shown in Fig. 31(b), and 3×3 , 4×4 and 5×5 Gauss integration is performed in each cross-sectional element respectively. The geometries of the strand cables due to the lay angles from $\alpha = 0^\circ$ to 30° are modeled using continuum mechanics based beam elements where the number of element per pitch length is $N_p = 30$.

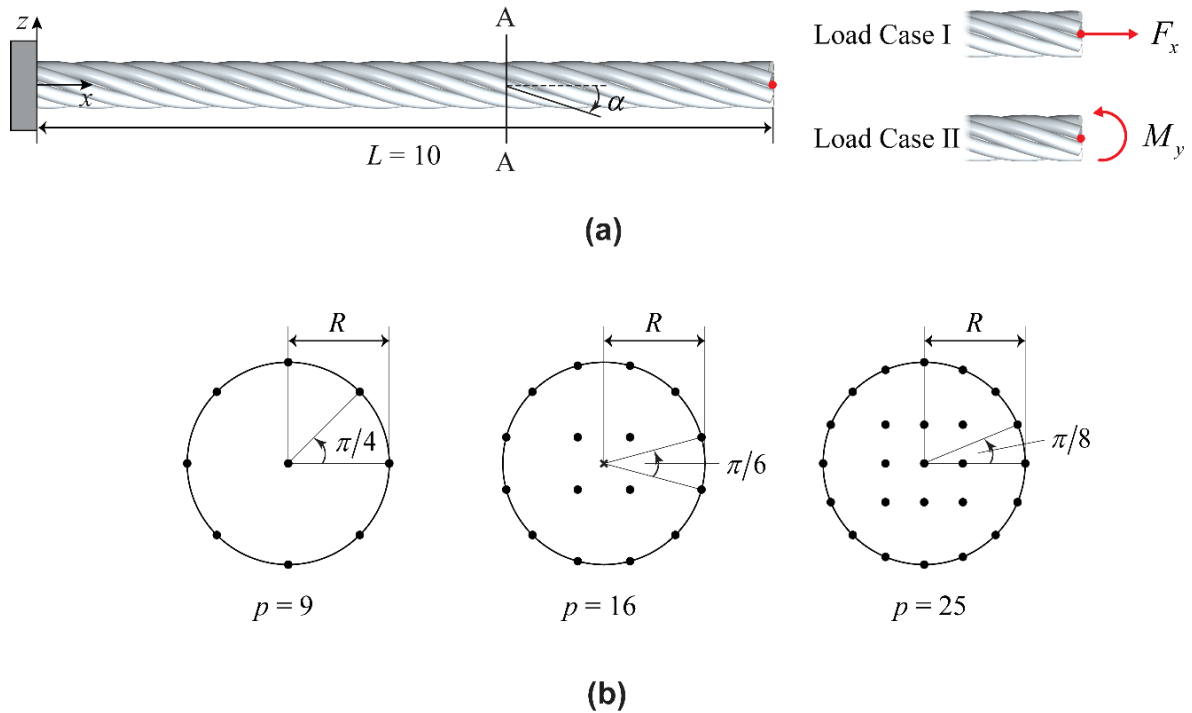


Fig. 31. (a) Cantilever 7-wire strand cable under Load Case I and Load Case II and (b) Cross-sectional modeling for the core and wires using 9-, 16-, and 25-node cross-sectional elements, respectively.

Fig. 32(a) shows the axial displacements and torsional angles at the tip of the cable when three cross-sectional discretization cases are considered under Load Case I. It is observed that there are no significant differences between three cross-sectional discretization cases under tensile loading, and all the results are in good

agreement with the analytical reference as the differences are less than 5%. Fig. 32(b) shows the deflections and bending angles at the tip of the cable when three cross-sectional discretization cases are considered under Load Case II. Unlike Load Case I, considerable differences from the analytical references are observed when 9-node cross-sectional interpolation is used in Load Case II. In order to obtain results that are consistent with the analytical reference with differences less than 5% in Load case II, at least 16-node cross-sectional interpolation is required.

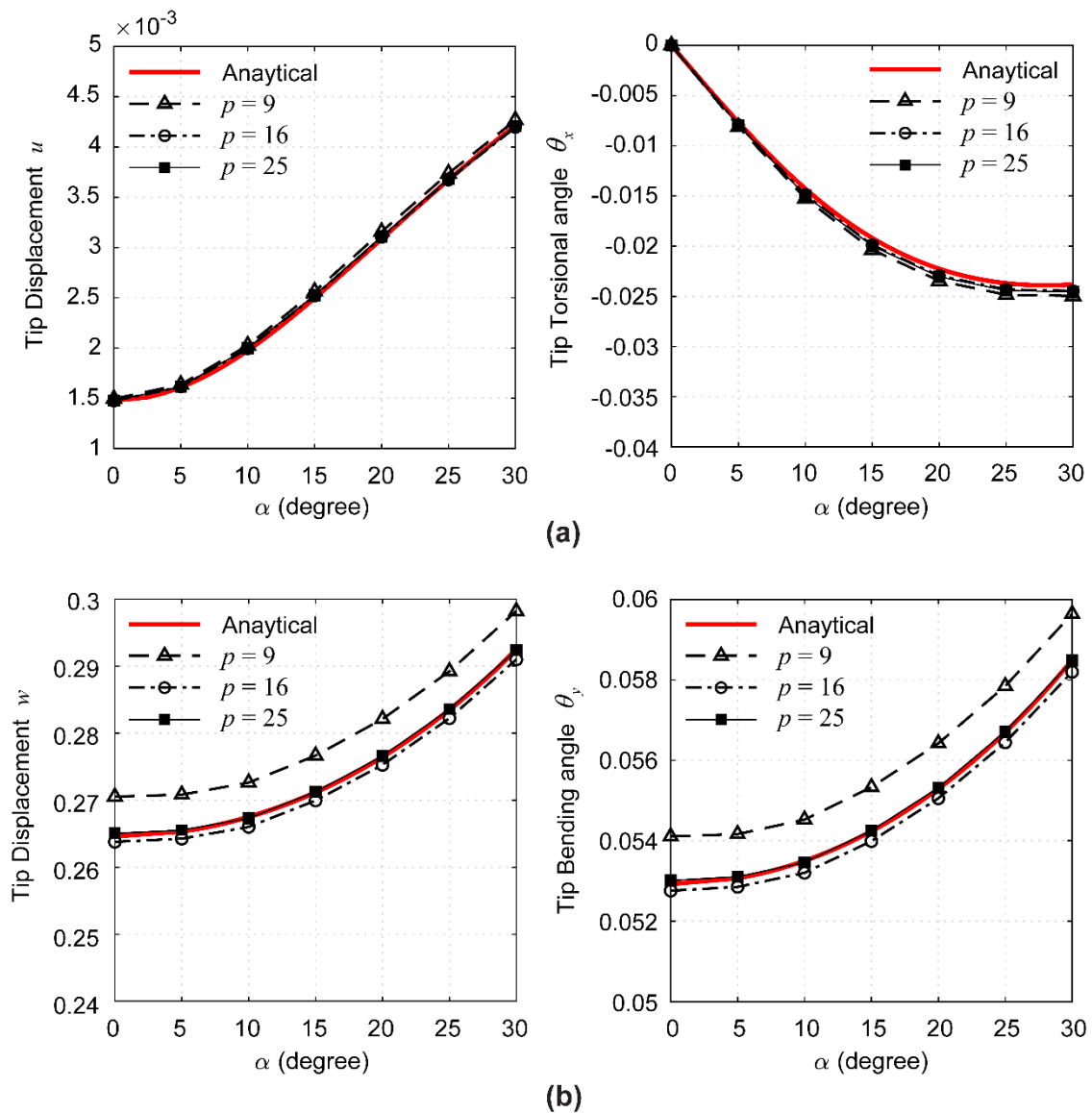


Fig. 32. (a) Tip axial displacements and torsional angles under Load Case I, (b) Tip deflections and bending angle under Load Case II.

As mentioned in section in 3.5.2, this is because the behaviors of the cable subjected to bending moment required more detailed numerical modeling rather than those under uniform tension. If the behavior of the entire structure of the cable is approximated to be a single beam, it can be said that the behavioral characteristics of the cable are governed by the axial rigidity of the beam under the tension dominated loading conditions and by the bending rigidity of the beam under the bending dominated loading conditions. The axial and bending rigidities are determined by area characteristics of the beam cross section and the moment of inertia for the beam cross section, respectively, in addition to Young's modulus. Therefore, the errors in cross-sectional area of the core and wires according to the degree of interpolation more influence on the second moment of inertia of the bending rigidity (m^4 unit) than on the area for the axial rigidity (m^2 unit), and because of this, more higher order cross-sectional element is required for the analysis of the bending dominated behavior of the cable.

3.6.4 Comparison with experimental test: Cantilever 7-wire helically-stranded cable

Here, the present beam model is compared with the experimental results obtained from the uniaxial tensile tests of a 7-wire cantilever strand cable conducted by Utting and Jones [39-42]. In the experimental test, tensile loading is applied to the tip of the cantilever cable while the torsional angle of the entire cable was restrained to prevent twisting in the cable structure, and the axial strain and reaction torque were measured. The lay angle of the helical wires is 17.03° , the pitch length of the cable is 78.66 mm , and the radii of the core and helical wires are $R_0 = 3.94 \text{ mm}$ and $R_1 = 0.1$, respectively. The cable is composed of elasto-plastic material in which Young's modulus $E = 188 \text{ GPa}$, Poisson's ratio $\nu = 0.3$, the initial yield stress $Y_0 = 1.540 \text{ GPa}$ and the linear hardening modulus $H = 24.6 \text{ GPa}$.

In the present beam model, the strand cable of $L = 157.3 \text{ mm}$, which is twice the pitch length of the cable, is modeled using 40 continuum mechanics based beam elements where 15 DOFs are used per each beam node as shown in Fig. 33(b). The cross-section of the core and wires are discretized using 16-node cross-sectional elements. In order to capture the plastic responses of the cable, iterative nonlinear analysis was performed.

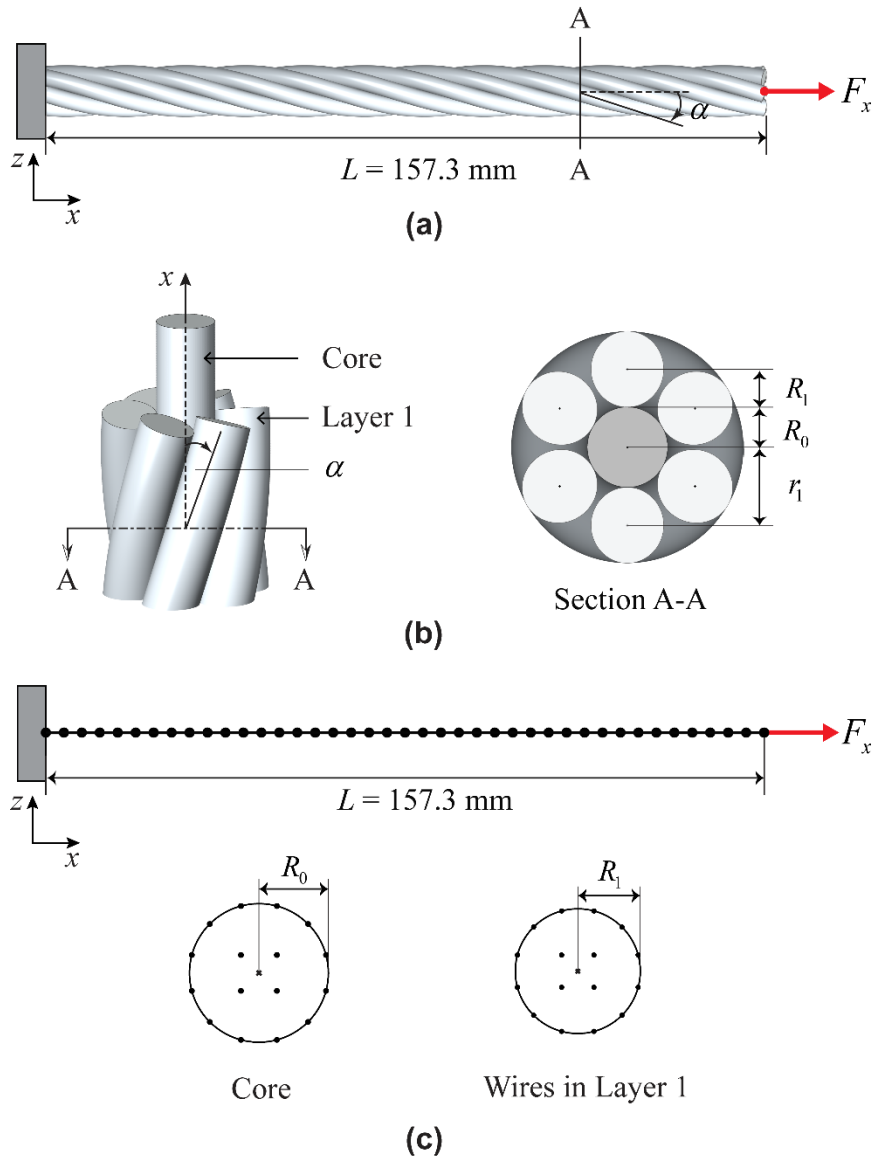


Fig. 33. Cantilever 7-wire strand cable subjected to tip axial loading F_x (a) Problem description, (b) Layer-wise and cross-sectional geometries of the cable, and (c) the present beam model using 40 continuum mechanics based beam elements.

Fig. 34(a) and (b) shows the comparison of the axial loading-axial strain and axial loading-reaction torque curves, as obtained from the present beam model, experimental data, and linear elastic analytical reference solutions. As shown in Fig. 34, both the axial strain and reaction torque obtained from the present beam model exhibit very good agreement with the experimental results in overall ranges. Also, the present beam model well predicts the initiation of yielding.

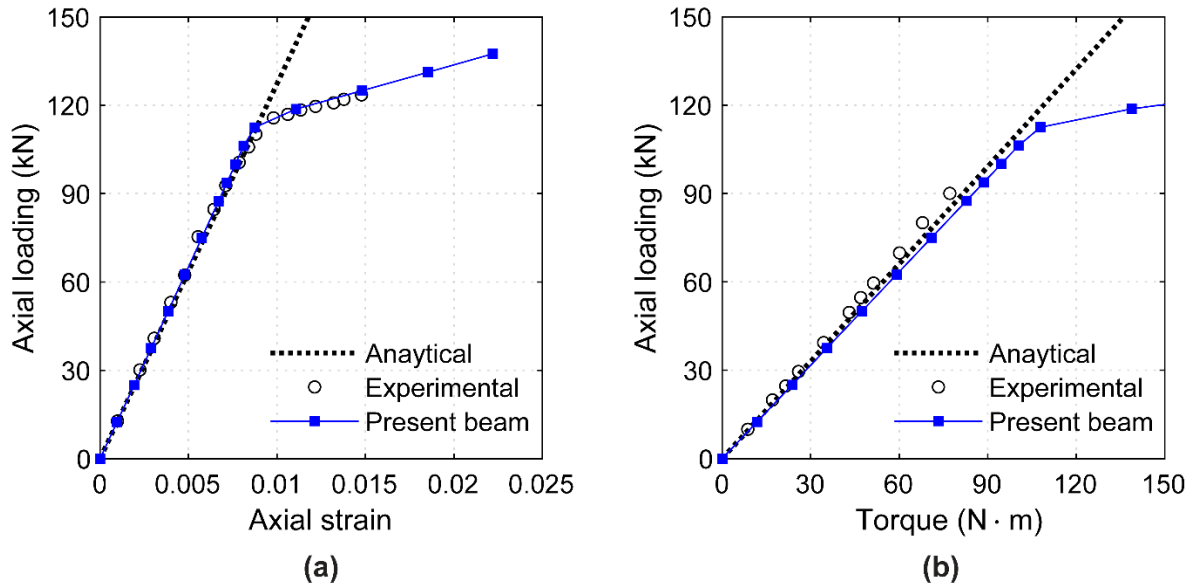


Fig. 34. (a) Axial load-axial strain curves for the axial strain of the cable and (b) Axial load-reaction torque curves for the reaction torque at the tip of the cable.

3.6.5 Two-layer, 19-wire helically stranded cable

A two-layer strand cable of length L that consists of 19 wires is considered as shown in Fig. 35. The cable is clamped at $x = 0$, and is subjected to uniform tensile loading F_x at the tip. The first layer (Layer 1) consist of 6 wires that rotate in a counterclockwise with a lay angle $\alpha_1 = 7.4894^\circ$, and the second layer consists of 12 wires that rotate in a clockwise with lay angles α_2 varying from $\alpha_2 = 0^\circ$ to -30° . According to the lay angles of the Layer 2 α_2 the various geometries of the two-layer strand cables was tested. The radii of the core and outer wires in Layer 1 and Layer 2 are $R_0 = 0.103$, $R_1 = 0.101$, and $R_2 = 0.096$ respectively, and material properties of the core and the wires are linear elastic with Young's modulus $E = 30 \text{ MPa}$ and Poisson's ratio $\nu = 0$.

In the present beam model, the two-layer strand is modeled using continuum mechanics based beam elements using $N_p = 20$ where 30 DOFs are used per each beam node. The cross-section of the core and wires are discretized using 16-node cross-sectional elements

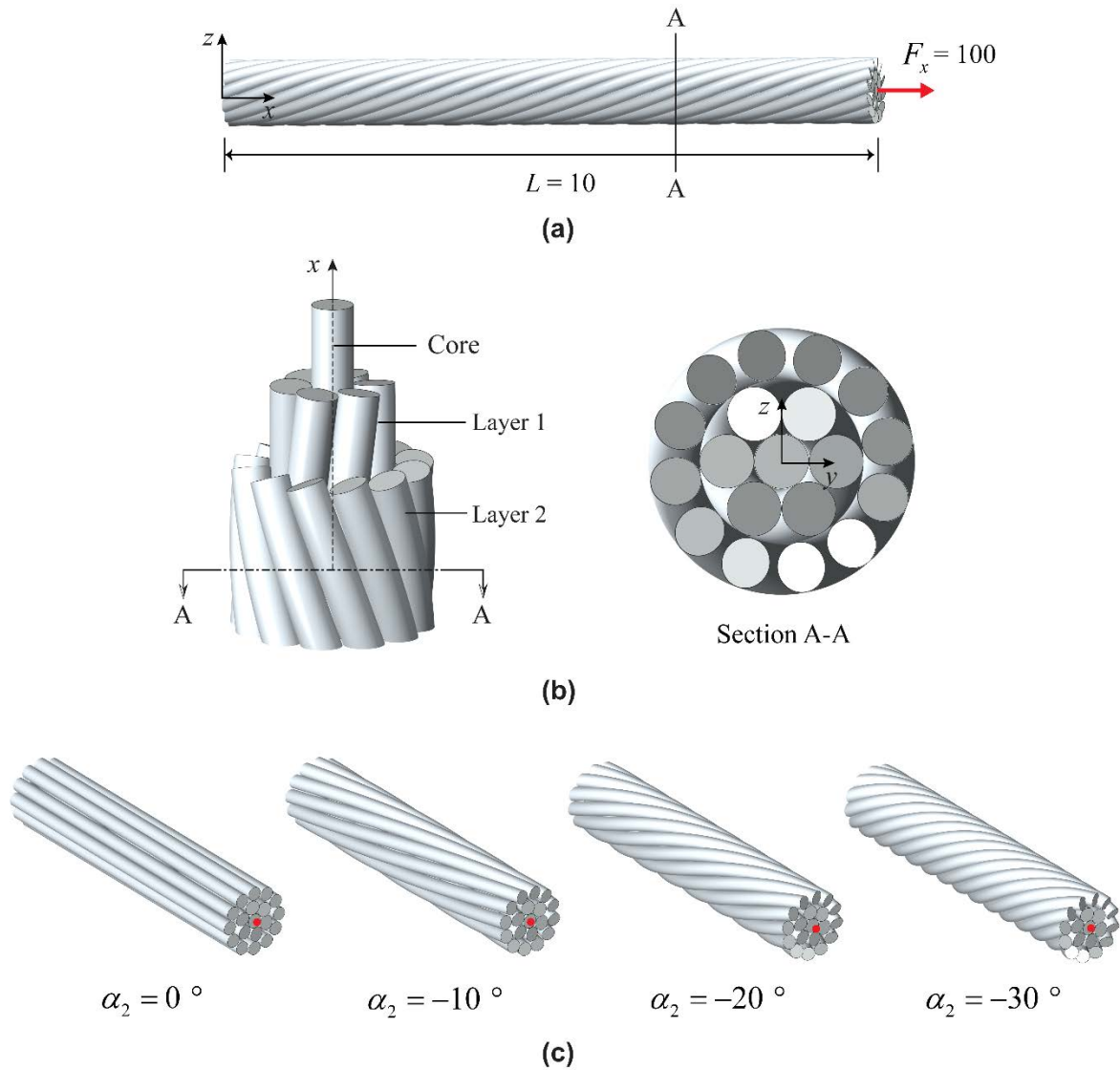


Fig. 35. Two-layer strand cable subjected to tip tensile loading F_x : (a) Problem description, (b) Layer-wise and cross-sectional geometry of the cable, and (c) Various helical geometries of the strand cable when lay angle $\alpha = 0^\circ$, -10° , -20° and -30° .

Fig. 36 compares the axial displacements and torsional angles at the tip of the two-layer strand cables obtained from the present beam model with the analytical references. As shown in Fig. 36, both the axial displacements and torsional angle obtained from the present beam model exhibit very good agreement with the analytical references in overall lay angle ranges.

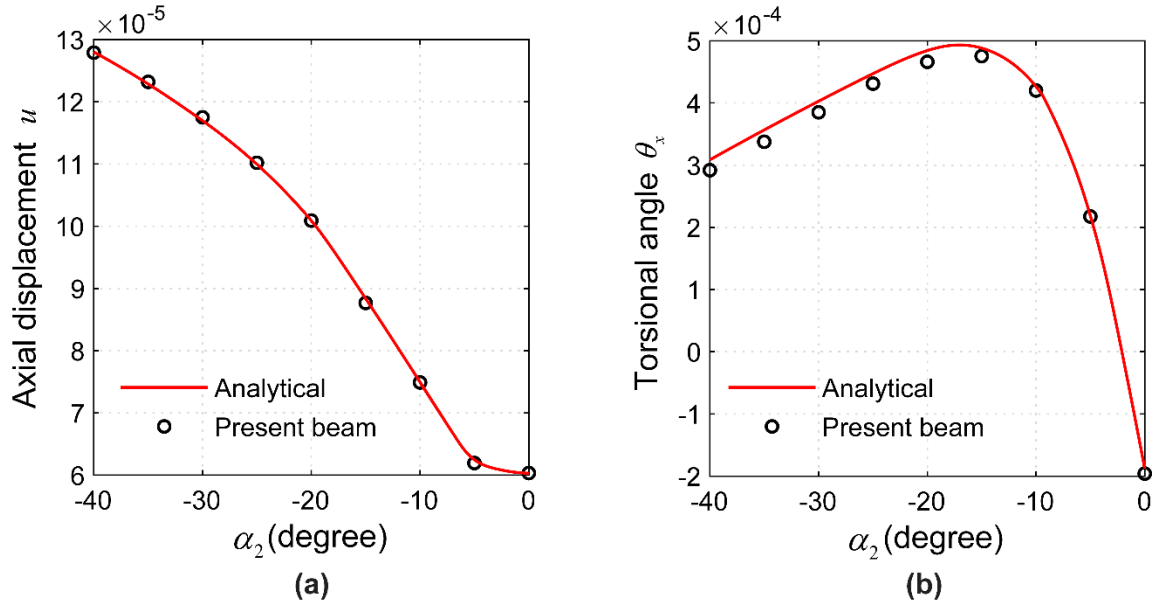
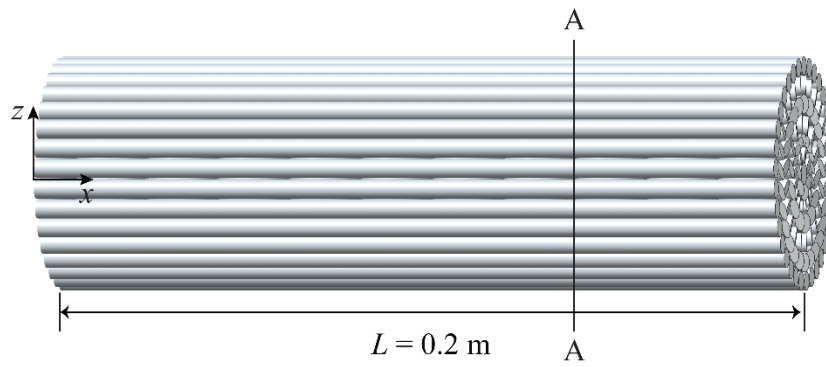


Fig. 36. (a) and (b) Tip displacement and torsional angle under tensile loading F_x obtained from the various geometries of two-layer strand cables (from $\alpha_2 = 0^\circ$ to -40°).

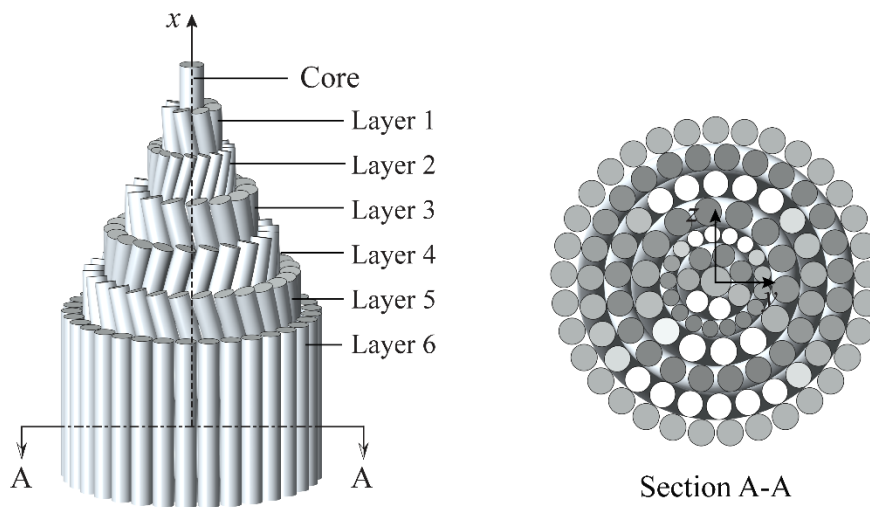
3.6.6 Cantilever six-layer, 120-wire helically stranded cable

The six-layer strand cable of length L that consists of 120 wires is considered as shown in Fig. 37. The cable is clamped at $x = 0$, and is subjected to uniform tensile loading F_x at the tip. The core and wires of the cable has the following material properties: Young's modulus $E = 188 \text{ GPa}$, Poisson's ratio $\nu = 0.3$, the initial yield stress $Y_0 = 1.540 \text{ GPa}$ and the linear hardening modulus $H = 24.6 \text{ GPa}$. The specific geometric information for the wires in the six-layer strand cable are listed in Table 10.

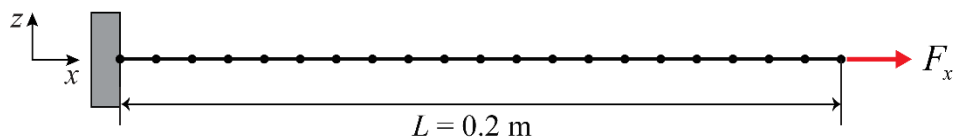
In the present beam model, the cable is modeled using 20 continuum mechanics based beam elements and each cross-section of the core and wires is discretized with 16-node cross-sectional elements. Assuming no inter-wire slip occurs under uniform tensile loading conditions, 23 DOFs are used per each beam node without wire DOFs for representing the inter-wire slip displacement at each wire, and thus 483 DOFs are used in total. The result obtained from the present beam model are compared with the reference solutions obtained from the full 3D solid element models using the commercial software LS-DYNA in [65]. In the LS-DYNA full solid model, 2,520,000 8-node solid elements and 8,393,760 DOFs were used.



(a)



(b)



(c)

Fig. 37. Six-layer cantilever strand cable composed of 120 wires: (a) Problem description, (b) Layer-wise and cross-sectional geometries of the strand cable (b) Present beam model using 20 continuum mechanics based beam elements.

Fig. 38 compares the axial loading- axial strain curves at the tip of the strand cable obtained from the present beam model with the those of obtained from the LS-DYNA full-solid model. In the linear region before yielding occurred inside the cable, the numerical results of present beam model exhibit good agreement with the those of

the LS-DYNA solid model, even though much fewer number of DOFs were used. As the load level increases, however, considerable difference is observed after the initiation of the yielding between two models. These difference is possibly due to a major influence of the wire-to-wire contact deformation and friction conditions in the strand cable.

Table 10. Geometric parameters of cantilever 6-layer, 120-wire helically stranded cable.

Layer	Number of wires	Diameter of wire (mm)	Lay length (mm)	Lay angle (°)
Core	1	5.8	-	0
Layer 1	7	4.3	150	-11.94
Layer 2	17	3.2	210	14.75
Layer 3	14	5.3	320	-14.37
Layer 4	21	5.0	420	15.23
Layer 5	27	5.0	520	-15.66
Layer 6	33	5.0	620	15.95

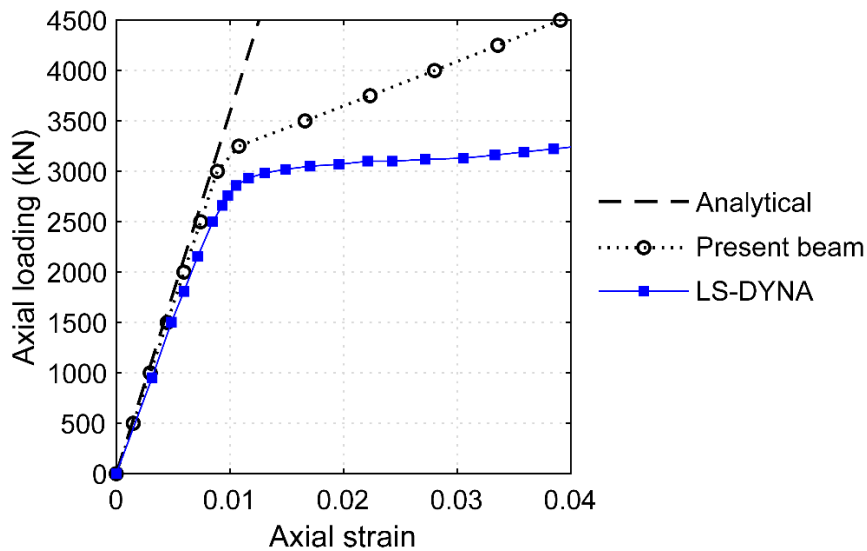


Fig. 38. Axial load-axial strain curves in the cantilever six-layer strand cable that consists of 120 wires subjected to uniform tensile loading F_x at the tip.

3.7. Concluding remarks

3.7.1 Summary

In Chapter 3, a new continuum mechanics based beam element for linear and nonlinear analyses of multi-layered helically stranded cable were presented, and their performance was demonstrated through several representative numerical examples. The novel feature of the proposed beam finite element is an advanced modeling capability that originates from the general 3D geometry and displacement interpolations of the continuum mechanics based beams. Most notably, the proposed beam finite element model enables much simpler and more efficient modeling procedure using relatively small number of the degree of freedom (DOF) because the entire geometry of the helically stranded cable is modeled as a single beam model instead of modeling the individual sub-components. Thus, it is possible to deal with the behavior of the entire layered beam structure regardless of the numbers of layers and sub-components that constitute the cable. It was verified that the proposed beam element model can be utilized very effectively for behavior that does not involve local fracture of some wires that constitute a cable or the failure of cross-sectional geometry, i.e. for cable kinematics that behave while the entire cable structure maintains a helical structure. The following follow-up research, however, is required for the proposed model to be used more comprehensively for more accurate analysis and precise design of cables that exhibit more complex behavior.

3.7.2 Future works

1) **Consideration of contact and friction conditions**

In general, the degree of connection between wires in a cable has a major influence on the bending rigidity and flexible behavior of the cable structure. As the degree of connection between wires increases, the entire cross section of the cable is more integrated and the flexural rigidity of the cable increases. On the contrary, as the degree of connection between wires decreases, the degree of the individual behavior of the wires increases and the flexural rigidity of the cable decreases, thus the cable exhibits more flexible behavioral characteristics. As a matter of facts, the minimum bending radius (MBR) that represents the degree of flexibility of the cable is one of the most important cable design requirements. This is because most cables are very long, and thus cables without sufficient flexibility are difficult to ensure the ease of construction and storage, and are also more vulnerable to failure. Therefore, in the design of common cables, the degree of the inter-wire connection inside the cable is

designed to minimize the MBR value and to reduce the initial contact and touching between the wires. In accordance with the most general cable design conditions, the proposed beam element model was derived by assuming frictionless and no touching conditions between wires.

It is known, however, that touching exists in the initial design of some cables and that the influence of contact and friction inside a cable increases when the cable exhibits extremely large deformation and rotation. In such cases, core-to-wire and wire-to-wire contact and friction conditions have a major influence on the behavior of the entire cable. Therefore, for the accurate analysis of the behavior of more general cables exhibiting large deformation and rotation, further research is required to expand the current model so that the friction and contact conditions inside the cable can be more precisely considered.

2) Expansion to more general cable geometry

The proposed beam finite element deals with only the behavior of cables with strand cable structures. For actual cable structures, however, various geometry is being used in addition to the basic strand cable structures depending on the application and design conditions. Therefore, in order to strengthen the performance and the modeling capability of the present beam model for more comprehensive cable analysis, further research is required to expand the kinematics of the present beam model so that more general types of cable cross-sectional geometry can be dealt with.

3) Consideration of changes in cable cross section

The proposed beam finite element was derived by assuming that the changes in the cross-section of the wires did not occur, thus the cross-sectional area of wires and core are constantly maintained in the entire cable structure. In the behavior of actual cables, however, contraction and expansion in the cross-section of the cables occur depending mainly on the material properties that constitute cables, except some cases in which Poisson's ratio is zero. In particular, for the cables that exhibit large deformation and rotation, the changes in the cross-sectional area has a major influence on the behavior of the cable. In the proposed beam finite element model, the kinematics of the beam allows the specific varying cross-sectional geometry for each beam node. Therefore, it is expected that an improved follow-up model that can closely consider the effect of the cross-sectional contraction and expansion inside the cable can be developed by expanding the kinematics of the current beam model.

Chapter 4. Closing remarks

This thesis introduces new continuum mechanics based beam finite elements for the linear and nonlinear analyses of multi-layered composite beams and helically stranded cable structures. The proposed beam finite elements have many advantages that come from the capability to represent entire 3D geometry and displacement field employing the continuum mechanics based formulations. The largest benefit of the proposed beam finite elements is that it can deal with the multi-layered beam and helically stranded cable structures, which generally have more complex geometries than simple beam structures, as a single beam model regardless of the numbers of layers and sub-components. This enables much simpler and more efficient modeling procedure using relatively small number of the degree of freedom (DOF). Further, the proposed beam finite element is successfully applicable for predicting geometric and material nonlinear behaviors of multi-layered composite beams and helically stranded cable structures. The modeling capability and the performance of the proposed beam element model were verified in several numerical examples. It was confirmed that the proposed beam finite element model can be very efficiently used in the analysis of macroscopic behavior of layered beam and helically stranded cable structures where no extreme failure in the overall structural geometry occurs.

Unlike the conventional beam model, the continuum beam model represents the cross-sectional geometry at each node using the interpolations of cross-sectional nodal positions, which are irrelevant to the degree of freedom (DOF) of the beam, rather than inputting cross-sectional constants at the nodes of one-dimensional elements. Interpolating the cross-sectional geometry at each beam node in the longitudinal direction of the beam, the three-dimensional (3D) position and displacement field of the entire beam is represented. This approach makes it possible to model the specific 3D displacement field of the entire beam without having DOFs at each specific nodal position as in solid element models while the DOFs are defined at the beam nodes of one-dimensional elements as in the conventional beam model.

The great advantages of the continuum mechanics based beam formulation enable more simple modeling procedure and accurate analysis of the complex multi-layered beam and helically stranded cable structures because it specifically models the overall positions of the beam instead of calculating cross-sectional constants that approximate the cross-sectional characteristics of the beam as in the traditional beam model. Further, the kinematics of the continuum beam model can be expanded straightforwardly to cover the more complex behavior

of the beam structures. For example, it is possible to expand the displacement field of the beam by simply adding the warping mode, inter-layer slip, or other distorted modes. In addition to displacements, the cross-sectional tilt direction at a specific position inside the beam can also be defined in detail. Therefore, helical geometries of the cable in which each cross-section of the wire is inclined at different angles and directions can be specifically modeled.

The kinematics of the continuum mechanics based beam model can be expanded in various ways. As a representative case, the continuum beam model expanded with the additional warping mode has been widely used as it is possible to consider the torsional behavior of the beam, which could not be properly described in the conventional 6-DOF beam. In this thesis, the continuum mechanics based beam formulation is expanded to deal with the behaviors of multi-layered beams considering the composite interaction between the layers with corresponding interlayer slips and the helically stranded cables including inter-wire slips and individual wire rotations. If the concept of this continuum mechanics based beam model is further widened, it will be possible to develop more advanced beam finite element models that can be effectively used for the macroscopic structural analysis of various beam shaped structures with more complex geometry, such as multi-layered pipe structures composed of multiple concentric layers, double-helix structures, and umbilical cables.

Bibliography

- [1] Reddy JN. Mechanics of laminated composite plates: theory and analysis. New York: CRC Press; 1997.
- [2] Jones RM. Mechanics of composite materials. McGrawHill; 1975.
- [3] Hodges DH. Nonlinear composite beam theory. New York: AIAA; 2006.
- [4] Newmark NM, Siess CP, Viest IM. Tests and analysis of composite beam with incomplete interaction. Proc Soc Exp Stress Anal 1951;9:75–92.
- [5] Adekola AO. Partial interaction between elastically connected elements of a composite beam. Int J Solids Struct 1968;4(11):1125–35
- [6] Kamiya BF. Buckling theory of sheathed walls; Linear Analysis 1987;113:2009–22.
- [7] Girhammar UA, Gopu VKA. Composite beam-column with interlayer slip-exact analysis. J Struct Eng 1993;119:1265–1282.
- [8] Dan L, Wheat JMC. Nonlinear analysis of two-layered wood members with inter- layer slips. J Struct Eng 1994;120:1909–29
- [9] Chui Y, Barclay D. Analysis of three-layer beams with non-identical layers and semi-rigid connections. Can J Civ Eng 1998:271–6.
- [10] Zieliński AP, Frey F. Nonlinear weighted residual approach: application to laminated beams. Comput Struct 2003;81:1087–98.
- [11] Foraboschi P. Analytical Solution of Two-Layer Beam Taking into account Interlayer Slip and Shear Deformation. J Struct Eng 2007;133:886–94.
- [12] Monetto I. Analytical solutions of three-layer beams with interlayer slip and step-wise linear interface law. Compos Struct 2015;120:543–51.
- [13] Krawczyk P, Frey F, Zielinski AP. Large deflections of laminated beams with interlayer slips Part 1 : model development. Eng Comput 2007;24:17–32.

- [14] Krawczyk P, Frey F, Zielinski AP. Large deflections of laminated beams with interlayer slips Part 2 :finite element development. *Eng Comput* 2007;24:17–32.
- [15] Čas B, Saje M, Planinc I. Non-linear finite element analysis of composite planar frames with an interlayer slip. *Comput Struct* 2004;82:1901–12.
- [16] Battini JM, Nguyen QH, Hjiat M. Non-linear finite element analysis of composite beams with interlayer slips. *Comput Struct* 2009;87:904–12.
- [17] Dall'Asta A, Zona A. Non-linear analysis of composite beams by a displacement approach. *Comput Struct* 2002;80:2217–28.
- [18] Gara F, Ranzi G, Leoni G. Displacement based formulations for composite beams with longitudinal slip and vertical uplift. *Int J Numer Methods Eng* 2006;65(8):1197–220
- [19] Nguyen QH, Hjiat M, Lai VA. Force-based FE for large displacement inelastic analysis of two-layer Timoshenko beams with interlayer slips. *Finite Elem Anal Des* 2014;85:1–10.
- [20] Hozjan T, Saje M, Srpčič S, Planinc I. Geometrically and materially non-linear analysis of planar composite structures with an interlayer slip. *Comput Struct* 2013;114–115:1–17.
- [21] Ayoub A, Filippou FC. Mixed formulation of nonlinear steel–concrete composite beam element. *ASCE J Struct Eng* 2000;126(3):371–81
- [22] Faella C, Martinelli E, Nigro E. Steel and concrete composite beams with flexible shear connection: “exact” analytical expression of the stiffness matrix and applications. *Comput Struct* 2002;80:1001–9.
- [23] Sousa Jr JBM, da Silva AR. Analytical and numerical analysis of multilayered beams with interlayer slip. *Eng Struct* 2010;32:1671–80.
- [24] Sousa Jr JBM. Exact finite elements for multilayered composite beam-columns with partial interaction. *Comput Struct* 2013;123:48–57.
- [25] Ranzi G. Locking problems in the partial interaction analysis of multi-layered composite beams. *Eng Struct* 2008;30:2900–11.
- [26] Bathe KJ. *Finite element procedures*. New Jersey: Prentice Hall; 2006.
- [27] Yoon K, Lee YG, Lee PS. A continuum mechanics based beam finite element with warping displacements and its modeling capabilities. *Strut Eng Mech* 2012;43:411–37

- [28] Yoon K, Lee PS. Nonlinear performance of continuum mechanics based beam elements focusing on large twisting behaviors. *Comput Methods Appl Mech Eng* 2014;281:106–30.
- [29] Yoon K, Lee PS, Kim DN. Geometrically nonlinear finite element analysis of functionally graded 3D beams considering warping effects. *Compos Struct* 2015;132:1231–47.
- [30] Yoon K, Lee PS, Kim DN. An efficient warping model for elastoplastic torsional analysis of composite beams. *Compos Struct* 2017;178:37–49
- [31] Yoon K, Kim DN, Lee PS. Nonlinear torsional analysis of 3D composite beams using the extended St . Venant solution. *Struct Eng Mech* 2017;1:33–42.
- [32] Neto EAS, Peric D, Owen DRJ. *Computational method for plasticity: theory and applications*. Wiley & Sons; 2008.
- [33] ADINA R&D, *ADINA theory and modeling guide*, Watertown, MA: ADINA R&D; 2013.
- [34] Foschi RO, Bonac T. Load-slip characteristics for connections with common nails. *Wood Sci.* 1977;9(3):118–23.
- [35] Alfano G, Crisfield MA. Finite element interface models for the delamination ana- lysis of laminated composites: mechanical and computational issues(2). *Int J Numer Methods Eng* 2001;50:1701–36.
- [36] Camanho PP, Dávila, C. Mixed-mode decohesion finite elements for the simulation of delamination in composite materials. *NASA/TM-2002-211737*; 2002. pp. 1–37.
- [37] Turon A, Camanho PP, Costa J, Dávila CG. A damage model for the simulation of delamination in advanced composites under variable-mode loading. *Mech Mater* 2006;38:1072–89.
- [38] Reeder JR, Crews JH. Mixed-mode bending method for delamination testing. *AIAA J* 1990;28:1270–6.
- [39] Utting WS, Jones N. Tensile testing of a wire rope strand. *J Strain Anal* 1985;20(3):151–64.
- [40] Utting WS, Jones N. The response of wire rope strands to axial tensile loads – Part I: experimental results and theoretical predictions, *Int. J. Mech. Sci.* 29 (9) (1987) 605–619.
- [41] Utting WS, Jones N. The response of wire rope strands to axial tensile loads – Part II: comparison of experimental and theoretical predictions, *Int. J. Mech. Sci.* 29 (9) (1987) 621–636.

- [42] Utting WS, Jones N. Axial-torsional interactions and wire deformation in 19- wire spiral strand, *J. Strain Anal. Eng. Des.* 23 (2) (1988) 79–86.
- [43] Hruska FH. Calculation of stresses in wire ropes. *Wire and wire products* 1951;26(9):766–7.
- [44] Hruska FH. Radial forces in wire ropes. *Wire and wire products* 1952;27(5):459–63.
- [45] Hruska FH. Tangential forces in wire ropes. *Wire and wire products* 1953;28(5):455–60.
- [46] McConnell KG, Zemeke WP. A model to predict the coupled axial torsion properties of ACSR electrical conductors. *Journal of Experimental Mechanics* 1982;22:237–44.
- [47] Machida S, Durelli AJ. Response of a strand to axial and torsional displacements. *Journal of Mechanical Engineering science* 1973;15:241–51.
- [48] Knapp RH. Derivation of a new stiffness matrix for helically armoured cables considering tension and torsion. *International Journal for Numerical Methods in Engineering* 1979;14:515–20.
- [49] Costello GA, Philips JW. Effective Modulus of twisted wire cables. *ASCE, Journal of the Engineering Mechanics Division* 1976;102:171–81.
- [50] Philips JW, Costello GA. Analysis of wire rope with internal-wire rope cores. *ASME Journal of Applied Mechanics* 1985;52:510–6.
- [51] Velinsky SA. General nonlinear theory for complex wire rope. *International Journal of Mechanical Sciences* 1985;27:497–507.
- [52] Kumar K, Cochran Jr JE. Closed-form analysis for elastic deformations of multilayered strand. *ASME Journal of Applied Mechanics* 1987;54:898–903.
- [53] Raoof M, Hobbs RE. Analysis of multilayered structural strands. *Journal of Engineering Mechanics* 1988;114(7):1166–82.
- [54] Raoof M, Kraincanic I. Simple derivation of the stiffness matrix for axial/torsional coupling of spiral strands. *Computers and Structures* 1995;55(4):589–600.
- [55] Costello GA. *Theory of wire rope*. 2nd ed. New York: Springer; 1997.
- [56] Sathikh S, Moorthy MBK, Krishnan M. A symmetric linear elastic model for helical wire strands under axisymmetric loads. *Journal of Strain Analysis* 1996;31(5):389–99.

- [57] Kumar K, Botsis J. Contact stresses in multilayered strands under tension and torsion. *Journal of Applied Mechanics* 2001;68:432–40.
- [58] Elata D, Eshkenazy R, Weiss MP. The mechanical behavior of a wire rope with an independent wire rope core. *International Journal of Solids and Structures* 2004;41(5):1157–72.
- [59] Ghoreishi SR, Messenger T, Cartraud P, Davies P. Validity and limitations of linear analytical models for steel wire strands under axial loading, using a 3D FE model. *Int J Mech Sci* 2007;49:1251–61.
- [60] [8] Chiang YJ. Characterizing simple-stranded wire cables under axial loading. *Finite Elem Anal Des* 1996;24(2):49–66.
- [61] [49] Jiang WG, Yao MS, Walton JM. A concise finite element model for simple straight wire rope strand. *International Journal of Mechanical Sciences* 1999;41(2):143–61.
- [62] [48] Nawrocki A, Labrosse M. A finite element model for simple straight wire rope strands. *Computers and Structures* 2000;77:345–59.
- [63] [50] Jiang WG, Henshall JL, Walton JM. A concise finite element model for three-layered straight wire rope strand. *International Journal of Mechanical Sciences* 2000;42(1):63–89.
- [64] Wehking K-H, Zieglen S. Calculation of a standard rope with FEM. *Wire* 2004;54(2):96–100.
- [65] Judge R, Yang Z, Jones SW, Beattie G. Full 3D finite element modeling of spiral strand cables, *Constr. Build. Mater.* 35 (2012) 452–459.
- [66] Stanova E, Fedorko G, Fabian M, Kmet S. Computer modelling of wire strands and ropes part II: finite element-based applications, *Adv. Eng. Softw.* 42 (6) (2011) 322–331.
- [67] Kmet S, Stanova E, Fedorko G, Fabian M, Brodniansky J., Experimental investigation and finite element analysis of a four-layered spiral strand bent over a curved support, *Eng. Struct.* 57 (2013) 475–483.
- [68] Yu Y, Chen Z, Liu H, Wang X. Finite element study of behavior and interface force conditions of seven-wire strand under axial and lateral loading. *Constr Build Mater* 2014;66:10–8.
- [69] Kim SY, Lee PS. Modeling of helically stranded cables using multiple beam finite elements and its application to torque balance design. *Constr Build Mater* 2017;151:591–606.
- [70] Filotto FM, Kress G. Nonlinear planar model for helical structures. *Comput Struct* 2019;224:106111.
- [71] Kim HJ, Yoon K, Lee PS. Continuum mechanics based beam elements for linear and nonlinear analyses of multi-layered composite beams with interlayer slips. *Compos Struct* 2020;235:111740.
- [72] Craig, J.J. *Introduction to Robotics: Mechanics and Control*, 2nd ed. Pearson Prentice Hall; 2005

[73] MW Spong, S Hutchinson, M Vidyasagar. Robot Dynamics and Control, 2nd ed. John Wiley & Sons; 2004

[74] P. McKerrow, H. Zima. Introduction to Robotics, 2nd ed. Addison-Wesley; 1991

